Ultrafast acoustics in hybrid and magnetic structures

Viktor Shalagatskyi

l'université nantes angers le mans
COMMUNAUTÉ D'UNIVERSITÉS ET ÉTABLISSEMENTS

Université du Maine
Le Mans - Laval

Thèse de Doctorat

Viktor SHALAGATSKYI

Mémoire présenté en vue de l'obtention du
grade de Docteur de l'Université du Maine
sous le label de L'Université Nantes Angers Le Mans

École doctorale : *3MPL*

Discipline : *Milieux denses et matériaux*
Spécialité : *Physique*
Unité de recherche : *IMMM*

Soutenue le *30.10.2015*

Ultrafast Acoustics in Hybrid and Magnetic Structures

JURY

Rapporteurs :	**Andreas HUETTEN**, Professeur, Bielefeld University **Ra'anan TOBEY**, Professeur associé, University of Groningen
Examinateurs :	**Florent CALVAYRAC,** Professeur, Université du Maine **Alexey MELNIKOV**, Professeur associé, Fritz-Haber-Institut der MPG
Directeur de Thèse :	**Vasily TEMNOV**, Chargé de recherches, CNRS, HDR, Université du Maine
Co-directeur de Thèse :	**Thomas PEZERIL**, Chargé de recherches, CNRS, HDR, Université du Maine
Co-Encadrante de Thèse :	**Gwenaëlle VAUDEL**, Ingénieur de recherche, CNRS, Université du Maine

Contents

List of figures

List of tables

I dedicate this thesis to my family.

Acknowledgments

I am very much obliged to region Pays de la Loire for funding of this work under the grant "Nouvelle équipe nouvelle thematique" and to many people who helped me during last four years.

First of all I am sincerely grateful to my supervisor Vasily Temnov, who offered me to become a part of his team and furnished a chance to work with many interesting projects. I appreciate all hard work he has done to enhance the outcome of this work.

I am especially grateful to my co-supervisor Thomas Pezeril, thanks to his skills and experience in experimental physics I was able to conduct all the measurements for this work.

I owe my most sincere gratitude to my co-supervisor Gwennaëlle Vaudel who supported me not only in scientific field, but also by motivating discussions that helped me to bear frustrations.

My PhD would not be officially possible without invaluable help from the president of our university Rachid el Guerjouma, head of our department Jean-Marc Greneche, Florant Calvayrac and Anne Desert. All these people putted a lot of efforts in helping me to obtain the residence permit. I also want to thank Pascal Ruello and Jean-Marc Breteau who helped me during my Master study.

Assistance provided by Vitaly Gusev for helping me with Two Temperature Model is greatly appreciated. I want to thank also Alexey Lomonosov and Alexandr Kovalenko for encouraging scientific discussions and enjoyable company. I address many thanks to my group members Tymur Parpiiev and Ievgenia Chaban for having fun after work and their support in day-to-day life. Additionally, I wish to acknowledge the support provided by Osamu Matsuda and Denis Mounier during the experimentation period. My special gratitude goes to Denis Makarov and his team for providing the excellent quality samples for the measurements.

My special thanks are extended to my chemistry teacher Marina Buyakevich who inspirit in me love to natural sciences from the very first years in the school. Teacher like you are hard to find and I am grateful for everything you have taught me.

I appreciate my parents encouragement and advice. Without fulled by their love and support phone calls it would be very hard to continue working hard. Also I want to thank my grandfather who helped me a lot during my graduate study.

Finally, I would like to thank my beloved wife Inna. Words cannot describe how grateful I am for your enduring support and unconditional love. Your unwavering faith in me brings energy to beat challenges and move forward.

0 Introduction

This thesis aims to understand the ultrafast dynamics of electronic, thermal and acoustic excitations in noble metal - ferromagnet multilayer structures starting from the initial stage of ultrafast laser absorption up to the detection of the generated picosecond acoustic pulses by using femtosecond pump-probe techniques and numerical simulations. Various interesting transient physical processes take place on intermediate time scales. Understanding and explaining the mechanisms of each of them lead us to possibility of controlling electronic, mechanical and magnetic properties of the materials.

There are many works which describe the mechanisms of interaction of an ultrashort laser pulse with a metallic film followed by the generation of acoustic pulses of different frequencies[1,2,3,4,5,6].

The main novelty of this work is that we analyze the acoustic pulses (or strain) generated in a cobalt layer by diffusive electrons which were laser excited in an adjacent gold overlayer. It was possible to observe this phenomenon because of two main factors:

1. The ultrashort laser pulse excites diffusive electrons in a noble metal with large electron mean free path $l_{electron}$ like gold, silver or copper[7,8,9,5]. For example, in gold the electron mean free path is $l^{Au}_{electron} = 40$ nm.
2. The second condition requires that the metallic layer adjacent to the noble metal layer (with efficient electron diffusion) has a large value of electron-phonon coupling g. Among metals with large values of g we can highlight ferromagnetic cobalt and nickel metals. As an example, the electron-phonon coupling in cobalt is about 20 times larger than in gold[10,11].

The electron mean free path in cobalt is very short ($l^{Co}_{electron} = 1$ nm[12]), this indicates about the inefficient electron diffusion and the efficient generation of much short acoustic pulses of greater amplitude than in the gold.

In this thesis we focused only on hybrid gold/cobalt samples : a cobalt layer sandwiched

between a variable gold layer and a sapphire substrate. By increasing the gold layer thickness we alter the amount of electrons that reach the adjacent cobalt layer and as a result the amplitude of the cobalt strain decreases. Surprisingly, it was found that the generation of the acoustic pulses in cobalt layer was efficient through 500 nm thick gold layer. Alternatively, we observed also the generation of acoustic pulses by diffusive electrons in case of gold/platinum/sapphire sample.

To analyze the electron diffusion and lattice heating we used the Two-Temperature Model (TTM)[13,14,15]. This model was modified to take into account the electron diffusion in the gold/cobalt structure. First numerical simulations showed that the amplitude of the lattice temperature generated by diffusive electrons is few times greater than observed experimentally (we compared the lattice temperature with the profile of the acoustic pulse). We assume, that the most logical explanation of the difference between simulation and experiment is related to the Kapitza resistance (thermal boundary resistance). In the case of an interface between two metals, the major influence on the value of the Kapitza resistance is related to electrons[16]. For this reason we included the electron Kapitza resistance into the TTM to decrease the electron flux through the gold/cobalt interface which results in a decrease of the cobalt lattice temperature.

The information about the profile of the established lattice temperature after electron-phonon equilibration is used as an input to describe the heat diffusion inside the sample using the heat diffusion model. We studied the heat diffusion using the finite-element software COMSOL to determine the Kapitza resistances of the structure. First of all we analyzed the cooling rate of the single gold and cobalt films deposited on a sapphire substrate. Then we implemented a more sophisticated simulation of hybrid gold/cobalt/sapphire structure.

Our analysis demonstrates that introduction of a thin cobalt layer sandwiched between a gold layer and a sapphire substrate allows to increase the cooling rate of the overheated metallic layers.

Throughout this work we used the pump-probe technique to measure the transient reflectivity ΔR at nanosecond and picosecond timescales. Measured data allowed us to study the thermal transport and to extract the values of the Kapitza resistances for multiple interfaces. Additionally, using the picosecond data we were able to study the acoustic profiles of the generated strains.

This dissertation is organized in four chapters. In the first chapter we start from the classical model of interaction of a femtosecond laser pulse with a metallic film followed by the non-equilibrium electron dynamics. We present the modified TTM suited for the studies of electron diffusion in bimetallic structures. Then we review the analytical approaches describing the Kapitza resistance for phonons and electrons. In the final part we present the necessary modifications to the TTM which take into account the electron Kapitza resistance.

Chapter 2 is devoted to theoretical and experimental features of the optical pump-probe technique. We present the thermo-elastic model for acoustic pulses generation and apply the

finite-difference algorithm to solve the acoustic wave equation. We review the mechanisms for the reflectivity changes induced by acoustic pulses. The developed algorithm for the acoustic pulse reconstruction using Fourier transform is explained. This algorithm was applied to the transient reflectivity and acousto-plasmonic datas. We also explain the pump-probe setups and some technical details.

In chapter 3, we present a step-by-step analysis of the transient reflectivity data. First of all we present the analysis of the heat diffusion for gold/sapphire, cobalt/sapphire and gold/cobalt/sapphire samples. By fitting the thermal background of the reflectivity we extract the values of the Kapitza resistances of all interfaces. Then we quantitatively analyze the profiles of electron and lattice temperatures obtained by the TTM simulations for an ideal metallic interface and for an interface which includes the Kapitza resistance. From these simulations we extract also the lattice temperature of the cobalt layer that governs the amplitude of the generated strain. The last section covers the analysis of the acoustic component of the transient reflectivity curve. This acoustic component was obtained by subtraction of the simulated thermal background provided by COMSOL from the experimental data. The temperature distribution used in COMSOL is applied to simulate the acoustic component of the reflectivity. We also performed the TTM simulations with the Kapitza resistance to fit the acoustic component of the reflectivity.

In chapter 4 we present general conclusions and discussions.

1

Ultrafast carrier transport at the nanoscale

This chapter starts from a brief recall of the ultrafast processes that follows an excitation of a metallic nanofilm by an ultrashort laser pulse. After that the Two Temperature Model (TTM) developed to describe electron diffusion inside a bimetallic structure will be presented. Finally, the TTM that takes into account the Kapitza resistance of the interface between two metals will be described.

Let us consider a situation when femtosecond laser pulse is normally incident on a free surface of the metallic nanofilm that is shown in Fig. 1.1. On the first stage, the laser light with a central wavelength λ will penetrate inside the metal film within a finite skin depth δ_{skin}. Each material has its own skin depth for a given wavelength of the electro-magnetic wave, but for metals within the visible light spectra it is typically few tens of nanometers.

Formally, the skin depth is determined by the imaginary part k of the complex refractive index $\widetilde{n} = n + ik$ as follows

$$\delta_{skin} = \frac{\lambda}{4\pi k}. \tag{1.1}$$

The energy deposition inside the metallic film (shown by white solid line in Fig. 1.2) has an exponential profiles that is governed by the skin depth parameter and is given by Lambert-Beer's law

$$I(z) = I_0 e^{-z/\delta_{skin}}, \tag{1.2}$$

where I_0 is the intensity of the incident laser light and z is the sample thickness.

Photons that are penetrating within the skin layer excite free electrons from the valence band to the state above the Fermi level E_F. If the photon has small energy $h\nu$ the electron will experience an intraband transition, but if the photon energy is high enough to overcome the band gap the transition will be interband. For example, if we consider illumination of

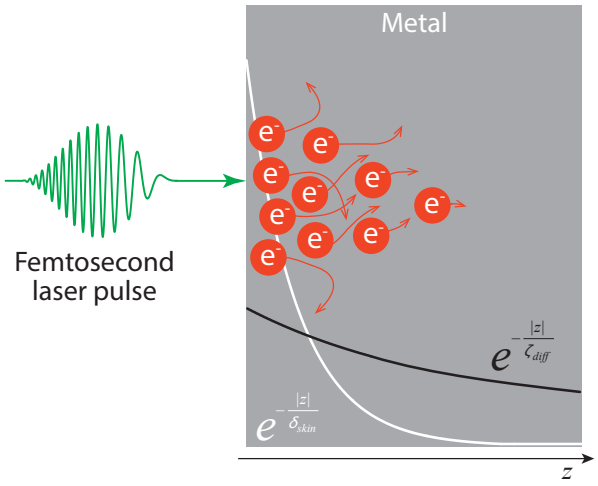

Figure 1.1: Sketch of an interaction of femtosecond laser pulse with a metal resulting in the electron diffusion. Exponential profile of the laser light penetration is shown by white solid line and black solid line shows the profile of the heat diffusion.

gold by 800 nm laser pulse the electron transition will be intraband because energy of the photon is smaller than the energy for the d band to the Fermi-surface transition (1.5 eV $\leq$ 2.4 eV)[17,18]. However, energy of 400 nm laser pulse is sufficient for interband transition in gold.

Amount of electrons excited by the photon absorption is proportional to the photon energy and the density of the laser pulse as it is shown in Fig. 1.2 a), where red box is the total amount of electrons promoted to the states above the Fermi level. At this moment the distribution of the electrons can not be characterized by the Fermi-Dirac statistics that is why the distribution is called non-Fermi like. As a result, this highly non-equilibrium state can not be characterized by the value of the electron temperature.

However, just after laser excitation electrons redistribute the excess energy through electron-electron scattering with a characteristic time τ_{e-e} that is typically of the order of few hundreds of femtoseconds[19] (the scattering is described within the framework of the Landau theory of Fermi-liquid[20]). As a result of electron-electron scattering electrons thermalize by the time of thermalization τ_{therm} (in a low excitation regime electrons in gold thermalize within 1 ps[21]). After thermalization the distribution of electrons can be described by the Fermi-Dirac statistics that is shown in Fig. 1.2 b). Just after thermalization the temperature of the electrons is typically high and can even reach $10^4 \div 10^5$ K for a pulsed laser in the range of petawatts (10^{15})[22,23]. From the other hand the temperature of lattice remains unchanged that is why electrons after thermalization can be referred as "hot".

The next step is a fast diffusion of these "hot" electrons propagating with the Fermi velocity. In the case of the noble metals like gold and copper electrons can diffuse on the distances much bigger than δ_{skin}[24,25,5] and even overcome hundreds of nanometers. During the diffusion, the electrons scatter with phonons that give a slow (as compared to the electron temperature dynamics) rise to the lattice temperature. The characteristic time of

electron-phonon interaction τ_{e-p} can be estimated theoretically to be on the same order of magnitude as τ_{e-e}, thus for gold with for $T_e \gg 300$ K it should be $\tau_{e-e} = 60$ fs[26]. However, experimentally electron-phonon interaction time in gold was estimated to be 700 fs[27].

Electrons exchange their energy with the phonons until the total equilibration is reached, i.e, the moment when both electron and lattice temperatures are equal $T_e = T_i$, that is shown in Fig. 1.2 c). For metals, electrons and phonons rapidly come to equilibrium by the time below $\tau_{eq} = 10$ ps. For example, thermal equilibrium in gold, under a laser fluence of 1 mJ.cm^{-2}, is achieved in $\tau_{eq} = 4$-5 ps[28].

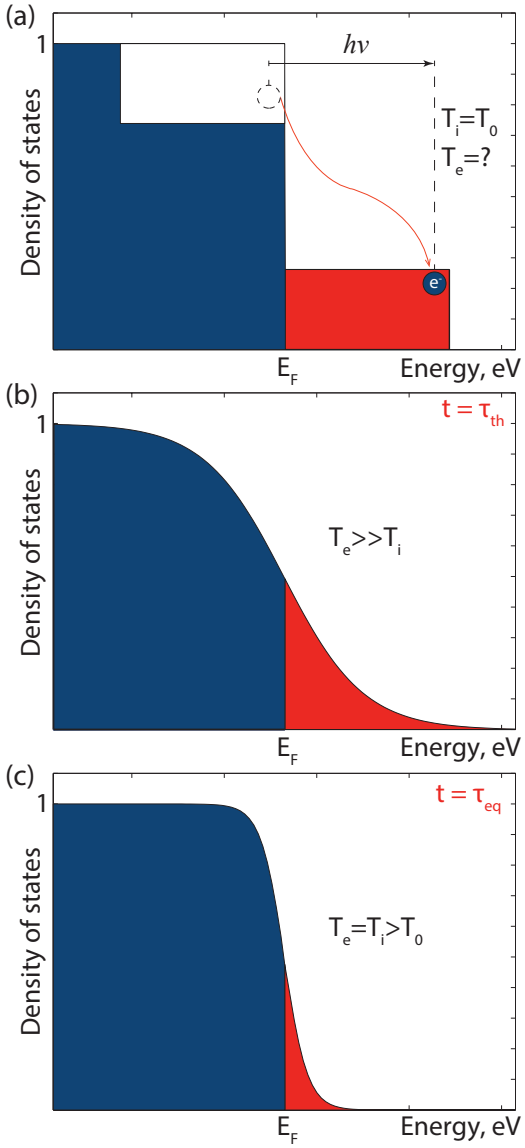

Figure 1.2: Consequent dynamics of the distribution of electrons induced by a femtosecond laser pulse; a) quasi-instantaneous repopulation of the states above the Fermi level E_F induced by absorption of the laser pulse with energy $h\nu$. Formed distribution is non-Fermi like because of the high level of non-equilibrium, as a result system can not be characterized by an electron temperature T_e. b) After electron thermalization (by the time $t = \tau_{th}$) the electron distribution can be described by the Fermi-Dirac statistics, thus electrons can be characterized by some value of T_e that is typically greater than the lattice temperature T_i. c) Through electron-phonon interaction the energy of electrons is redistributed to the lattice and the system reaches equilibrium ($T_e = T_i$) by the time τ_{eq}.

Finally, by the time τ_{eq} the heat diffusion profile is formed (that is referred to the spatial distribution of the lattice temperature) which is characterized by diffusion length ζ_{diff} shown by black solid line in Fig. 1.2. The main mechanism of the energy transfer in system now is the thermal diffusion driven by the gradient of the lattice temperature.

When laser pulse duration is much bigger than the time necessary for electronic and phononic subsystems to reach the equilibrium $\tau_{laser} \gg \tau_{eq}$ the dynamics of the temperature can be reliably well described by only one temperature model, where there is no distinction between electronic and phononic temperatures and carrier concentration can be determined by Fermi-Dirac distribution. But if laser pulse duration is less or comparable with the time of temperature equilibration $\tau_{laser} \leq \tau_{eq}$ one temperature model is no longer adequate for describing of the thermal properties of the system, that is why the TTM is widely used to explain carrier dynamics in femtosecond optical studies[14,13,28,29].

1.1 Two Temperature Model for bimetallic structure

The core idea of the TTM is based on the interaction of the laser light with a free electron gas with consequent heating of lattice through electron-phonon interaction at the short timescale. Despite the fact that the free electron gas in this model should thermalize instantaneously, it can be successfully used to describe the ultrafast energy transport at the microscale and explain some experimental observations that will be discussed in the data analysis chapter.

First phenomenological version of the TTM was proposed by Kaganov et al.[14] and Anisimov et al.[13] for quantitative predictions of highly non-equilibrium changes in metals induced by ultra-short laser pulses. This model suppose that energy injected by the laser pulse is redistributed among two carriers: electrons and phonons which are characterized by two temperatures T_e and T_i respectively.

Neglecting the duration of electron thermalization[30] the temporal and spatial evolution in 1D of both electronic and phononic temperatures can be found by solving two coupled nonlinear differential equations

$$\begin{aligned} C_e(T_e)^{(1,2)}\frac{\partial T_e^{(1,2)}}{\partial t} &= k_{1,2}(T_e)\frac{\delta^2 T_e^{(1,2)}}{\partial z^2} - g_{1,2}(T_e^{(1,2)} - T_i^{(1,2)}) \\ C_i^{(1,2)}\frac{\partial T_i^{(1,2)}}{\partial t} &= g_{1,2}(T_e^{(1,2)} - T_i^{(1,2)}), \end{aligned} \tag{1.3}$$

where $C_e(T_e)$ is the electronic heat capacity (assumed to depend linearly from T_e in low range of excitations[16]), $k(T_e)$ is the electronic thermal conductivity (that also depends linearly on T_e[28,31]), g is the electron-phonon coupling constant that does not vary significantly in the low excitation regime[24,32,15], C_i is the lattice heat capacity. We neglect the diffusion of phonons because equilibration of the system takes less than few picoseconds. The superscripts (1) and (2) denote the metallic layers.

We will solve the TTM for the structure shown in Fig. 1.3 where there are two layers

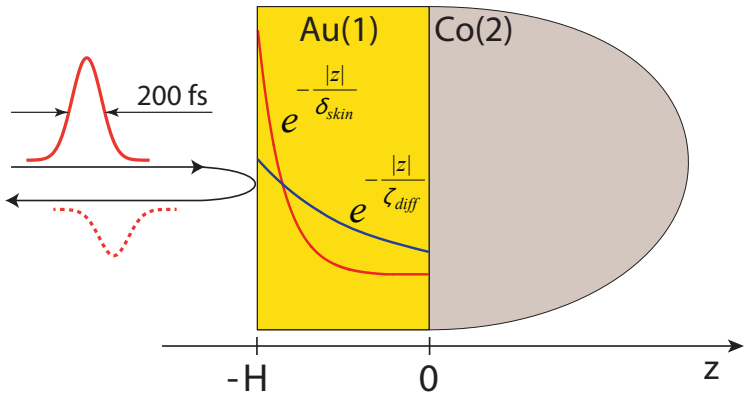

Figure 1.3: Model of bimetallic structure composed of a gold film and a semi-infinite cobalt substrate that is excited by 200 fs laser pulse. Two profiles of energy deposition are depicted in the gold layer, first shows the exponential skin depth characterized by δ_{skin}. And the second displays the heat diffusion profile with a diffusion length ζ_{diff}.

composed of gold and cobalt. In this model the gold layer of thickness H is illuminated by a normally incident 200 fs FWHM ultrashort laser pulse. However adjacent cobalt layer is considered to be semi-infinite. The energy of laser pulse is partially transferred to free electrons in gold within the skin layer δ_{skin} and the remaining part is reflected according to the reflection coefficient R. Excited free electrons diffuse with velocities close to the Fermi velocity v_F and penetrating on hundreds of nanometers in case of noble metals[33,24,5]. Electron diffusion length is characterized by ζ_{diff} and determined by thermal conductivity k and electron-phonon coupling coefficient g giving $\zeta_{diff} = \sqrt{k/g}$ (derivation of this formula under few assumptions will be shown later). In noble metals, the electron diffusion is very efficient and results in much deeper penetrations as compared to skin depth $\zeta_{diff} \gg \delta_{skin}$[33].

Following initial and boundary conditions are applied

$$k_1 \frac{\partial T_e^{(1)}}{\partial z}\bigg|_{z=-H} = -(1-R)If(t) \tag{1.4}$$

$$k_1 \frac{\partial T_e^{(1)}}{\partial z}\bigg|_{z=0} = k_2 \frac{\partial T_e^{(2)}}{\partial z} \tag{1.5}$$

$$T_e^{(1)}|_{z=0} = T_e^{(2)} \tag{1.6}$$

$$T_e^{(2)}|_{z\to\infty} = 0. \tag{1.7}$$

The source term originally presented in the body of the first equation in (1.3) is introduced through the boundary condition for free interface of gold (1.4) where R is the reflection coefficient, I is the intensity of laser pulse and $f(t)$ is its temporal distribution. The interface between gold and cobalt is supposed to be ideal that is why we apply the condition of the continuity of the heat flow for electronic temperature as it follows from (1.5). Third condition (1.6) stands for non-scattering transport of electrons through the interface between gold and

cobalt, thus electrons do not lose energy. Final term (1.7) stands for an absorbing boundary condition.

After rewriting and rearranging of (1.3) we obtain :

$$\frac{\partial^2 T_e^{(1,2)}}{\partial z^2} - \frac{1}{D_{1,2}}\left[\frac{\partial T_e^{(1,2)}}{\partial t} - \frac{(T_e^{(1,2)} - T_i^{(1,2)})}{\tau_{1,2}}\right] = 0$$
$$\left(\frac{C_i}{C_e}\right)^{(1,2)} \frac{\partial T_i^{(1,2)}}{\partial t} - \frac{(T_e^{(1,2)} - T_i^{(1,2)})}{\tau_{1,2}} = 0, \tag{1.8}$$

where $D_{1,2} = k_{1,2}/C_e^{(1,2)}$ is the electron diffusivity parameter and $\tau_{1,2} = C_e^{(1,2)}/g_{1,2}$ is the characteristic time for the electron heat release. One of the most elegant ways to solve coupled nonlinear differential equations (1.8) is to do it in the frequency domain by applying the Fourier transform (FT)

$$\hat{F}(w,z) = \int_{-\infty}^{+\infty} F(t,z)e^{iwt}dt. \tag{1.9}$$

After application of FT to equations (1.8) we obtain

$$\frac{\partial^2 \hat{T}_e^{(1,2)}}{\partial z^2} - \frac{1}{D_{1,2}}\left[(iw)\hat{T}_e^{(1,2)} - \frac{(\hat{T}_e^{(1,2)} - \hat{T}_i^{(1,2)})}{\tau_{1,2}}\right] = 0 \tag{1.10}$$
$$\left[(iw)\left(\frac{C_i}{C_e}\right)^{(1,2)} + \frac{1}{\tau_{1,2}}\right]\hat{T}_i^{(1,2)} - \frac{\hat{T}_e^{(1,2)}}{\tau_{1,2}} = 0. \tag{1.11}$$

The same should be done also for all the boundary conditions (1.4) - (1.7)

$$k_1 \frac{\partial \hat{T}_e^{(1)}}{\partial z}\bigg|_{z=-H} = -(1-R)I\hat{F}(w) \tag{1.12}$$
$$k_1 \frac{\partial \hat{T}_e^{(1)}}{\partial z}\bigg|_{z=0} = k_2 \frac{\partial \hat{T}_e^{(2)}}{\partial z} \tag{1.13}$$
$$\hat{T}_e^{(1)}|_{z=0} = \hat{T}_e^{(2)} \tag{1.14}$$
$$\hat{T}_e^{(2)}|_{z\to\infty} = 0 \tag{1.15}$$

where $\hat{T}_e$ is the temperature at frequency domain.

We can rearrange Eq. (1.11) to express $\hat{T}_i^{(1,2)}$ in the following form

$$\hat{T}_i^{(1,2)} = \frac{\hat{T}_e^{(1,2)}}{1 + iw\left(\frac{C_i}{C_e}\right)^{(1,2)}\tau_{1,2}} \tag{1.16}$$

and by substitution into Eq. (1.10) we obtain a closed form equation for $\hat{T_e}^{(1,2)}$ without the lattice temperature

$$\frac{\partial^2 \hat{T_e}^{(1,2)}}{\partial z^2} + \frac{-iw}{D_{1,2}} \left[1 - \frac{(C_i/C_e)^{(1,2)}}{1 + (iw)(C_i/C_e)^{(1,2)}\tau_{1,2}} \right] \hat{T_e}^{(1,2)} = 0 \tag{1.17}$$

The term from the left side of $\hat{T_e}^{(1,2)}$ in Eq. (1.17) is the Maxwell wave number $p_{1,2}$, that we consider for definiteness to have positive real parts

$$p_{1,2} = \sqrt{\frac{-iw}{D_{1,2}} \left[1 - \frac{(C_i/C_e)^{(1,2)}}{1 + (iw)(C_i/C_e)^{(1,2)}\tau_{1,2}} \right]}. \tag{1.18}$$

Electronic temperatures in gold and cobalt from Eq. (1.17) take the next general form

$$\begin{aligned} \hat{T_e}^{(1)} &= c_{11}e^{-p_1 z} + c_{12}e^{p_1 z} \\ \hat{T_e}^{(2)} &= c_{21}e^{-p_2 z} + c_{22}e^{p_2 z}. \end{aligned} \tag{1.19}$$

To determine all the constants we apply the boundary conditions (1.12) - (1.15). From (1.15) it follows that $c_{22} = 0$. Using (1.14) it can be shown that

$$c_{11} + c_{12} = c_{21}. \tag{1.20}$$

After application of the boundary condition (1.13) we found that

$$-k_1 p_1 c_{11} + k_1 p_1 c_{12} = -k_2 p_2 c_{21}. \tag{1.21}$$

From (1.12) it follows that :

$$-k_1 p_1 c_{11} e^{p_1 H} + k_1 p_1 c_{12} e^{-p_1 H} = -(1 - R) I F(w). \tag{1.22}$$

After substitution of c_{21} from (1.20) in (1.21) we can write the system of equations for c_{11} and c_{12} consisting of updated (1.21) and (1.22) as follows

$$\begin{aligned} c_{11}(-k_1 p_1 + k_2 p_2) + c_{12}(k_1 p_1 + k_2 p_2) &= 0 \\ -c_{11} k_1 p_1 e^{p_1 H} + c_{12} k_1 p_1 e^{-p_1 H} &= -(1 - R) I F(w). \end{aligned} \tag{1.23}$$

To solve such system we rewrite it into the next matrix form

$$\begin{pmatrix} (-k_1 p_1 + k_2 p_2) & (k_1 p_1 + k_2 p_2) \\ -k_1 p_1 e^{p_1 H} & k_1 p_1 e^{-p_1 H} \end{pmatrix} \begin{pmatrix} c_{11} \\ c_{12} \end{pmatrix} = \begin{pmatrix} 0 \\ -(1 - R) I F(w) \end{pmatrix} \tag{1.24}$$

where principle determinant Δ_0 is given by

$$\Delta_0 = k_1 p_1 \left[(k_2 p_2 - k_1 p_1) e^{-p_1 H} + (k_2 p_2 + k_1 p_1) e^{p_1 H}. \right] \tag{1.25}$$

By applying the Cramer's rule it is easy to show that coefficients c_{11} and c_{12} are taking the next form

$$\begin{aligned} c_{11} &= (1-R) IF(w) \frac{k_1 p_1 + k_2 p_2}{\Delta_0} \\ c_{12} &= (1-R) IF(w) \frac{k_1 p_1 - k_2 p_2}{\Delta_0}. \end{aligned} \tag{1.26}$$

And the last coefficient c_{21} is the sum of c_{11} and c_{12} as it follows from (1.20)

$$c_{21} = (1-R) IF(w) \frac{2 k_1 p_1}{\Delta_0}. \tag{1.27}$$

Let us express electron temperature $\hat{T}_e$ at the interface between two metals at $z = 0$ on the basis of the solution

$$\hat{T}_e(w, z=0) = \frac{(1-R) IF(w) 2 k_1 p_1}{k_1 p_1 (k_2 p_2 - k_1 p_1) e^{-p_1 H} + (k_2 p_2 + k_1 p_1) e^{p_1 H}}, \tag{1.28}$$

after rearrangement

$$\hat{T}_e(w, z=0) = \frac{(1-R) IF(w)}{k_2 p_2 + k_1 p_1} \left[\frac{1}{1 + \frac{k_2 p_2 - k_1 p_1}{k_2 p_2 + k_1 p_1} e^{-2 p_1 H}} \right] e^{-p_1 H} \tag{1.29}$$

We can simplify Eq. (1.29) using the following approximations:

- Evaluate everything at acoustic frequencies $\omega \sim \omega_{ac} \sim 1/\tau_{ac}$ so that the term

  $$\omega_{ac} \tau_{1,2} \frac{C_i}{C_e}^{(1,2)} >> 1$$

  this will appropriate the Maxwell wavenumber as follows

  $$p_{1,2}^2 \simeq \left(-\frac{i\omega}{D_{1,2}} \right) \left(1 + \frac{1}{i\omega\tau_{1,2}} \right). \tag{1.30}$$

- The next assumption is that $\omega_{ac} \tau_{1,2} << 1$ which leads to

  $$p_{1,2} \simeq \frac{1}{\sqrt{D_{1,2} \tau_{1,2}}} = \frac{1}{\sqrt{k_{1,2}/g_{1,2}}}. \tag{1.31}$$

Now expression of electron temperature (1.29) with simplified p take the following form

$$\hat{T}_e(w, z=0) = \frac{(1-R)IF(w)}{\sqrt{k_2 g_2} + \sqrt{k_1 g_1}} \left[\frac{1}{1 + \frac{\sqrt{k_2 g_2} - \sqrt{k_1 g_1}}{\sqrt{k_2 g_2} + \sqrt{k_1 g_1}} e^{-\frac{2H}{\sqrt{k_1/g_1}}}} \right] e^{-\frac{H}{\sqrt{k_1/g_1}}} \tag{1.32}$$

The lattice temperature $\hat{T}_i$ is given by (1.16) and by substitution of electron temperature $\hat{T}_e$ from (1.32) will be

$$T_i^{(\hat{1},2)} = \frac{1}{(C_i/C_e)^{(1,2)}\,\tau_{1,2}} \frac{(1-R)IF(w)}{-i\omega} \frac{\frac{1}{1+\frac{\sqrt{k_2 g_2} - \sqrt{k_1 g_1}}{\sqrt{k_2 g_2} + \sqrt{k_1 g_1}} e^{-\frac{2H}{\sqrt{k_1/g_1}}}}}{\sqrt{k_2 g_2} + \sqrt{k_1 g_1}} e^{-\frac{H}{\sqrt{k_1/g_1}}}. \tag{1.33}$$

The inverse FT of the term $\frac{(1-R)IF(w)}{-i\omega}$ in (1.33) will provide total absorbed laser fluence $\Theta(t)$ that will describe quasi-instantaneous lattice heating.

Finally, the lattice temperature will be given by

$$T_i^{(1,2)} = \frac{g_{1,2}}{C_i^{(1,2)}} \frac{(1-R)\Theta(t)}{\sqrt{k_2 g_2} + \sqrt{k_1 g_1}} \frac{1}{1 + \frac{\sqrt{k_2 g_2} - \sqrt{k_1 g_1}}{\sqrt{k_2 g_2} + \sqrt{k_1 g_1}} e^{-\frac{2H}{\sqrt{k_1/g_1}}}} e^{-\frac{H}{\sqrt{k_1/g_1}}}. \tag{1.34}$$

In Eq. (1.34) the exponential term in denominator $\sqrt{k_1/g_1}$ is the diffusion length ζ_{diff} defined in the beginning of this chapter, that determine the profile of heat penetration.

By analyzing the expression of the lattice temperature given by Eq. (1.34) we can admit that there is a term responsible for different heating in gold and cobalt given by the ratio between electron phonon coupling g and lattice heat capacity C_i. Therefore to estimate overheating of gold as compared to cobalt layers we can divide lattice temperature of cobalt and gold at the interface using Eq. (1.34) so that

$$\frac{T_i^{Co}}{T_i^{Au}} \simeq \frac{(g/C_i)^{Co}}{(g/C_i)^{Au}} \tag{1.35}$$

By substitution values from Table 3.2 given in 3.2.1 we obtain the value of overheating equal to 13.5 that will be checked afterwards in the section of data analysis.

However, sometimes during solving of differential equations the division by zero in the frequency domain occurs, therefore leading to numerical problems when returning back to time domain. That is why another integral formula for the calculation of lattice temperature can be derived. For that we need to rearrange second term in Eq. (1.8) :

$$\frac{\partial T_i^{(1,2)}}{\partial t} + \frac{1}{(g/C_i)^{(1,2)}} T_i^{(1,2)} = \frac{1}{(g/C_i)^{(1,2)}} T_e^{(1,2)}(z,t). \tag{1.36}$$

Let's suppose that the solution of differential equation has a classical form

$$T_i^{(1,2)} = A^{(1,2)} e^{-\frac{t}{(g/C_i)^{(1,2)}}}, \tag{1.37}$$

we can substitute in Eq. (1.36) and after rearrangement it will look as follows

$$\frac{\partial A^{(1,2)}}{\partial t} = \frac{1}{(g/C_i)^{(1,2)}} T_e^{(1,2)}(z,t) e^{-\frac{t}{(g/C_i)^{(1,2)}}}. \tag{1.38}$$

Finally, integration of Eq. (1.38) provides the value of the coefficient $A^{(1,2)}$ and by substitution into Eq. (1.37) the lattice temperature can be expressed as follows

$$T_i^{(1,2)}(z,t) = \frac{1}{(g/C_i)^{(1,2)}} \int_0^t T_e^{(1,2)}(z,t') e^{-\frac{t-t'}{(g/C_i)^{(1,2)}}} dt'. \tag{1.39}$$

1.2 Thermal transport through the interface

In the previous section we have seen the ultrafast diffusion of electrons through an ideal interface. However, this is not the case in real world, where interface plays a crucial role in the thermal transport[34,35]. An interface is a surface forming a common boundary between two portions of matter. Therefore it is a boundary that indicates the modification of elastic and electronic properties of a medium. Therefore, some carriers of heat that can easily travel in first medium may not be allowed in the second medium. As an example, we can consider the case of a gold film deposited on a dielectric sapphire substrate. When the gold layer is heated by femtosecond laser pulse it could cool down into the substrate by transferring electrons and phonons through the interface. However, sapphire has a big band gap which restricts conduction of electrons and therefore only phonons can heat the substrate. For this case we can expect big thermal resistance at the interface between gold and sapphire because only one heat carrier is involved in thermal transport. The characteristics of an interface to resist the thermal flow is known as thermal boundary or Kapitza resistance. In the general case of metal-dielectric and dielectric-dielectric interfaces the impact of electronic transport is negligible, that is why thermal transport is examined within the framework of lattice vibrations theory[36,34] also called Acoustic Mismatch Model (AMM). However, there is another approach for estimation of thermal resistance of the interface the Diffuse Mismatch Model (DMM) that is based on the phononic density of states[37,38].

In contrast for metal-metal interface, the contribution of the electrons in thermal transport can be as high as 90% and only 10% are attributed to phonons[16].

1.2.1 Thermal boundary resistance (Kapitza resistance)

Thermal boundary resistance or Kapitza resistance is a parameter that determine the rate of an interface to resist the thermal flow. First experiments that showed the temperature drop between two mediums was performed by Kapitza in 1941[39], where he showed drop of temperature between liquid helium and solid. This phenomenon was explained by analogy with a resistance placed in electric circuit leading to decrease of the output voltage.

To illustrate the Kapitza resistance we consider the case when two materials are in contact and one of them is heated with a constant heat flux Q. The difference in lattice and electronic structures between these two materials lead to scattering of phonons and electrons from the interface boundary. Scattered carriers do not penetrate into adjacent material leading to discontinuity of the temperature ΔT. Therefore in the simplest case the Kapitza resistanceR_{Kap} describe this discontinuity

$$R_{Kap} = \frac{1}{G_{Kap}} = \frac{Q}{\Delta T}. \tag{1.40}$$

In contrast to Kapitza resistance there is its inverse referred as thermal boundary conductance $G_{Kap} = 1/R_{Kap}$.

The notion of the Kapitza resistance can be applied not only to electrons and phonons but also to magnons[40]. Therefore the total Kapitza resistance is a sum of these three contributions

$$\frac{1}{R_{Kap}} = \frac{1}{R_{Kap}^{phonon}} + \frac{1}{R_{Kap}^{electron}} + \frac{1}{R_{Kap}^{magnon}}. \tag{1.41}$$

However the repartition of contributions will vary according to the nature of the materials forming the interface. Therefore the Kapitza resistance of the interface between two dielectrics or dielectric and metal phononic has the dominant phonon term R_{Kap}^{phonon}. The Kapitza resistance of the metal-metal interface will have the dominant electron term $R_{Kap}^{electron}$ and small phonon contribution[41,16] R_{Kap}^{phonon}. If the interface is formed between two magnetic materials, the magnonic term R_{Kap}^{magnon} can be also involved in the thermal transport[40]. But extraction of the separate contributions is a very challenging task, that is why only the total Kapitza resistance R_{Kap} is widely used.

Furthermore we will review basic models dedicated to formalize the Kapitza resistance.

1.2.2 Acoustic Mismatch Model (AMM)

The first analytic approach devoted to explain the temperature jump at the interface of liquid helium and copper was AMM[36]. The core assumption of this model is that the phonon wavelengths are larger than the lattice spacing parameter a. As a result, the medium of propagation can be treated as continuum acoustic. The interface between two media is

supposed to be plane and phonons are treated like propagating plane waves. Using all these assumptions the phonons incident on the interface undergo Snell's law and the phonon transmission coefficient T_{12} can be developed by analogy with the Fresnel optics

$$T_{12} = \frac{4Z_1 \cos\theta_1 Z_2 \cos\theta_2}{(Z_1 \cos\theta_1 + Z_2 \cos\theta_2)^2}, \tag{1.42}$$

where Z is the acoustic impedance : $Z = \rho c_s$ with the density of material ρ and the sound velocity c_s; θ is the angle of incidence to plane normal.

From the other hand the reflection coefficient R_{12} will be

$$R_{12} = \left| \frac{Z_1 \cos\theta_1 - Z_2 \cos\theta_2}{Z_1 \cos\theta_1 + Z_2 \cos\theta_2} \right|^2. \tag{1.43}$$

Such rough model serves as an upper limit of the estimation of the thermal transport through the interface. There are many inaccuracies in AMM. It does not take into account the spectrum difference of the two mediums, because by definition $T_{12} = T_{21}$. In reality, it is possible that a high-frequency phonon from medium 1 can not be transmitted into medium 2 because such frequency is not present in his spectrum, as a result $T_{12} \neq T_{21}$. The assumption that thermal transport can be described by propagating plane waves is also very rough because in reality it has diffusive nature.

The expression of Kapitza resistance can be calculated as an integral of the transmission coefficient T_{12}. By considering the flux from medium 1 to 2 striking at different angles θ the expression of the Kapitza resistance will look as follows[42]

$$\frac{1}{R_{Kap}} = \frac{1}{2} C_1 \upsilon_1 \int_0^{2\pi} T_{12}(\cos\theta) \cos\theta \, d\cos\theta, \tag{1.44}$$

where C_1 is the volumetric specific heat and υ_1 is the phonon group velocity of the first medium.

1.2.3 Diffusive Mismatch Model (DMM)

The DMM model supposes that scattering of phonons is non-specular (diffusive) and supposes phonon memory loss (incident and transmitted/reflected phonons are unrelated). Under such consideration when the phonon arrives at the interface between two mediums it is completely unbounded from the previous path and direction of the movement, thus the transition is related only by the mismatch of the phonon density of states in both substances. Often, the DMM calculations are based on the Debye approximation (where DOS is a linear function). The expression of the transmission coefficient T_{12} from material 1 to 2 is given by

$$T_{12} = \int_0^{\pi/2} \frac{\upsilon_2 D_2}{\upsilon_1 D_1 + \upsilon_2 D_2} \cos\theta \sin\theta d\theta. \tag{1.45}$$

On the basis of the transmission coefficient T_{12}, we can calculate the Kapitza resistance[42] of an interface to be

$$\frac{1}{R_{Kap}} = \frac{1}{4} C_1 \upsilon_1 T_{12} \tag{1.46}$$

We can analyze both expressions from AMM (1.42) and DMM (1.45) in the case of the interface between two identical materials. In specular approximation the AMM gives 100% of transmission for phonons, but by contrast the DMM will produce 50% of transmission. By this simple example the overestimation of the AMM and underestimation of the DMM can be revealed. For metal-metal interface generally, results of both expressions (1.44) and (1.46) reasonably differ only by less than 30%[38]. For metal-dielectric interface between gold and sapphire it is even smaller[37].

1.2.4 DMM for electrons in metals

Previously discussed AMM and DMM models are related only to the phononic contribution of the Kapitza resistance. However, there is a model based on the diffuse mismatch logic for electron contribution of the interface resistance[16] that describes more accurately thermal properties of interface between two metals.

As previously, the main assumption is that all electrons scatter diffusely when encountering the interface. Such description can be validated when the interface between two metallic layers forming the alloys with dimensions smaller than few atomic layers[43,44]. In case when the deposition technique can validate previous condition (for example for the case of magnetron sputter deposition or molecular beam epitaxy) the DMM for electrons can be used.

The transition from DMM for phonons to DMM for electrons is straightforward. The only difference is concerned with the distinction of electrons by their energies E. That is why both velocity and DOS are functions of energy, being $\upsilon_i(E)$ and $D_i(E)$ respectively, where i denotes the material. In such case the transmission coefficient T_{12} form metal 1 to metal 2 is given by

$$T_{12}(E) = \int_0^{\pi/2} \frac{\upsilon_2(E) D_2(E)}{\upsilon_1(E) D_1(E) + \upsilon_2(E) D_2(E)} \cos\theta \sin\theta d\theta. \tag{1.47}$$

In the simplified model of the metal, such as degenerate metal with an isotropic Fermi surface, the Kapitza resistance can be expressed as

$$\frac{1}{R_{Kap}^{electron}} = \frac{1}{2} \upsilon_1(E_F) T_{12}(E_F) \int_0^{\infty} E \frac{dN_1(E,T)}{dT} dE, \tag{1.48}$$

where $N_1(E,T)$ is the density of occupied states of energy E at temperature T. The integral term in the denominator can be replaced by the electron heat capacity per unit volume

C_e, which is proportional to $D(E_F)$ and temperature T in the case of free electron gas by $C_e = (\pi^2/3)D(E_F)k_B^2 T = \gamma T$. Finally, the Kapitza resistance takes the following form

$$\frac{1}{R_{Kap}^{electron}} = \frac{Z_1 Z_2}{4(Z_1 + Z_2)}, \tag{1.49}$$

where Z_i is the product of the electron heat capacity $C_e = \gamma T$ and the Fermi velocity υ_F for a side i, $Z_i = \gamma T \upsilon_F$.

1.3 TTM for bimetallic structure with Kapitza resistance

It is possible to make few modifications in the TTM model to take into account the electron Kapitza resistance. First of all, the boundary condition given by Eq. (1.14) should be rewritten by introducing the Kapitza resistance R_{Kap} which decreases the electron heat flow from gold to cobalt

$$(\hat{T_e}^{(1)} - \hat{T_e}^{(2)})|_{z=0} \;=\; R_{Kap} k_1 \frac{\partial \hat{T_e}^{(1)}}{\partial z}. \tag{1.50}$$

Also, an additional term should be added to boundary the condition given by Eq. (1.21) resulting in

$$c_{11} + c_{12} - R_{Kap} k_1 p_1 (c_{11} - c_{12}) = c_{21} \tag{1.51}$$

Using those modified boundary conditions, we can rewrite in the same manner the matrix form of equation resulting in

$$\begin{pmatrix} (-k_1 p_1 + k_2 p_2 - K_{Kap}) & (k_1 p_1 + k_2 p_2 + K_{Kap}) \\ -k_1 p_1 e^{p_1 H} & k_1 p_1 e^{-p_1 H} \end{pmatrix} \begin{pmatrix} c_{11} \\ c_{12} \end{pmatrix} = \begin{pmatrix} 0 \\ -(1-R) I F(w) \end{pmatrix} \tag{1.52}$$

where K_{Kap} is a coefficient that is given by $K_{Kap} = R_{Kap} k_1 k_2 p_1 p_2$. The new principle determinant Δ_0 will be

$$\begin{aligned} \Delta_0 = \;& k_1 p_1 (k_2 p_2 - k_1 p_1 - K_{Kap}) e^{-p_1 H} + \\ & + k_1 p_1 (k_2 p_2 + k_1 p_1 + K_{Kap} e^{p_1 H}. \end{aligned} \tag{1.53}$$

Consequently, the coefficients c_{11}, c_{12} and c_{21} take the following form

$$c_{11} \;=\; (1-R) I F(w) \frac{k_1 p_1 + k_2 p_2 + K_{Kap}}{\Delta_0}$$

$$
\begin{aligned}
c_{12} &= (1-R)IF(w)\frac{k_1 p_1 - k_2 p_2 + K_{Kap}}{\Delta_0} \\
c_{21} &= (1-R)IF(w)\frac{2k_1 p_1 + 2K_{Kap}}{\Delta_0}.
\end{aligned} \tag{1.54}
$$

We can admit that if we put $R_{Kap} = 0$ all the coefficients c_{11}, c_{12}, c_{21} will transform into Eq. (1.26) and Eq. (1.27) where no boundary resistance is considered. Subsequent procedure of the calculation of the lattice temperature remains the same as previously.

2

Opical Pump-Probe Technique

Picosecond acoustics technique is an experimental all-optical pump-probe technique used for the study of electronic and elastic properties of materials using ultrafast laser pulses. This technique is of high interest for characterizations and studies of nanostructured materials, because the frequencies of generated acoustics lie in the 10-1000 GHz range[45,46,47].

Schematic diagram explaining the principle of operation of this technique is shown in Fig. 2.1, where a metallic film is illuminated by two femtosecond laser pulses. The pump pulse is used to excite the coherent acoustic pulse within the skin layer at the free surface side. Then the acoustic pulse (coherent longitudinal phonons) propagates at the sound velocity towards the substrate illuminated by weaker femtosecond probe pulse. This pulse monitors the changes in optical constants, such as reflectivity coefficient R, within its own skin layer. At the moment, when the acoustic pulse reaches the probe skin layer it exerts changes in the reflectivity coefficient which is detected by photodiode.

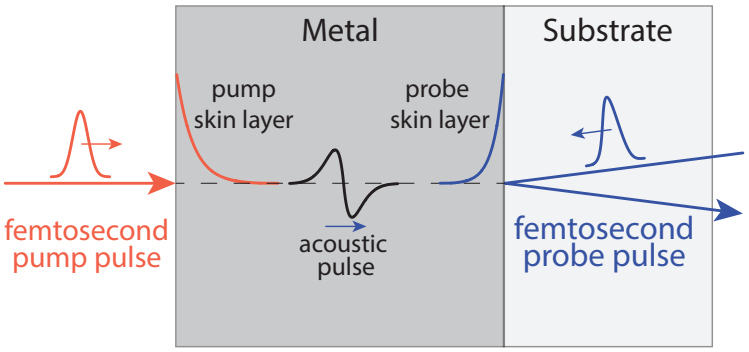

Figure 2.1: Diagram of the pump-probe experiment showing the profile of heated region by absorbed pump pulse within the skin layer δ; this excitation region then emits the acoustic pulse of bipolar shape (which is true for all free-surface-excited films); the acoustic pulse induces the change of the density and modifies the reflectivity coefficient R on the other side of the film; these acoustically induced changes are detected by the probe pulse from a photodiode as a variation of the light intensity.

2.1 Thermo-elastic generation of strain and stress

Under laser irradiation, the kinetic energy of the solid system increases from the absorption of photons. The resulting excess energy forces the atoms located in proximity one with another to vibrate with bigger amplitudes and frequencies, moving them far away from original positions. The collective displacement of excited atoms leads to change the volume of the solid as well as of its linear dimensions. The coherent component of such collective displacement is an acoustic pulse and the driving mechanism of such generation is called thermal expansion. The possibility to generate acoustics by heating has been studied by White[48]. He considered the problem in one dimension without taking into account the diffraction effect and also neglected effects of diffusion. He supposed that the profile of generated acoustics matches the deposition heat profile.

In order to determine what kind of acoustics can be generated via thermal expansion the effect on stress-strain relation should be introduced[49]. In the case of isotropic solids there is no need to use tensor notation, therefore the relative displacement of the particles, called thermal strain η will be given by

$$\eta_z = \frac{\partial u_z}{\partial z} = \alpha \Delta T(z) \tag{2.1}$$

where u is the z^{th} component of the displacement, α is the coefficient of linear thermal expansion and $\Delta T(z,t)$ is the change of the temperature induced by the laser pulse relative to the initial temperature T_0.

Thermal component of the stress can be found under consideration that solid has expanded (at $t = \infty$ the stress will leave the region of excitation $\sigma_{zz} = 0$) and in absence of thermal diffusion we will have

$$\sigma'_z = -3B\alpha \Delta T(z) \tag{2.2}$$

where B is the bulk modulus of elasticity defined as $B = \lambda + \frac{2}{3}\mu$.

And the total stress σ is a sum of the static thermal stress and propagating stress looks as follows[50]

$$\sigma_z = (2\mu + \lambda)\eta_z + \sigma'_z \tag{2.3}$$

where λ and μ are the elastic constants. The propagation of strain and the static thermal stress will be covered in the next section.

2.2 Strain propagation in monolayer

Dynamic processes of longitudinal strain propagation in metallic films shown in Fig. 2.2 which take place just after thermo-elastic generation can be examined by solving the equation of elasticity

$$\rho \frac{\partial^2 u_z}{\partial t^2} = \frac{\partial \sigma_z}{\partial z}, \tag{2.4}$$

where ρ is the density of the material. But before solving this equation, the correct expression of stress σ_{zz} should be determined. It can be done by substitution of thermal component from Eq. (2.3) into (2.2) resulting in

$$\sigma_z = (2\mu + \lambda)\eta_z - 3B\alpha\Delta T(z) = \rho c_s^2 \eta_z - 3B\alpha\Delta T(z), \tag{2.5}$$

where c_s is the sound velocity.

The next step is to determine the temperature spatial profile $\Delta T(z)$. It should decay exponentially following the skin layer profile and the amplitude can be expressed for two cases : for time $t < 0$ to be zero $\Delta T(z,t) = 0$ and otherwise, for $t > 0$ to be

$$\Delta T(z,t) = \frac{(1-R)Q}{AC\delta} e^{-\frac{z}{\delta_{skin}}}, \tag{2.6}$$

where R is the reflectivity, Q is the deposited energy by the pump pulse, A is the area of the film that was illuminated by pump pulse, C is the specific heat capacity. The boundary condition restricts the stress to be zero $\sigma_{zz} = 0$ at $z = 0$ that give a static strain term η_0 from Eq. (2.5)

$$\eta_0 = \frac{3B\alpha(1-R)Q}{\rho c_s^2 AC\delta_{skin}}. \tag{2.7}$$

The following initial conditions can be applied to single film case: $\eta_{zz} = 0$, $\partial\eta_{zz}/\partial t = 0$ and $u_z = 0$ everywhere at $t < 0$. The solution of the elasticity Eq. (2.4) for a given boundary and initial conditions leads to a three component solution for strain[1]

$$\eta_z = \eta_0 \left(e^{-z/\delta_{skin}} - \frac{1}{2}\left[e^{-|z+c_s t|/\delta_{skin}} + e^{-|z-c_s t|/\delta_{skin}} \operatorname{sign}(z - c_s t) \right] \right). \tag{2.8}$$

Calculated strain distribution for three different times is shown in Fig. 2.2. The first static exponential term represents the pure thermal strain at time $t = \infty$, shown as a red solid line. It is static because we neglect the heat diffusion. Second exponential term is shown for two consecutive times as blue dashed line and as blue solid line. We can admit that they both have bipolar shapes. This is true because according to Eq. (2.8) two strains are propagating initially in opposite directions. But after total reflection from the free interface one part of

the strain changes its sign and then propagates in the same direction as the first one.

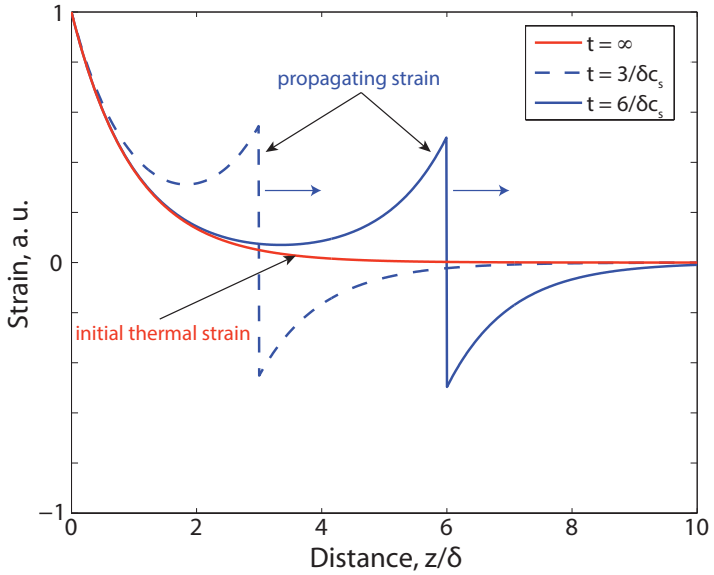

Figure 2.2: Calculated strain distribution generated by the heat absorbed within the skin depth δ as a function of thickness z/δ for different time instances. Strain is propagating with a sound velocity c_s. Diffusion is neglected.

2.3 Strain propagation in a multilayer

We have seen that strain propagation in the case of a single layer structure with only one interface is a quite simple and clear process. But in the case of a multilayer structure with multiple interfaces, derivation of the analytic expression is a more sophisticated problem. That is why we used numeric computations on the basis of the finite-difference method, because it is easy to implement and the results are consistent with experimental observations.

The scheme of application of such method is shown in Fig. 2.3, where 1D structure containing layer of gold of thickness d_1 followed by layer of cobalt of thickness d_2 and finalized by layer of sapphire is discretized in time and space. The discretization is very important issue of finite-difference algorithm. Mesh in time Δt and space Δd should be related one to another. This governing factor is the sound speed c_s. For definiteness, if we fix the time step Δt the discretization mesh size should satisfy the following relation

$$dz_{1,2,3} = \Delta t \cdot c_s^{(1,2,3)}. \tag{2.9}$$

This relation allows to ensure that strain will always propagate by a distance Δd inside each material according to its sound speed c_s by the time Δt. This important condition is illustrated in Fig. 2.3, where gold blocks are of smaller size than that of cobalt because by the time Δt the strain in gold will overcome roughly two times smaller distance than the strain in cobalt, because of smaller sound speed (see Table 2.1).

Table 2.1: Sound velocities of gold, cobalt and sapphire

Property\Material	Gold (1)	Cobalt (2)	Sapphire (3)	Unit
Sound velocity	3450[51]	6300[52]	11300[25]	$[c_s] = [ms^{-1}]$

To take into account all the reflections of strains taking place at the multiple interfaces (free interface of gold, gold/cobalt and cobalt/sapphire) we introduce two strains propagating in opposite directions. The first strain η_+ propagates in $+z$ direction and the second η_- propagates in $-z$ direction as it is shown in Fig. 2.3 by arrows. As an example, we can consider the situation when at time t_0 the strain η is generated at some point inside the gold layer as shown by red dot in Fig. 2.3. At later time t_1 the strain η splits into two : one half of strain η_+ is propagating in $+z$ direction and another η_- in the opposite direction without interaction among themselves. This model consider no attenuation and no dispersion.

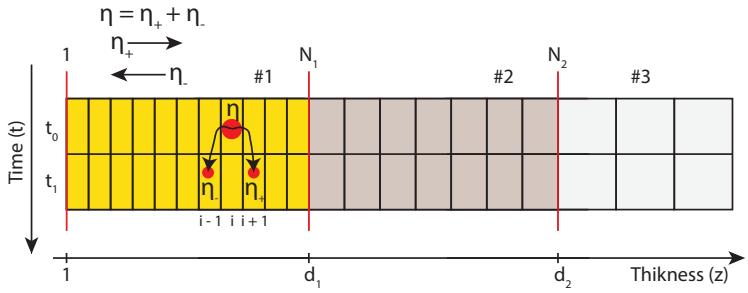

Figure 2.3: Sketch of finite difference approach for discretization of gold/cobalt/sapphire structure. Horizontal axis shows mesh in space which is proportional to sound speed c_s in each material, that is why the blocks in gold are smaller than those in cobalt. Vertical axis stands for equidistant mesh in time.

When the strain is approaching any interface, the amount of transmitted and reflected energy is governed by the relation of acoustic impedances Z in two adjacent mediums. The impedance depends on the density ρ and the sound velocity c_s of the medium and is given by $Z = \rho c_s$. In general, the formulas that govern the reflections and transmissions of strain through the interfaces are given by

$$R_{12} = \frac{Z_2 - Z_1}{Z_1 + Z_2} \tag{2.10}$$

$$R_{21} = \frac{Z_1 - Z_2}{Z_1 + Z_2} \tag{2.11}$$

$$T_{12} = \frac{2Z_1}{Z_1 + Z_2}\frac{v_1}{v_2} \tag{2.12}$$

$$T_{21} = \frac{2Z_2}{Z_1 + Z_2}\frac{v_2}{v_1}. \tag{2.13}$$

When the strain is transmitted to another medium with a different acoustic speed it experiences a change of its spatial distribution in order to preserve its temporal duration. Still, the conservation law should be satisfied, it means that the integral of the strain should

remain the same, that is why there is a preserving factor υ_1/υ_2 which increases the amplitude of the strain if it shrinks in space and decreases in the case of broadening.

To illustrate this concept we can consider the following example: the strain of arbitrary amplitude 1 and 10 ps FWHM duration is propagating from gold to cobalt. The spatial profile of such strain in gold is characterized by 34.5 nm, but after transmission into cobalt layer (where the acoustic speed is 1.82 times bigger) the strain is broadening 1.82 times and reaches 63 nm. Consequently, according to Eq. (2.12) the amplitude of strain transferred into cobalt layer will decrease to 0.59. However, such pair of metals like gold and cobalt might be considered as phase-match couple because of small losses of strain when the reflection takes place, because $R_{CoAu} = -R_{AuCo} = 0.09$, that means that only about 10% of strain is not transmitted through the interface between these two metals.

More formal representation of the algorithm of finite difference method for solving acoustic wave equation results in following expressions for propagation of the "positive" η_+ and "negative" η_- strains as well as formula for total strain η

$$\eta_+(t_{i+1}, z_j) = \eta_+(t_i, z_{j-1}) \tag{2.14}$$

$$\eta_-(t_{i+1}, z_j) = \eta_-(t_i, z_{j+1}) \tag{2.15}$$

$$\eta(t_i, z_j) = \eta_+(t_i, z_j) + \eta_-(t_i, z_j). \tag{2.16}$$

All the necessary boundary conditions for solving acoustic wave equation in the case of complex gold/cobalt/sapphire structure can be transformed into the following expressions for both strain propagating in opposite directions:

1. The reflection of strain at the free interface at first point z_1 at $t+1$ for η_+ strain is given by

$$\eta_+(t_{i+1}, z_1) = -\eta_-(t_{i+1}, z_1). \tag{2.17}$$

2. The strain η_+ in first spatial point of cobalt layer at time $t+1$ should contain transmitted strain η_+ from gold to cobalt and also reflected strain η_- from cobalt/gold interface resulting in

$$\begin{aligned} \eta_+(t_{i+1}, z_{N_1+1}) &= T_{12}\eta_+(t_i, z_{N_1}) + \\ &+ R_{21}\eta_-(t_{i+1}, z_{N_1+1}). \end{aligned} \tag{2.18}$$

3. The strain η_- in the last gold point at $t+1$ should contain the strain η_+ reflected at gold/cobalt interface and also the strain η_- transmitted from cobalt to gold effecting in

$$\begin{aligned} \eta_-(t_{i+1}, z_{N_1}) &= T_{21}\eta_-(t_j, z_{N_1+1}) + \\ &+ R_{12}\eta_+(z_{N_1}, t_j). \end{aligned} \tag{2.19}$$

4. The last conditions describe the reflection and transmission of strain at cobalt/sapphire interface.

$$\eta_{-}(z_{N_2}, t_{j+1}) = R_{23}\eta_{+}(z_{N_2,t_j}) \tag{2.20}$$
$$\eta_{+}(z_{N_2+1}, t_{j+1}) = T_{23}\eta_{+}(z_{N_2}, t_j). \tag{2.21}$$

In the case when the thickness of the substrate is much bigger (few mm) than the thickness of bimetallic film, we can neglect the reflection of the strain at sapphire/air interface because the temporal domain of interest is much smaller than the back-forward propagation time in sapphire substrate.

The MATLAB script that performs the strain propagation is given in Appendix A.2.

Evaluation of the algorithm of strain propagation

Evaluation of the finide-difference algorithm for solving the acoustic wave equation was done using the data measured by recent magneto-plasmonic pump-probe experiment, where very same sample structure gold/cobalt/sapphire was used[25]. In this experiment the pump pulse is incident on the surface of cobalt as it is shown in Fig. 2.4, where after absorption of the energy within the skin layer electrons are able to diffuse on slightly bigger distances producing the profile of deposited heat. Therefore through thermo-elastic mechanism the strain pulse is generated and propagate towards the free interface of gold where it can be detected by surface plasmons within their 13 nm skin layer.

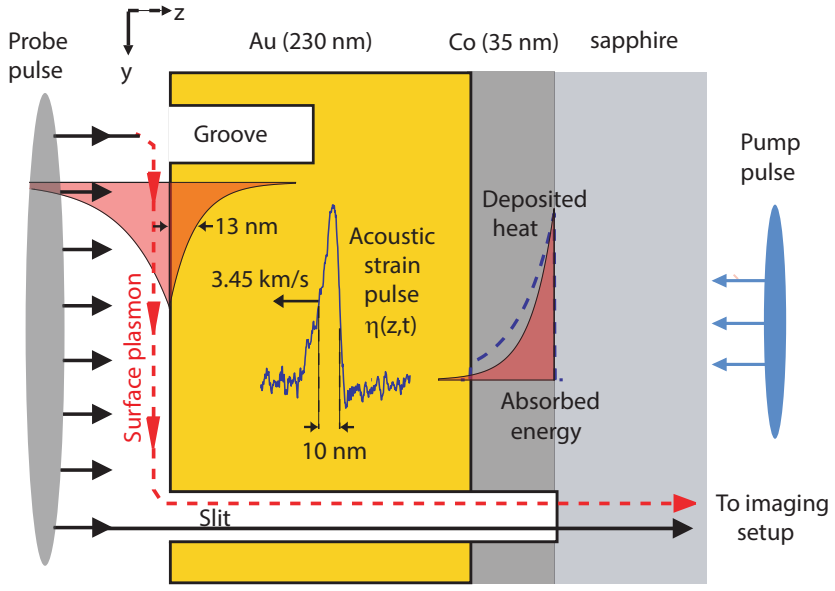

Figure 2.4: Scheme of the acousto-plasmonic pump-probe experiment[25], where acoustic strain is generated by laser absorption in the cobalt layer. This strain then propagates through the gold layer and interacts with surface plasmon wave-vector k_{sp} by modulation of the dielectric function ϵ_m.

To compare the experimental result with calculation we need first to calculate impedances of gold, cobalt and sapphire as well as all the reflection and transmission coefficients. Determined values of impedances are listed in Table. 2.2, where we can admit small difference in values for gold and cobalt as well as for cobalt and sapphire pairs. As a result of small differences between impedances, the reflection coefficients for these interfaces will be also small (only 10% of reflection).

Table 2.2: Values of acoustic impedances of the studied materials

Property\Material	Gold	Cobalt	Sapphire	Unit
Impedance	66585	56070	45200	[Z] = [kg $s^{-1}m^{-2}$]

Now we can use the value of the heat profile generated by a pump pulse in cobalt, which is equal to 18 nm[25] to define the spatial profile of the strain and solve the acoustic wave equation for the structure that has 230 nm of gold followed by 35 nm of cobalt on a sapphire substrate.

The illustration that shows the spatial profile of the calculated strain distribution is shown in Fig. 2.5. The first red solid line inside the structure shows the initial strain distribution for $t = 0$ ps, where there is only one exponential unipolar strain generated in the cobalt layer. At the time $t = 7$ ps, the strain propagating in two opposite directions leaves the cobalt layer and now is present inside both gold and sapphire layers with a small 10% tale occurred after the reflection at the cobalt/sapphire interface.

As it was discussed before, the strain spatial duration and amplitude change when according to the sound speed in the medium of propagation. That is why the strain amplitudes in gold and cobalt are different. Spatial profiles of strains also change, that can be observed by comparing strains in gold and sapphire at time $t = 7$ ps. Because of a factor of two in relation between cobalt and sapphire sound speeds, the spatial profile of the strain in sapphire is two times larger. By the time $t = 67$ ps, the strain pulse generated in cobalt ("first echo") will arrive to the detection surface and after total reflection with change of sign goes backward. This strain is involved in generation of two consecutive echoes ("second echo" and "third echo") by reflection at gold/cobalt and then at cobalt/sapphire interfaces, as shown by the last profile. Two last echoes will arrive to the probing side approximately around $t \approx 200$ ps.

In order to analyze experimental signal involving the plasmonic detection of acoustics the mechanism of interaction between the strain and the surface plasmons is briefly explained below.

Ultrashort acoustic pulse alters the dielectric function ϵ_m inside the metal by charge separation. This leads to modulation of the surface plasmon wave vector $k_{sp} = k_0\sqrt{\epsilon_m/(1+\epsilon_m)}$

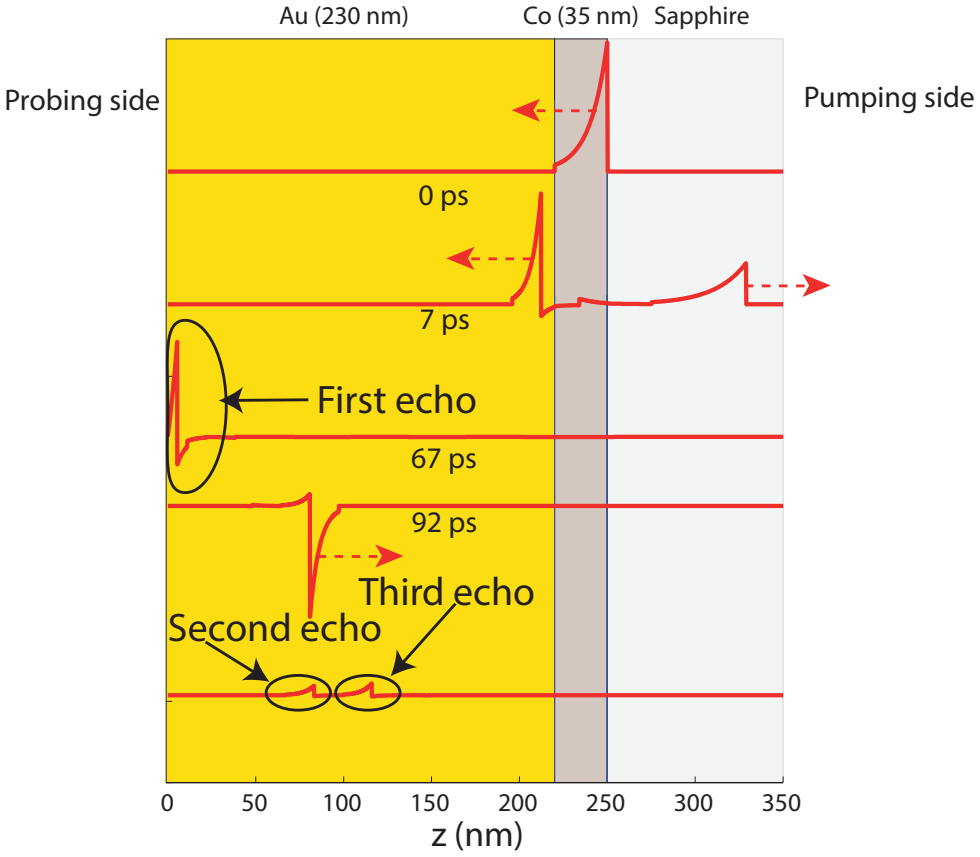

Figure 2.5: Spatial profiles of the strains η at different times t are shown as red solid lines. They demonstrate progressive propagation of the initially generated strain in cobalt layer by thermal expansion. Three consecutive echoes that should be detected at probing side are depicted by arrows. Second and third echoes are reflections of the strain shown for $t = 92$ ps at the gold/cobalt and the cobalt/sapphire interfaces respectively.

within the surface plasmon skin depth $\delta_{skin}^{sp} = 13$ nm at the gold/air iterface by

$$\delta k_{sp}(t) = -\frac{k_0}{2|\epsilon|\delta_{skin}} \int_0^\infty \eta(z,t) \exp(-|z|/\delta_{skin}^{sp}) dz \tag{2.22}$$

The measured signal is a convolution of the strain $\eta(z,t)$ with the exponential penetration of surface plasmons. Therefore, by integrating the strain distribution (calculated using finite-difference algorithm) within the skin depth δ_{skin}^{sp} of the surface plasmons it is possible to reproduce the experimental signal. The experimental data shown by blue solid line in Fig. 2.6 is the real part of the dielectric function ϵ_m without the thermal background. The fit curve is shown by red solid line. The strain distribution was smeared by the Gaussian with 2 nm (FWHM) to take into account the surface roughness. It is easy to see that even such simple approach allows to fit all three echoes simultaneously. The amplitudes of the strain pulses are in high agreement with experimental observation. Simulation curve can be optimized by taking into account slightly more complicated profile of the strain pulse[25] but this is not a primordial task for the evaluation of the efficiency of finite-difference algorithm.

By this example it was shown that the developed finite-difference algorithm can be used for the evaluation of the strain propagation inside nanostructures. The big advantage of this

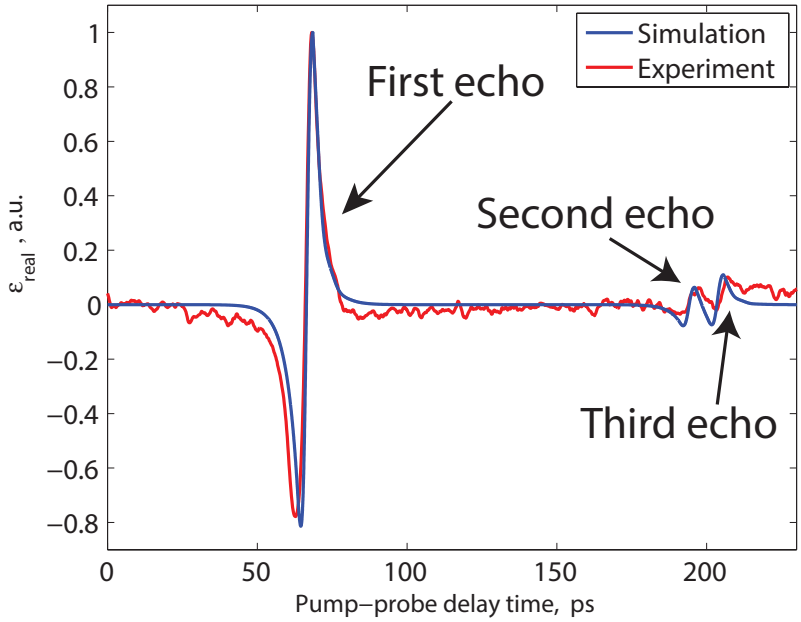

Figure 2.6: Real part of the dielectric function ϵ_m without thermal background is shown as the red solid line presenting three echoes explained earlier; Simulation curve (blue solid line) reproducing reasonably well all the echoes as well as their shape is the result of the propagation algorithm implementation and calculation using (2.22).

algorithm is the possibility to use an arbitrary initial strain distributions that can be very complex, as it will be shown in the data analysis chapter. However this algorithm does not take into account possible diffraction or dispersion effects during propagation in films.

2.4 Detection of strain

Optical methods being non-contact and nondestructive (for low fluences) give access to study wide range of physical properties. Huge progress in ultrafast pulsed lasers during several decades have enabled ultrasonic pump-probe measurements at femtosecond timescale for frequencies up to and beyond 1 THz range[45,47,46]. Among multiple methods for detection of the induced changes in the materials, the reflectivity measurement is one of the most widely used. It is based on the effect of change of the complex reflection coefficient $\tilde{n} = n + ik$ when coherent or incoherent phonons arrive within the skin depth of the probed surface.

In equilibrium, the amount of the light reflected from the surface of the material is governed by the screening of photons on the electron cloud formed by the overlap of electron clouds of multiple atoms. When a phonon interacts with the atom this leads to its displacement from the equilibrium position and to perturbation of the electronic structure. Therefore it is possible to indirectly observe arrival of phonons by examination of the variation of the reflectivity coefficient ΔR of the probe light reflected from the surface.

The theory that describes complex reflection coefficient change $\delta\tilde{r}(t)$ under the presence of acoustic strain $\eta(z,t)$ within the skin depth is well known[1,3,2] and the expression that

governs induced change of $\delta\tilde{r}(t)$ is given by

$$\frac{\delta\tilde{r}(t)}{\tilde{r}} = -i\frac{4\pi}{\lambda}\int_0^\infty \left(1 - \frac{2\tilde{n}}{1-\tilde{n}^2}\frac{d\tilde{n}}{d\eta}\exp\left[i\frac{4\pi}{\lambda}\tilde{n}z\right]\right)\eta(z,t)dz, \tag{2.23}$$

where $\tilde{n}$ is the complex refractive index with real n and imaginary k parts $\tilde{n} = n + i\cdot k$, $d\tilde{n}/d\eta$ is the photoelastic coefficient that governs how strong is the change of the refractive index with respect to the strain $d\tilde{n}/d\eta = dn/d\eta + idk/d\eta$.

When the detection take place on the free surface, the reflection of strain with change of a sign should be taken into account, that yields to

$$\frac{\delta\tilde{r}(t)}{\tilde{r}} = -i\frac{4\pi}{\lambda}\int_{-\infty}^{\infty}\left[1 - (A+iB)e^{i4\pi\tilde{n}c_s|t'-t|/\lambda}\right]\mathrm{sign}(t'-t)\eta(t')dt', \tag{2.24}$$

where, A and B are coupled dimensionless parameters[6] that depend on the photoelastic coefficient $d\tilde{n}/d\eta$ and the index of refraction $\tilde{n}$ as follows $A + iB = 2\tilde{n}(d\tilde{n}/d\eta)/(1-\tilde{n}^2)$.

Two types of signal can be extracted from Eq. (2.24) such as imaginary part providing phase information that gives the displacement of the measured surface[53,54] and the real part that gives reflectivity change $S(t)$ that we measure in our experiment

$$S(t) = \frac{\Delta R}{R} = 2\Re\left[\frac{\delta\tilde{r}(t)}{\tilde{r}}\right] = -i\frac{8\pi}{\lambda}\int_{-\infty}^{\infty}G(t'-t)\eta(t')dt' \tag{2.25}$$

where $G(t)$ is the sensitivity function of the material given by

$$G(t) = \left[A\sin(w_{Br}t) + B\cos(w_{Br}t)\,\mathrm{sign}(t)\right]e^{\frac{-|t|}{\tau_{skin}}} \tag{2.26}$$

where w_{Br} is the Brillouin frequency $w_{Br} = 4\pi n c_s/\lambda = 2\pi\cdot 45$ GHz and the acoustic time-of-flight $\tau_{skin} = \delta_{skin}/c_s = 1.68$ ps through the skin depth $\delta_{skin} = \lambda/(4\pi k) = 10.6$ nm for a given probe wave length $\lambda = 393$ nm (complex index of refraction is $\tilde{n} = n + i\cdot k = 1.45 + i\cdot 3$[55]).

The sensitivity function $G(t)$ determines the shape of the reflectivity signal when the ultrashort acoustic pulse arrives within the skin layer of the probe pulse. In the sensitivity function there are two contributions : sine-term that changes slowly and cosine-term that is responsible for a sharp step. It will be informative to illustrate different combinations of photo-elastic coefficients A and B. Depending on the dominant term the sensitivity function will distort differently the transient reflectivity responses as it is shown in Fig. 2.7, where four different cases of A and B are considered.

The resulting response of the material on the presence of acoustics is controlled by the ratio between B and A that can be expressed as follows

$$\frac{B}{A} = \frac{\beta-\chi}{\beta\chi+1}, \chi = \frac{dn}{d\eta}/\frac{dk}{d\eta}, \beta = \left(\frac{n}{k}\right)\frac{n^2+k^2-1}{n^2+k^2+1}. \tag{2.27}$$

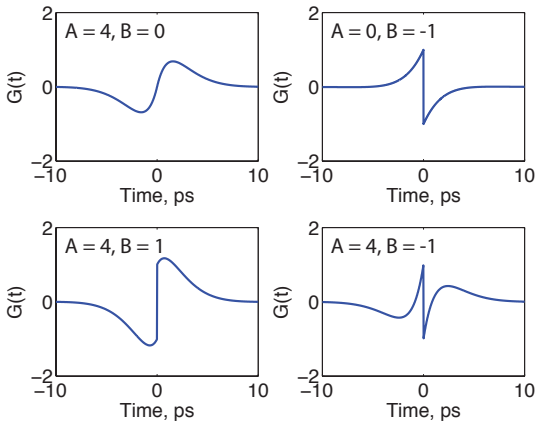

Figure 2.7: The response function $G(t)$ for different combinations of the photo-elastic coefficients A and B which reveal smooth response when B approach to zero and sharp step if A is very small.

The sensitivity function $G(t)$ given by Eq. (2.26) is appropriate for detection at the free interface of the sample because it takes into account total reflection of strain with change of sign, whereas that is not necessarily the case. If the probing surface is the interface between a transparent substrate and a metallic film the sensitivity function $G(t)$ will undergoes some changes.

For example, if we suppose the ideal interface between two mediums (phase matched situation) the sensitivity function will contain only one half of the sensitivity function suitable for the detection at the free interface as it is shown in Fig. 2.8. This can be the case for the detection at the cobalt/sapphire interface because the reflection coefficient is very small ($R \leq 10\%$).

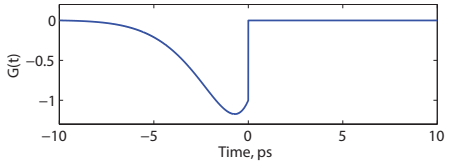

Figure 2.8: The response function for strain detection at the interface between phase-matched materials.

2.5 Reconstruction of ultrashort acoustic strain pulses

Usually, analysis of the acoustic data from pump-probe measurements is done by manual fitting of the strain pulse shape. Therefore, to fit experimental data several or even multiple assumptions about strain pulse shape are frequently made. That is why quantitative acoustic measurements require reliable algorithm for acoustic strain profile $\eta(t)$. It was shown recently that for acousto-plasmonic measurements it is possible to recover the strain profile using an iterative numerical method[25]. In this section I will describe in details recently proposed algorithm of reconstruction of the strain pulse shape from transient reflectivity measurements which is based on the Fourier transform. In addition this algorithm will be applied also to

acousto-plasmonic experimental data.

2.5.1 Reconstruction of strain from transient reflectivity data

First attempt on the way to build the reconstruction algorithm for transient reflectivity measurements was to apply iterative numerical method proposed by Temnov et al.[25]. In the case of acousto-plasmonic measurements the strain pulse shape can be recovered from the derivative of the real part of the dielectric function $\delta\epsilon(t)$:

$$\eta(t) = \frac{\tau_{\text{skin}} d\epsilon'}{2|\epsilon_{\text{m}}|dt} - \frac{1}{2\tau_{\text{skin}}} \int_{-\infty}^{\infty} \eta(t') e^{-\frac{-|t-t'|}{\tau_{\text{skin}}}} dt'. \tag{2.28}$$

This equation converges for experimental data that comprise of ultrashort acoustic pulses which are shorter than the acoustic propagation time through the optical skin depth τ_{skin}.

Similar expression to Eq. (2.28) can be derived for transient reflectivity from Eq. (2.25)

$$\begin{aligned} \eta(t) &= \frac{dS(t)}{dt}\frac{\lambda}{16\pi c_s} - \int_{-\infty}^{\infty} \left(A\omega_{Br} - \frac{B}{\tau_{skin}} \right) \cos(\omega_{Br} t' - t) e^{-|t'-t|/\tau_{skin}} \eta(t') dt' \\ &+ \int_{-\infty}^{\infty} \left(B\omega_{Br} + \frac{A}{\tau_{skin}} \right) \sin(\omega_{Br}|t'-t|) e^{-|t'-t|/\tau_{skin}} \eta(t') dt'. \end{aligned} \tag{2.29}$$

However, the numerical iterative solution of this equation diverges because of too large coefficients of the sine and cosine terms.

From the other hand we have tried to apply the Fourier transform to reconstruct the strain pulse shape from Eq. (2.25). In that case the strain $\eta(t)$ will be given by

$$\eta(t) = \frac{\lambda}{8\pi^2 c_s} \int_{-\infty}^{\infty} \frac{S(\omega)}{G(\omega)} e^{i\omega t} d\omega \tag{2.30}$$

where $S(\omega)$ is the Fourier transform of experimental data and $G(\omega)$ is the Fourier transform of Eq. (2.26). In more general case the expression of the sensitivity function $G(w)$ can be analytically represented as follows

$$G(\omega) = -2i\omega \frac{(2\omega_{Br}/\tau_{skin})A + (\omega^2 - \omega_{Br}^2 + 1/\tau_{skin}^2)B}{(\omega^2 - \omega_{Br}^2 + 1/\tau_{skin}^2)^2 + (2\omega_{Br}/\tau_{skin})^2} \tag{2.31}$$

Unfortunately, division by $G(w)$ in frequency domain in Eq. (2.30) can result in three singularities, $\omega = 0$ and $\omega = \pm\omega_0 = \sqrt{\omega_{Br}^2 - 1/\tau_{skin}^2 - 2(\omega_{Br}/\tau_{skin})(A/B)}$. However it is possible to minimize or even prevent from the influence of these singularities. First zero-frequency $\omega = 0$ can be avoided by subtraction of the slow thermal background in experimental signal $S(t)$ to guarantee $\int S(t)dt = 0$ which will ensure $S(\omega = 0) = 0$. The two other singularities occur when $\omega_{Br}^2 - 1/\tau_{skin}^2 > (A/B)(2\omega_{Br}/\tau_{skin})$, thus it is possible to select such pair of wavelength and metal to avoid non-zero roots in $G(\omega)$ or shift them to low frequency range.

Evaluation of the algorithm

Evaluation of the proposed algorithm have been made for the transient reflectivity data measured for the sample consisting of 100 nm of gold followed by thin 30 nm layer of cobalt on top of the sapphire substrate. In this experiment both pump and probe pulses were incident from the free surface of gold, where the pump pulse was 200 fs FWHM at 800 nm and the probe pulse of the same duration at 400 nm. Before implementation of the reconstruction algorithm the detected signal should be preprocessed to avoid the artifacts in the reconstructed strain. These steps consist of:

1. All pulses which are not related to acoustics should be removed (like electronic peak).
2. Thermal exponential background should be subtracted to ensure evanescence of first zero $\omega = 0$ by $\int S(t)dt = 0$, what will mean that only coherent part of acoustics will be treated by reconstruction algorithm.

The extracted part of the reflectivity signal is shown in Fig. 2.9 a) and b) by blue solid line. So far we are dealing only with the part of the signal containing the acoustic echo generated by hot electrons in the cobalt layer and arriving at the free surface of gold.

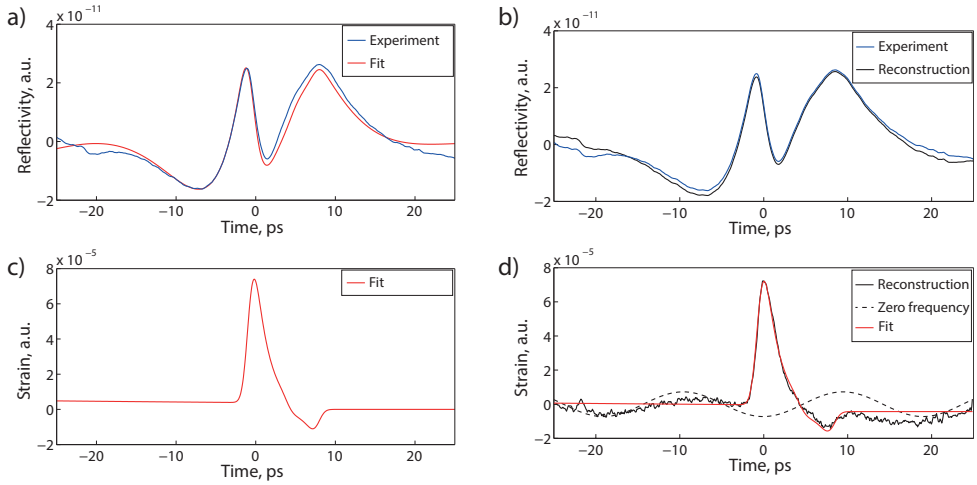

Figure 2.9: a) Fit (red solid line) and experimental transient reflectivity data (blue solid line) in the case of strain generation by hot electrons through 100 nm of gold on a 30 nm cobalt film; b) Superposition of experimental (blue solid line) and reconstructed (black solid line) reflectivity curves with the help of reconstruction algorithm; c) Gaussian-like strain pulse shape used for fitting with the 10% reflection tale produced by reflection at cobalt/sapphire interface; d) reconstructed strain pulse shape (black solid line) with the zero-frequency oscillating term (black dashed line) that has the period 18 ps superimposed with manually adjusted strain pulse (red solid line).

This data was initially analyzed by manual fitting. Therefore, the strain pulse shape was supposed to consist of one exponential term and a tail from the 10% reflection at the cobalt/sapphire interface. Additionally, we took into account the nanometer surface roughness of the gold and high acoustic dispersion that cause the spreading of initially exponential strain pulse profile. For that we convoluted the strain with a Gaussian with 1 ps FWHM. The best fit was obtained for $\tilde{n} = n + i \cdot k = 1.46 + i \cdot 1.94$[56](for 400 nm probe

wavelength) and the ratio $B/A = -0.59$. The FWHM of first strain is equal to $\tau_0 = 2$ ps. The heat diffusion profile can be found by multiplying the strain duration by cobalt speed of sound $\zeta_{heat} = \tau_0 \cdot c_s = 2$ ps $\cdot$ 6.3 nm/ps ≈ 12 nm. This fit is shown in Fig. 2.9 c) and the transient reflectivity response of this strain is shown as red solid line and it is superimposed with experimental data in Fig. 2.9 a).

The same experimental curve has been used to obtain the shape of the strain by application of the reconstruction algorithm; as a result the reconstructed strain (black solid line) was superimposed with the manual fit (red solid line) and they are shown in Fig. 2.9 d). As it was discussed earlier, we observe the harmonic modulation (black dashed line) with period $T = 2\pi/\omega_0 = 18$ ps but the shape of strain itself corresponds very well to that expected theoretically (blue solid line) and we can see clearly both the first big pulse followed with 10% of reflection. It should be noticed also that reconstructed strain contains no assumption about the shape or reflections from the cobalt/sapphire interface. Furthermore, the only fit parameter, which was used, is the ratio of the photoelastic coefficients B/A. In both cases the transient reflectivity response was calculated using the strain pulse shape and Eq. (2.25). We can state that for both strains the reproduced reflectivity was very close to the experimental observation.

One single example of the data treatment is not enough to prove that this algorithm works. That is why one more transient reflectivity data was processed from very similar experiment[6]. In that experiment, the strain generation was done by direct illumination of a thin layer of $SrRuO_3$ (SRO) by 300 fs laser pulse with central wavelength 786 nm. The probe pulse was detecting the strain pulse arrival by transient reflection from the free surface of gold at 393 nm. We can notice that the probe wavelength and the material of detection are the same, that is why obtained previously ratio of photoelastic coefficients $B/A = -0.59$ can be used. The only difference in slightly different complex index of refraction that was used $\tilde{n} = n + i \cdot k = 1.67 + i \cdot 1.94$[57], where real parts of n differ by 0.2.

The strain pulse is estimated to have rectangular shape with FWHM around 1.9 ps, but surface roughness and acoustic dispersion will lead to spreading of the strain pulse. That is why best manual fit of strain pulse is a Gaussian with FWHM = 2.54 ps depicted in Fig. 2.10 c). The simulated reflectivity is shown in Fig. 2.10 a) as red solid line and follows well the dynamics of the experimental curve with a small difference at $t >$5 ps.

The reconstruction algorithm provides strain pulse shape as shown in Fig. 2.10 d) as black solid line. The superimposed manual fit of the strain (red solid line) has very high correspondence with the reconstructed strain. Nonetheless, the harmonic modulation observed in the previous reconstruction procedure is also presented here and the period of modulation remains to be 18 ps, but in contrast it shows much smaller amplitude.

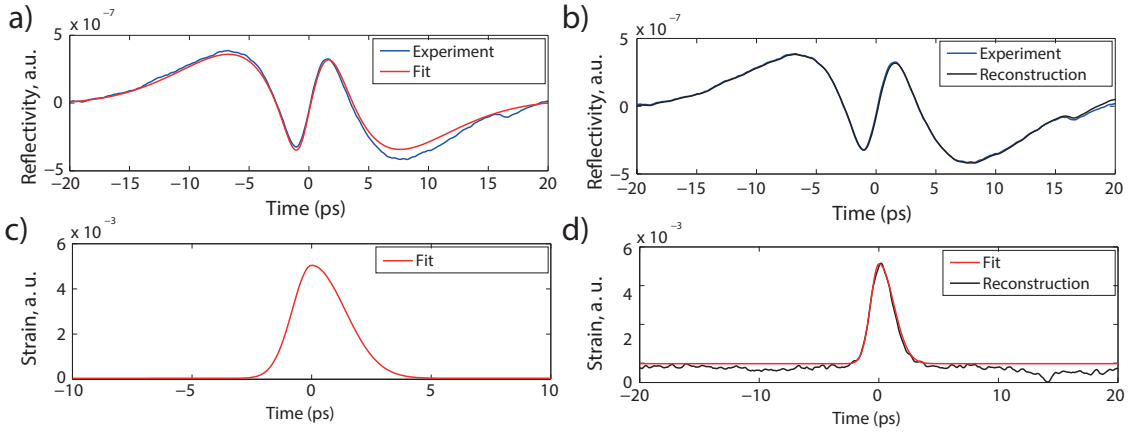

Figure 2.10: a) Superposition of experimental transient reflectivity data (blue solid line) and manual fit (red solid line) in the case of direct illumination of very thin 12 nm single crystal SRO layer; b) Superposition of experimental (blue solid line) and reconstructed reflectivity (black solid line) curves with the help of reconstruction algorithm are almost identical; c) Gaussian-like strain pulse shape obtained by manual fitting; d) reconstructed strain pulse shape (black solid line) with very low amplitude of zero-frequency oscillating term (with period 18 ps) superimposed with the manual fit (red solid line).

2.5.2 Reconstruction of strain from acousto-plasmonic data

It can be shown also that such approach can be used for reconstruction of acousto-plasmonic data presented in the section of evaluation of strain propagation. Even though a general method for acoustic strain pulse reconstruction from acousto-plasmonic experiment can be developed. For that we need to express the strain $\eta(t)$ from the analytic expression that determines the change of the dielectric permittivity $\delta\upsilon_{real}(t)$ and take the Fourier transform

$$\eta(\omega) = \frac{\tau_{skin}}{|\epsilon_m|}\frac{\Sigma(\omega)}{F(\omega)}, \tag{2.32}$$

where $\Sigma(\omega)$ is the Fourier transform of the measured real part of dielectric function $\delta\epsilon_{real}$ and $F(\omega)$ is the Fourier transform of the sensitivity function of gold under the presence of the strain within the skin layer and it is given by

$$F(\omega) = \sqrt{\frac{2}{\pi}}\frac{i\omega\tau_{skin}^2}{1+\tau_{skin}^2\omega^2}. \tag{2.33}$$

Fortunately, in the case of acousto-plasmonic sensitivity function there is only one zero frequency component that corresponds to $\omega = 0$ and it can be avoided by simple background removal. Finally, after taking the inverse Fourier transform it is possible to obtain the general form for the expression of the strain

$$\eta(t) = \sqrt{\frac{\pi}{2}}\frac{1}{|\epsilon_m|\tau_{skin}}\int_{-\infty}^{\infty}\Sigma(\omega)\frac{1+\tau_{skin}^2\omega^2}{i\omega}e^{i\omega t}d\omega. \tag{2.34}$$

Evaluation of the algorithm

The measured ultrafast dynamics of the real part of the surface dielectric function without slow thermal background is shown in Fig. 2.11 a), where three bipolar signals show arrival of the strain pulses within the skin layer of surface plasmons modulated by the sensitivity function $F(t)$. The result of recovery of the strain pulses from the experimental data is shown in Fig. 2.11 b), where we can clearly see three echoes: first which was generated by absorption of the laser pulse in the cobalt layer and two other by reflections at gold/-cobalt and cobalt/sapphire interfaces respectively. The processed signal does not contain any thermal background, there is no sign of periodic modulation in the reconstructed strain.

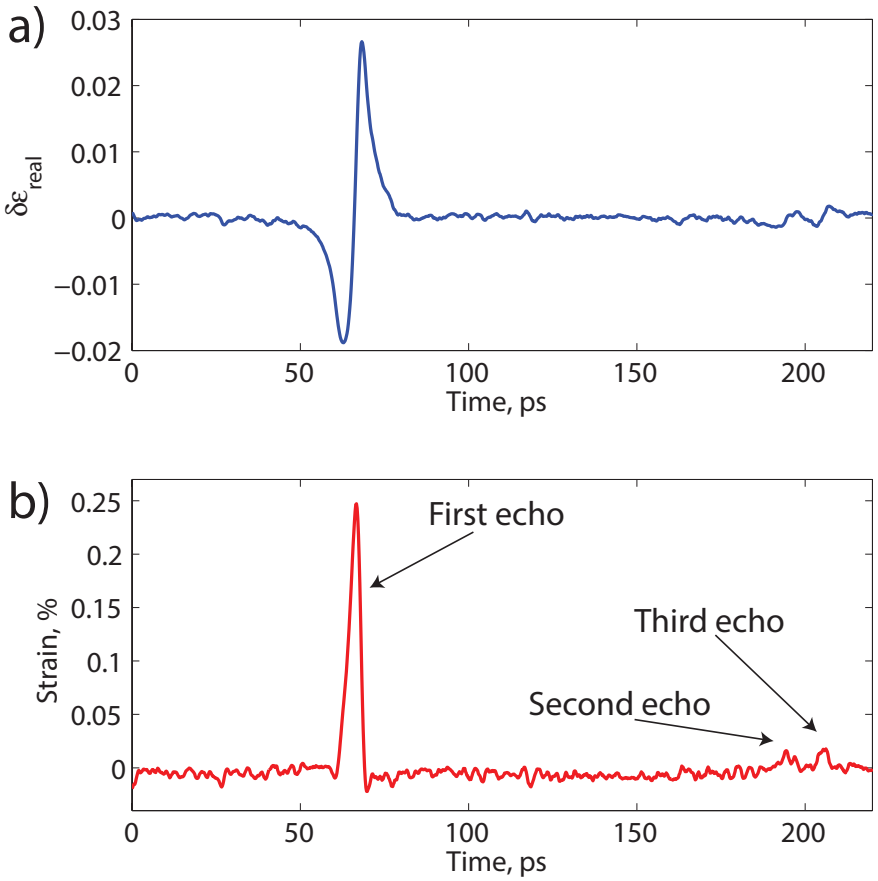

Figure 2.11: a) Dynamics of the real part of the surface dielectric function without thermal background; b) Strain pulse shape reconstructed using Eq. (2.34) shows three consecutive echoes detected at free surface of gold.

The shape of the first reconstructed echo is compared with the solution of the nonlinear Korteveg-de Vries equation[25] which takes into account the dispersion during strain propagation in the gold layer, and also the smearing effect of 1 nm surface roughness is considered. Superposition of the reconstructed (blue solid line) and calculated (red solid line) strains is shown in Fig. 2.12. We can notice good qualitative agreement resulting in 3 ps pulse shape that corresponds to 20 nm heat penetration depth.

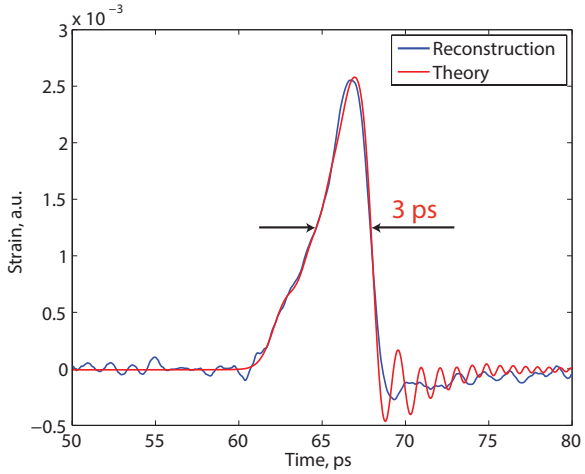

Figure 2.12: The first reconstructed acoustic echo (blue solid line) is superimposed with the solution of the Korteveg-de Vries nonlinear equation, additionally taking into account 1 nm surface roughness gold surface (red sold line).

2.5.3 Conclusion

The proposed algorithm is suitable for reconstruction of the arbitrary acoustic strain pulses measured by transient reflectivity and acousto-plasmonics. We have seen that reconstructed strain pulses are in good agreement with theoretical expectations for transient reflectivity and in good agreement with solution of Korteveg-de Vries nonlinear equation.

Additionally, the algorithm is easy to implement and preprocessing steps like hot electron peak removal and background subtraction are easy to implement. Furthermore, the majority of the constants needed for reconstruction are easy to find in the available databases. The only inconvenience is related to the necessity to know the photoelastic coefficients A and B for transient reflectivity measurements.

The only drawback of proposed algorithm is enclosed in fundamental limitations of the Fourier transform for zero-frequencies that results in harmonic modulation of processed data shown for transient reflectivity case. Additionally, it was shown that the zero-frequency ω_0 originates in the choice of the probe wavelength and depends on the material properties. Therefore, it is possible to choose a pair of probe wavelength and metal to decrease the influence of modulation. However, it was shown by analytical development, that in the case of acousto-plasmonic detection there is only one zero-frequency component $\omega_0 = 0$ that can be easily avoided by thermal background removal.

The proposed reconstruction algorithm did not use any assumptions of how the strain pulse should look like and can be used for recovery of an arbitrary acoustic strain profiles that can be very practical in the domain of ultrafast acoustics.

2.6 Experimental details of pump-probe techniques

Thanks to the progress in the field of ultrafast lasers made in the last decades, investigation of the dynamics of electrons and phonons at femtosecond timescales using femtosecond lasers is now possible. Intense and ultrashort laser pulses provide a unique possibility to excite wave packets of coherent phonons in the sub-THz range[6,58,59]. The branch of physics that uses femtosecond lasers for generation and detection of phonons is called "picosecond ultrasonics" and the main method for experimental investigations is the pump-probe technique firstly presented for a sub-picosecond acoustic generation by Thomsen et. al. in 1984[1].

In the following chapter all experimental issues connected to the generation and detection of picosecond acoustics through the measurement of the change of the reflectivity will be discussed. I will overview the equipments and their role in the pump-probe setup. Additionally, two modifications of initially presented configuration are explained. The first adaptation is used for performing time-resolved imaging with the help of a CCD camera of surface illuminated by the probe pulse. The second modification allows to detect magnetic signals in gold/cobalt/sapphire samples linked to the excitation of the "hot" electrons in gold. These hot electrons can easily penetrate in adjacent ferromagnetic cobalt layer and cause precession of magnetization.

2.6.1 Femtosecond two-side pump-probe setup

The setup for the two side pump-probe experiment that was used for our measurements is presented in Fig. 2.13. In this setup a 800 nm laser beam serves as the pump. Right at the laser output, the pump pulse is passed through a non-linear crystal for frequency doubling providing 400 nm probe pulse. Then pump and probe pulses are separated. Therefore the probe pulse is forwarded to the surface of detection. At the same time, the pump pulse goes through an acousto-optic modulator and a delay line to adjust the optical path between pump and probe. Then two objectives are used to focus both pulses into the same region from different sides. The reflected probe pulse from the surface contains the information about the perturbation generated by the pump pulse. That is why it is directed to a photodiode which is connected to a lock-in amplifier. In turn, the lock-in amplifier extracts the signal at the reference frequency of modulation of pump pulse (typically of KHz range) to increase signal-to-noise ratio. Finally, a homemade computer software control the XPS controller that change the delay between pump and probe pulses allowing to detect time evolution of the signal induced by the pump pulse.

Hereafter I will briefly present the role and characteristics of the elements of the setup.

Laser

The femtosecond laser is the core element of the pump-probe setup. In our case we used Coherent MIRA 900s. Gain medium of this laser is a titanium doped sapphire (Ti:Sapphire)

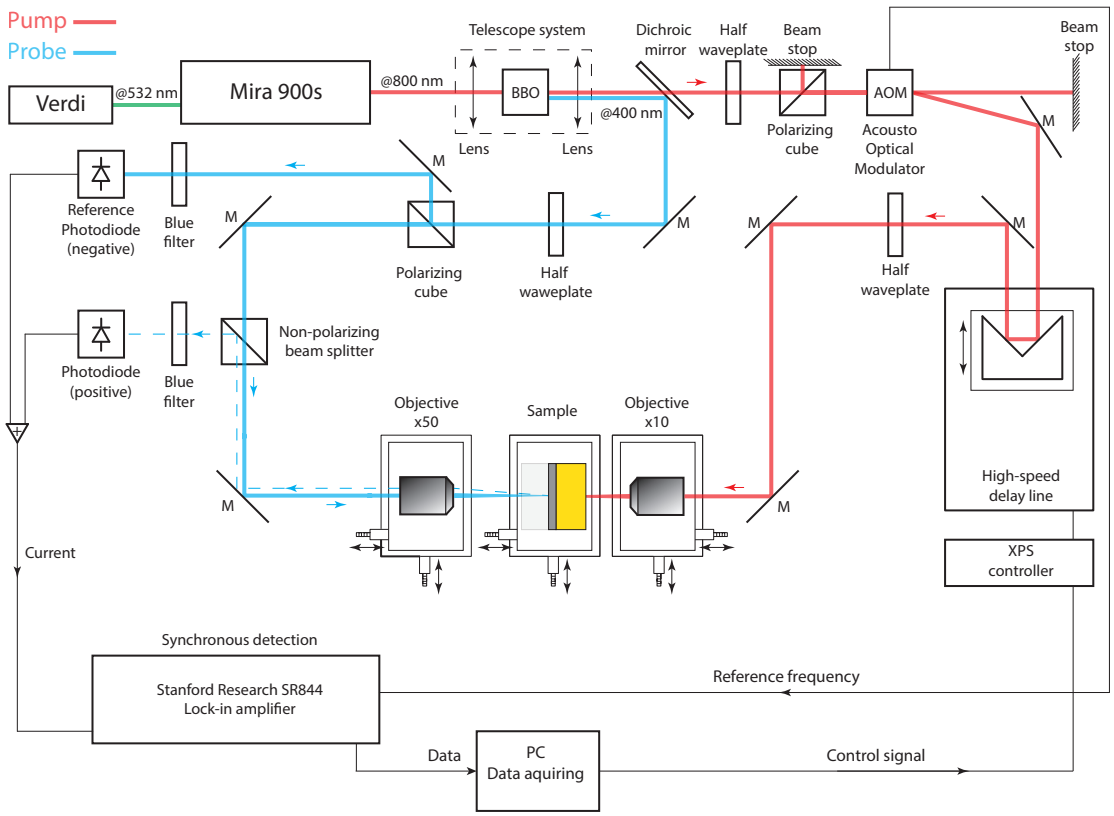

Figure 2.13: Pump-probe experimental setup with synchronous detection for pumping and probing from different sides.

crystal. The mode-locked oscillator is pumped with a continuous wave (c. w.) laser Verdi that delivers up to 5 W of power. The Mira laser output delivers infrared 150 fs pulses of 25 mW average power that corresponds to 40 nJ of energy in each pulse at 800 nm wavelength. The 500 kHz repetition rate of the laser is controlled by the cavity damper elements inserted inside the MIRA cavity.

Telescope

The telescope in this setup serves for two reasons :

1. To collimate the divergent light from the laser output (the dimension of the beam on the output is 2 mm diameter).

2. To generate 400 nm probe pulse with a Beta Barium Borate (BBO) crystal in the focal plane of the first lens.

The BBO is a nonlinear crystal that offers the possibility to generate second harmonic (with 20-30 % efficiency). Thus by doubling the frequency of Mira laser we obtain the probe pulse of 400 nm. This probe pulse is reflected then by the dichroic mirror (such mirror reflects the light in a specific spectrum depending on the deposited coating and transmits other wavelengths).

Half waveplate and polarizing cube

The combination of a half waveplate and a polarizing cube serves for tuning the laser intensity forwarded to the sample in order to conduct the experiment below the damaging threshold. By rotation of the half waveplate the polarization of the laser light is rotated and only the horizontal component of the electric field of light passes through the polarizing beam splitter and is directed to the sample.

Acousto-optic modulator (AOM)

In pump-probe techniques, the pump beam is often modulated in intensity at a given frequency so that, associated with a synchronous detection allows to increase the signal-to-noise ratio and detect very small signals.

We have used an acousto-optic modulator that uses acousto-optic effect to deflect the pump pulse at KHz reference frequency. Efficient deflection of the incoming laser light occurs at an angle of incidence of light equal to the Bragg angle θ_B. The angle between the first-order diffracted beam and zero-order diffracted beam is $2\theta_B$ (see Fig. 2.14). The diffraction condition is given by

$$\sin\theta_B = \frac{\lambda f}{2nc_s} \tag{2.35}$$

where λ is the wavelength of the light, f is the acoustic carrier frequency ($\sim$ 110 MHz), n and c_s are the refractive index and the sound speed of the AOM crystal respectively. This crystal is made of paratellurite TeO_2 with $c_s = 4200$ m·s^{-1}, $n = 2.2$ at 800 nm. The angle of deviation $2\theta_B$ for TeO_2 cell is equal to 0.5°. Considering the small deviation angle a distance of about 30 cm is necessary for the separation of two beams.

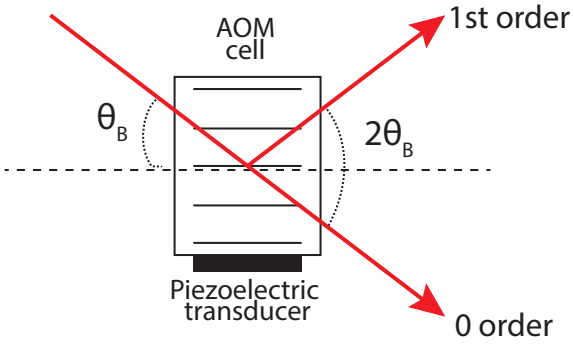

Figure 2.14: Diagram showing the principles of operation of an acousto-optic modulator. The angle of incidence is equal to the Bragg angle θ_B and the deflection angle is $2\theta_B$.

The first order deflected beam is then used as the pump pulse and is forwarded to the sample surface, whereas the reference frequency of the pump modulation from the AOM is sent to the lock-in amplifier for synchronization.

Synchronous detection

Synchronous detection is used in pump-probe experiments because the signal generated by the pump pulse is often very small $10^{-4} \div 10^{-7}$. Moreover such tiny signal is hidden in the noise that can be produced by the change of the ambient temperature, airflow on the path of the light, vibrations, laser fluctuation and so on.

For synchronous detection we used a Stanford Research SR844 lock-in amplifier. This lock-in use the synchronous demodulation to recover the signal at the reference frequency. To illustrate the principle of work we can consider two harmonic signals of constant amplitude with the same modulation frequency f_m, one is a voltage from the photodiode that measures the reflectivity change $U_{phot} = A\sin(2\pi f_m t)$ and another is a voltage from the AOM. Thus the signal from AOM contains the reference frequency of modulation of the pump pulse $U_{ref} = B\sin(2\pi f_m t)$. Then, inside the lock-in these two signals are multiplied

$$\begin{aligned} U_{phot} \cdot U_{ref} &= A\sin(2\pi f_m t) \cdot B\sin(2\pi f_m t) \\ &= \frac{1}{2}AB \cdot \cos(2\pi(f_m - f_m)t) - \frac{1}{2}\cos(2\pi(f_m + f_m)t) \\ &= \frac{1}{2}AB - \frac{1}{2}AB\cos(2\pi 2 f_m t) \end{aligned} \tag{2.36}$$

After multiplication there are two components : the constant (DC) $\frac{1}{2}AB$ and component at double frequency $2f_m$ with a negative sign (this indicates that the phase shift of $2f_m$ component is $-180°$). Then the lock-in performs the low-pass filtering that retains the DC component and neglects all high-frequency components containing $2f_m$ term and noise. Thus, if there are multiple harmonics in U_{phot} only those close to the reference frequency f_m will appear in the output of the lock-in (bandwidth of the filter can vary).

Delay line

For detection of temporal evolution of the induced changes in the sample we used a delay line. The delay line changes the optical path between pump and probe pulses by displacement of a retro-reflector mounted on a linear servomotor which ensures precise, fast and small stepping. We used a Newport ILS-LM high speed linear motor stage connected to a Newport XPS controller. This delay line is 60 cm length, however, since the laser beam travels back and forth, the Newport ILS-LM stage provides 120 cm of spatial delay (which corresponds up to 4 ns of time delay). The XPS controller in turn, was connected to a computer to control the motion.

Objectives

Because of relatively small output laser power, two objectives were used in the setup to increase the laser fluence at the focus. The first objective focuses the pump pulse in a small

region on the sample surface. Whereas, the second objective focuses the probe pulse from the other side of the sample to ensure the detection from a small region of disturbances produced by the pump pulse. We used two Mitutoyo objectives, first x10 for pump pulse and second x50 for probe pulse. These objectives have an advantage in comparison with conventional lenses, such as correction of chromatic and spherical aberrations. As disadvantage we can state higher (up to 20%) losses due to reflections in multiple optic elements inside the objective. Alignment of the beams is facilitated by the presence of precise moving stages with three degrees of freedom. The size of the pump beam on the sample after focusing through x10 objective is about 20 μm Full-Width at Half Maximum (FWHM). From the other side of the sample, the size of the probe beam using a x50 objective is around 5 μm FWHM.

Alignment of the pump-probe setup with high magnification objectives opposite to each other can be a difficult task. That is why, first of all it is necessary to reach overlapping of pump and probe pulses without objectives. Then we can mount one of the objectives and arrange it collinear to the optic axis, with taking care about passing the beam right through the center of the objective. Next step is to mount the second objective similarly. For final step of collimation, we used a pin-hole placed in the focus between the objectives. Such pin-hole with 5 or 10 μm diameter facilitates precise alignment and overlapping of pump and probe beams in the focal plane. As a result of correct final step of alignment both pulses should pass the pin-hole. Only after that this pin-hole can be replaced by the sample.

Additional points of the setup

During the day the laser fluctuations could be very important. That is why we used two balanced current photodiodes to remove laser fluctuations. First (reference) photodiode was illuminated by the probe pulse reflected from a non-polarized beam splitter and contains only noise produced by the laser. Its intensity was tuned by the half waveplate situated before the beam splitter. A second photodiode was used to collect the light from the probe pulse reflected from the sample surface. The photodiodes that were at our disposal generate current of different signs, such that in parallel we obtain the subtraction from both photodiodes as an input for the lock-in.

2.6.2 Femtosecond two-side pump-probe setup with 2D imaging

A growing interest for ultrafast studies of nanosized objects requires imaging at the nanoscale and at the femtosecond timescale. It was shown recently[60] that it is possible to build a setup for 2D imaging with femtosecond resolution. Briefly, in this setup, the photodiode was replaced by a CCD camera and the acquisition process was synchronized with the help of a LabVIEW program. This program controls both the delay line position and frequency of the AOM. Scheme of this setup is presented in Fig. 2.15.

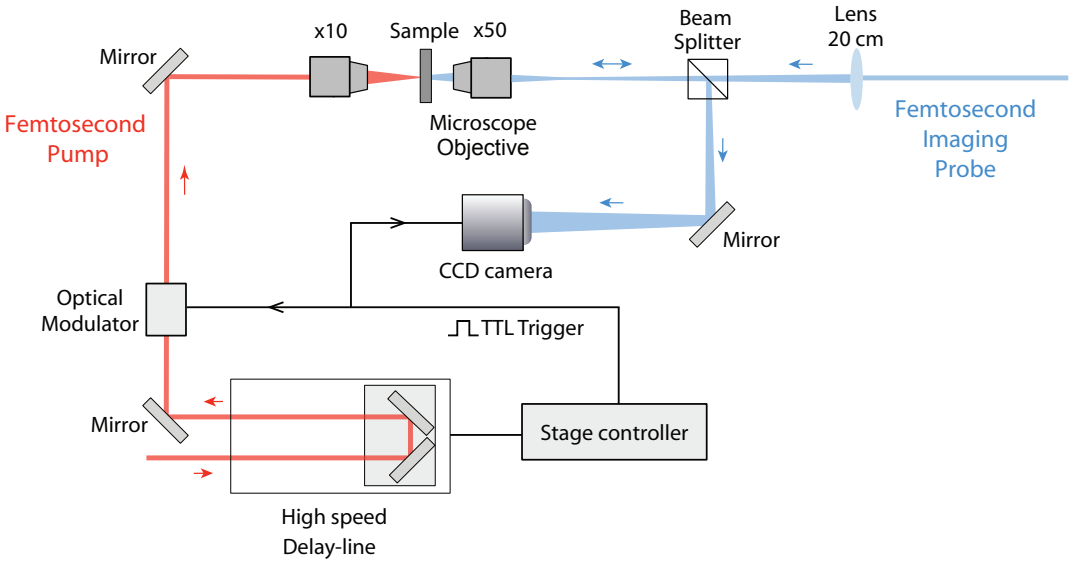

Figure 2.15: Scheme of the core of the femtosecond pump-probe imaging experimental setup. Two objectives are adjusted from different sides. First x10 objective focus femtosecond 800 nm pump pulse on the back of the sample for generation of transient process. Another x50 objective is adjusted from the front side for scanning by 400 nm femtosecod imaging probe. The lens positioned before the beam splitter is devoted to illuminate the entire surface of the CCD camera. Stage controller sends a TTL trigger instantaneously to optical modulator and to CCD camera. This is necessary to register one image without pump pulse (will serve as the reference) and another with the changes induced by the pump pulse. Then by subtraction of one image from another it is possible to eliminate laser noise like in the case of balanced photodiode scheme.

CCD camera

We used a Hamamatsu EM-CCD 9100-02 camera. It has high dynamic range (full well capacity of 70 000 electrons, 10 electrons of readout noise, 14 bit A/D converter) and maximum frame rate of 30 Hz at full image resolution of 1000x1000 pixels. Since we were interested in fast acquisition the resolution of the camera was reduced to 256x256. This manipulation allow to increase the frame rate up to 100 Hz and minimize the acquisition time. Essential point of this imaging setup is the synchronization between the stage controller, the acousto-optical modulator and the CCD camera. It is possible to represent the algorithm of interaction of these three elements as follows:

- When XPS stage controller increment the position of the delay line the TTL trigger is transmitted to the CCD camera and the AOM. The XPS controller send a TTL signal at a frequency less than the maximum frame rate of the camera $f \leq 100$ Hz.
- The optical modulator deflects the pump pulse only on rising (positive) edge of the TTL signal. In this way the modulation frequency of the pump pulse is only half $f/2$ of the operational frequency f of camera.
- Consequently, the CCD camera can image the surface of the sample with and without excitation. All the registered images are stored in RAM, thus for long scanning a big amount of memory is necessary.

Such manipulation allows eliminating the laser noise and therefore increases the signal-to-

noise ratio. Also, the final result can be improved by averaging many images from different loops of acquisition.

This setup allowed to measure a nonlinear reshaping of the strain propagating inside highly anisotropic gold medium and all the details related to that are presented in publication presented in Appendix C.

2.6.3 Nanosecond one-side pump-probe setup

Nanosecond measurements of the reflectivity changes were performed on the basis of the laser resonant ultrasound spectroscopy setup[61]. Simplified configuration relevant to our needs of thermal transport studies is presented in Fig. 2.16. In this setup we used a Q-switched microchip Nd:YAG laser that served as a pump laser. This laser operates at 1064 nm and delivers up to 10 μJ of energy with 0.6 ns pulse duration at 5 kHz repetition rate. We used a CW 532 nm laser at constant 1 mW power for probe pulse. The Gaussian probe spot of 50 μm diameter was focused on the surface of the sample. After reflection from the sample, the probe beam is forwarded to a New Focus 1601 high-speed photo-receiver with 1 GHz band-pass. According to the probe power a measurement sensitivity of 1 mV nm^{-1} was achieved with 0.5 mV$_{rms}$ noise level. The output of the photo-receiver was measured with a LeCroy WavePro 7300 3 GHz digital oscilloscope. The oscilloscope was triggered from the laser pulses at 5 kHz and the signal was measured during 2 seconds that corresponds to 10,000 averaged acquisitions after pump pulse arrival.

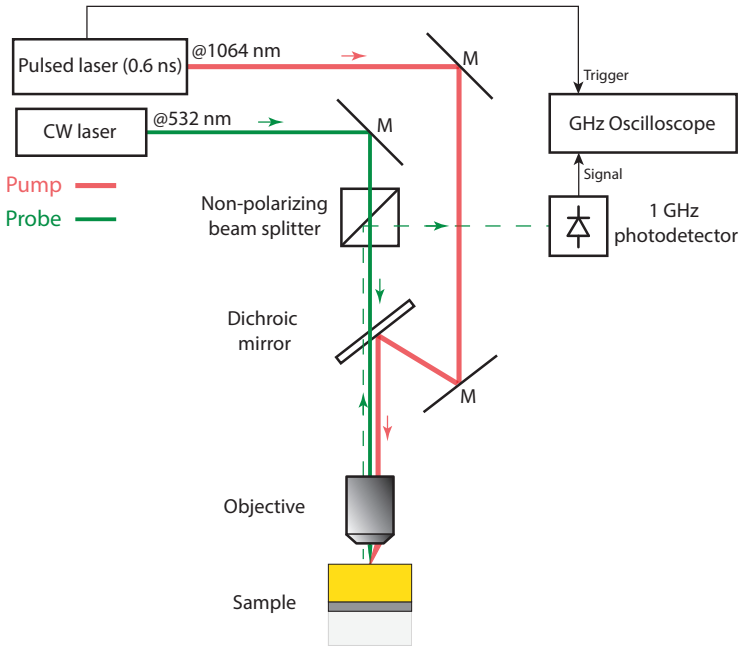

Figure 2.16: Nanosecond one side pump-probe experimental setup with synchronous detection.

2.6.4 Femtosecond two-side pump-probe setup for magnetic measurements

Different experimental approaches can be used for the measurement of the spin dynamics[62,63,64] and all of them are based on time resolved magneto-optic Kerr effect (MOKE). This effect allows to measure the polarization changes of the probe light reflected from a magnetized sample surface.

In thin ferromagnetic films, like 30 nm cobalt layer, the magnetization vector $\vec{M}$ is oriented in the plane of the sample, thus to be able to measure the Kerr effect in a polar geometry we need to change the direction of the magnetization. In the ideal polar Kerr geometry the magnetization vector $\vec{M}$ is perpendicular to the plane of the sample, therefore we should introduce a strong magnet that will reorient $\vec{M}$ to be out-of-plane.

We have used initially built pump-probe setup shown in Fig. 2.13 with few modifications at the detection stage, resulting in the setup shown in Fig. 2.17. The sample is magnetized by a strong neodymium magnet ($\approx$ 150 mT) inclined by $\approx 35°$ to reach out-of-plane magnetization.

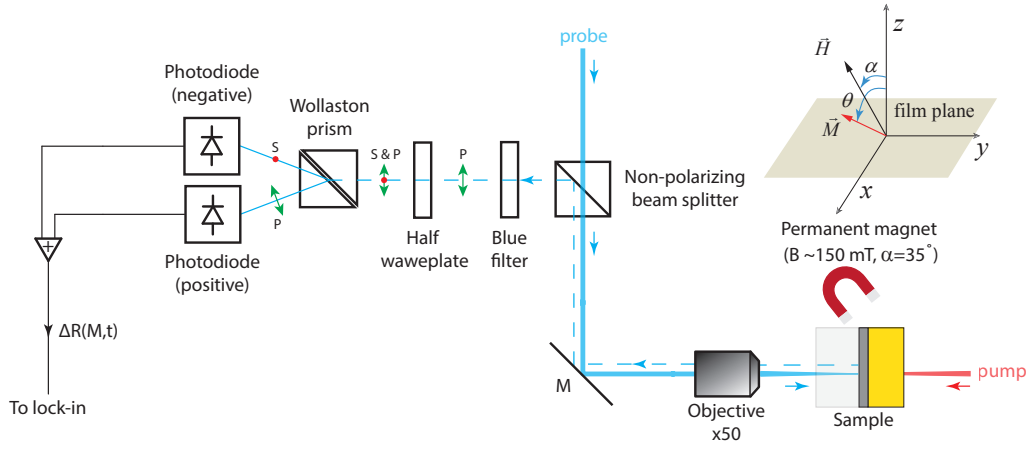

Figure 2.17: Modification of the pump-probe setup for MOKE measurement, introducing additional half waveplate and a Wollaston prism allowing the detection of the polarization rotation induced by precession of the magnetization $\vec{M}$. The sample is magnetized by a permanent magnet with field $B = 150$ mT tilted by 35°.

At the detection stage we introduce a half wave plate and a Wollaston prism before the balanced photodiode pair.The combination of the half waveplate and the Wollaston prism allows to measure the rotation of polarization MOKE at the surface of a ferromagnetic material. For that, initially linear polarization of the laser beam, in the absence of the pump pulse, should be rotated by the half waveplate and then splitted in the Wollaston prism into two beams detected by the photodiodes generating the current of opposite sign. This adjustment of the setup is shown schematically in Fig. 2.17, where a p-polarized (green double arrow) beam changes its polarization state by passing the half waveplate and presents an equal s (red dot) and p components before entering the Wollaston prism. Then, the Wollaston prism separates s and p polarizations which are detected by the balanced

photodiodes.

In this way s-polarized component of the light will be compensated by the p-polarized component resulting in the zero output. When an ultrashort laser pulse will be absorbed within the skin layer of the gold layer, the excited hot electrons will penetrate into adjacent cobalt film and after scattering on phonons the lattice temperature will increase. In the ferromagnetic layer the magnetic crystalline anisotropy changes, induced by the temperature gradient, will excite the ferromagnetic resonance (FMR)[65,10] that will change the polarization state of the reflected light. Therefore on the output of the Wollaston prism the intensity change of s and p components will be detected in the current forwarded to the lock-in.

2.6.5 Sample fabrication

Hybrid gold/cobalt/sapphire multilayer structures were manufactured in Germany (IFW Dresden) by DC magnetron sputtering (base pressure: $2x10^{-7}$ mbar; Ar sputter pressure: 10^{-3} mbar) of a (111) gold layer on top of a hcp-cobalt film deposited on a (0001) sapphire substrate. Once loaded into the deposition chamber, (0001) sapphire substrates were outgassed for 30 minutes at 250°C. Deposition of Co and Au layers was carried out also at 250° C. In the case of bilayer structure, a 30 nm thick Co layer was grown, then a (111)-textured gold layer with a thickness of 120-200 nm was deposited. Deposition rates were 12 nm/minute for Au and 2 nm/minute for Co. Nanometer surface roughness was characterized by atomic force microscopy for each investigated sample.

3

Data analysis

3.1 Analysis of thermal transport at the nano- and picosecond timescales

Basically, the rate of a heat diffusion or cooling of a heated sample depends on the following parameters: the specific heat capacity C_p, the thermal conductivity k, the thickness of the sample and finally the Kapitza resistance of an interface R_{Kap}. The first two parameters are constants and can be found in the literature. The thickness of the sample can be estimated by measuring the time between two consecutive acoustic echoes propagating at the sound speed inside the sample. As a result, only the Kapitza resistance is the unknown fit parameter that will help to analyze the heat diffusion for a set of measurements performed at nano- and picosecond timescales.

At this stage we will use a simplified model of the heat diffusion, such as the one temperature model, which has only averaged temperature of the carriers (no distinction on the electron or lattice temperatures). Energy injection by the laser pulse will be replaced by the initial temperature distribution formed after electron and phonon equilibration. As a result, the profile of the resulting temperature is characterized by the diffusion length ζ_{diff}. The diffusion length is a laser flux dependent parameter[28,31], but it can be estimated by analyzing the profile of the coherent acoustic generated by thermo-elastic mechanism[25]. Therefore, the FWHM of the generated acoustic pulse can be used as the diffusion length for the definition of the initial temperature distribution in the sample in our simulations of the heat diffusion problem.

3.1.1 One Temperature Model analysis in COMSOL

Before moving on to the details with analysis of the transient reflectivity data I will briefly introduce the proposed technique suitable for thermal transport studies performed at nanosecond and even picosecond timescales.

First of all at the initial stage of the analysis we are interested only in describing the incoherent carrier dynamics that has diffusive nature. This component of the signal can be characterized by slowly varying processes as compared to the coherent ultrafast acoustic signals. I will show that carrier dynamics that determine the heat flow in the sample can be reasonably well described by one temperature model with some assumptions about the initial temperature distribution generated by ultrafast diffusive electrons.

Therefore, for our purpose of the study of the thermal transfer in multilayer structures we used the heat diffusion model with one averaged temperature, that contains both the electronic and the phononic contributions

$$\rho C_p \frac{\partial T}{\partial t} + \rho C_p \cdot \nabla T + \nabla \cdot (-k \nabla T) = Q, \tag{3.1}$$

where C_p is the specific heat capacity, ρ is the material density, k is the thermal conductivity, and Q is the source term.

Solving the heat equation analytically for multilayer structures and for the complex initial temperature distributions can be a difficult task. However, a wide range of the numerical approaches that allow solving of complicated problems are at our disposal. We used the finite element software package COMSOL with the Heat transfer module. This software allows to accurately calculate the heat dynamics in very complex structures and to control nearly each step of the calculation.

The very crucial point in our simulations is a definition of the source term Q. Unfortunately, we can not simulate our problem from the very beginning, when the laser pulse excites free electrons, which afterwards transport the heat all over the structure. As it was mentioned before, the electrons excited in noble metals can travel on hundreds of nanometers[7,8,9,5]. Therefore in the case of a gold/cobalt sample with a gold thickness of even several hundreds nanometers there will be some amount of electrons transmitted to the adjacent cobalt layer. As a result, these electrons will heat the cobalt lattice leading to the complex temperature distribution because of the overheating factor related to a stronger cobalt electron-phonon coupling coefficient g^{Co} (see section 1.1).

How do we know about that? We observed experimentally the acoustic strain generation in the cobalt layer for each gold/cobalt sample pumped from the gold side. Even though we observed the generation of the strain in cobalt layer for the sample consisting of 500 nm gold and 30 nm cobalt as it can be seen in Fig. 3.1, where strains are highlighted by a dashed rectangles and pointed by the arrows.

We can determine the diffusion lengths ζ_{diff} for both gold and cobalt layers basing on the

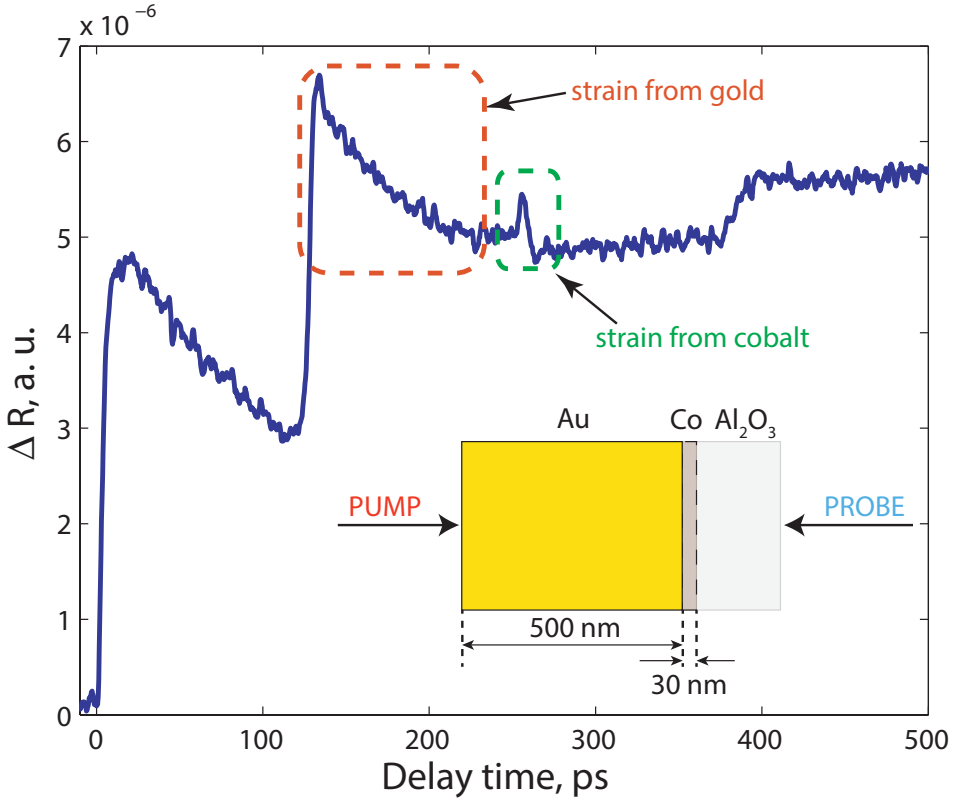

Figure 3.1: Demonstration of the strain generation in cobalt layer through 500 nm of gold

knowledge, that the acoustic strain pulse shape is dictated by the profile of the deposited heat[25] (through the thermo-elastic mechanism). These profiles were established after equilibration among electron and phonon bath, that typically takes less than 10 ps (for low fluences in the gold)[23]. As a result we have the following diffusion lengths

- $\zeta_{diff}^{Au} = 180$ nm for gold,
- $\zeta_{diff}^{Co} = 12$ nm for cobalt when pumping by electrons,
- $\zeta_{diff}^{Co} = 18$ nm for cobalt when pumping by 800 nm femtosecond laser pulses.

Therefore, the initial temperature distribution inside the gold/cobalt structure for an arbitrary overheating factor is presented in Fig. 3.2.

It should be mentioned that in our simulations we have only two fit parameters : the overheating of the cobalt layer and the Kapitza resistance. The overheating value determines the maximum amplitude of the temperature rise on the measured cobalt/sapphire interface, whereas the Kapitza resistance is responsible for the heat flow through the interface.

In our simulation we are able to extract the Kapitza resistances of both gold/cobalt and cobalt/sapphire interfaces, but for that we need to analyze reflectivity signals from two different timescales because of their different sensitivity to the heat flow dynamics. At the picosecond timescale the non-homogeneous distribution of the temperature as shown in Fig. 3.2 should first equilibrate within the metallic films. Therefore the main heat flow will be across the gold/cobalt interface, thus the Kapitza resistance of this interface will tune the

rate at which the cobalt layer is cooling mainly into the gold layer.

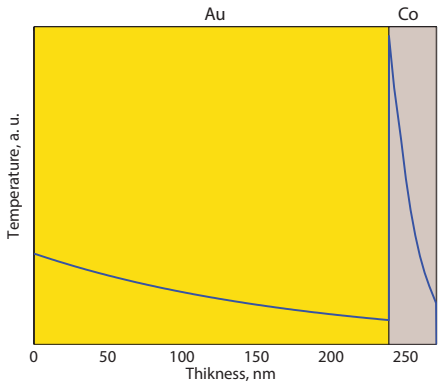

Figure 3.2: Example of an initial distribution of the temperature in gold/cobalt structure based on the heat diffusion parameters $\zeta_{diff}^{(Au),(Co)}$ which were extracted from the acoustic pulses.

To evaluate this assumption we conducted the simulation of the heat diffusion for the sample consisting of 240 nm of gold followed by 30 nm of cobalt on the 500 μm sapphire substrate. The initial distribution of the temperature consists of two exponential functions with corresponding diffusion lengths $\zeta_{diff}^{(Au),(Co)}$ for each material and the overheating of the cobalt layer is equal to 13 as it is shown in Fig. 3.3 as green solid line. Physical parameters used in the simulation are listed in the Table 3.1 and for this particular case no Kapitza resistances were defined.

Table 3.1: Physical parameters of gold, cobalt and sapphire for COMSOL simulations

Property\Material	Gold	Cobalt	Sapphire	Unit
Density	19300[66]	8900[66]	3980[67]	$[\rho] = [\text{kg m}^{-3}]$
Specific heat capacity	129.1[68]	421[68]	761[67]	$[\text{C}_p] = [\text{J kg}^{-1}\ \text{K}^{-1}]$
Thermal conductivity	318[69]	69[70,71]	25.2[67]	$[\text{k}] = [\ \text{J m}^{-3}\text{K}^{-3}]$

Since the profile of the temperature at $t = 0$ ps (green solid line) shows big difference at the gold/cobalt interface, the heat flux across this boundary will lead to the rapid cooling of the overheated cobalt layer into the gold film. Progressive profiles of the temperature with the time step $\Delta t = 5$ ps show the continuous temperature equilibration and the last profile demonstrates that equilibration of the temperature in gold and cobalt layers takes only 50 ps. After this point only the Kapitza resistance of the cobalt/sapphire interface becomes a limiting factor that determines the rate of the heat transfer.

This simulation shows that at picosecond timescale within first 50 ps under the condition of non-homogeneous initial distribution the interface between gold and cobalt is of crucial importance. That is why the influence of even small value of the Kapitza resistance will be pronounced.

However, we might experience the limitation of the time window for analysis of the slowly cooling pairs of materials because the classical femtosecond pump-probe setup with the delay

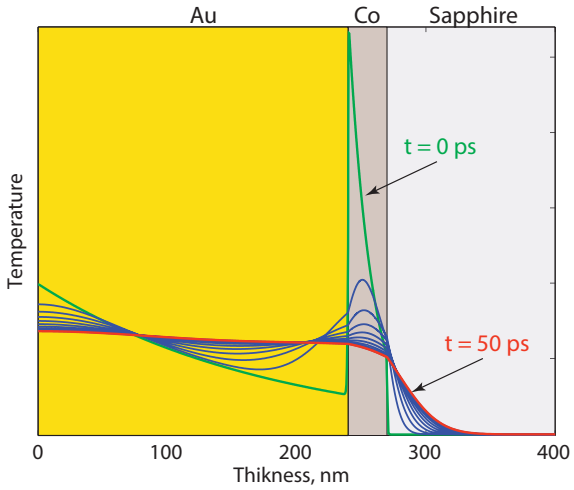

Figure 3.3: Spatial profiles of the temperature in a gold/cobalt/sapphire structure after solving the heat equation with the initial distribution shown as the green solid line. The profiles start from the $t = 0$ ps with 5 ps time step. Fast cooling of the cobalt layer is followed by the heating of the adjacent gold film. The last profile corresponds to time $t = 50$ ps (red solid line) which shows quasi-uniform distribution of the temperature inside the gold/cobalt layers.

line of 60 cm length can provide no more than 4 ns time delay. Such short scan might not guarantee an explicit fitting.

To confirm that, we conducted a similar simulation but within 50 ns time window that is shown in Fig. 3.4, where the time steps were equal to $\Delta t = 5$ ns. Since the equilibration of the complex initial temperature profile in gold and cobalt takes only 50 ps, all the profiles except the first one shows the uniform distribution of the temperature in metals. It can be seen that the amount of heat conducted to the sapphire substrate through the cobalt/sapphire interface is much larger at the nanosecond timescale, which means that only the Kapitza resistance of this interface is dominating.

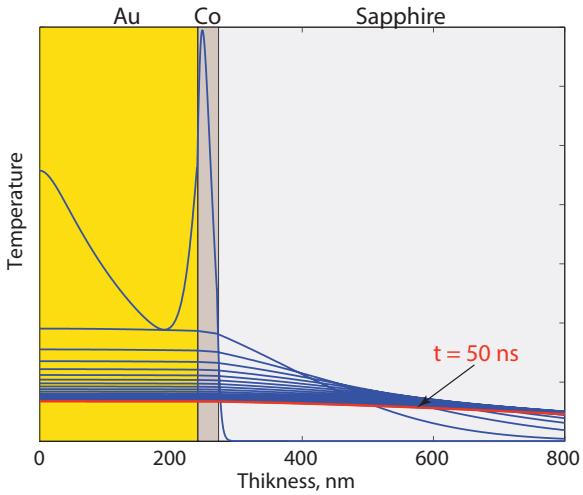

Figure 3.4: Spatial profiles of the temperature inside the gold/cobalt/sapphire sample after solving the heat equation with a time step equal to $\Delta t = 5$ ns. Equilibration of the temperature inside the structure takes only 50 ns (red solid line). At nanosecond timescale the influence of the Kapitza resistance of the gold/cobalt interface will be minimal and by contrast the Kapitza resistance of the cobalt/sapphire interface will be dominant.

To conclude, we have seen that the dominant impact of the heat flow through the gold/-cobalt interface can be observed at the picosecond timescale and the cobalt/sapphire interface plays a major role at the nanosecond timescale. Based on these observations we can suppose that it is possible to determine the Kapitza resistances for each interface even in complex bimetallic structures by performing both femtosecond and nanosecond pump-probe experiments. It should be mentioned also that the cooling rate is more sensitive to the heat diffusion profile determined by ζ_{diff} in the case of picosecond dynamics. However, it has almost no importance for nanosecond timescale, thus for fitting of nanosecond reflectivity data the approximation with the uniform initial profiles of the temperature in both layers can be applied.

Analysis of the reflectivity data will be divided into 3 parts. In first two parts we will analyze single gold and cobalt films by simulation of the thermal background of nanosecond and picosecond reflectivity measurements with a single fit parameter : the Kapitza resistance of the metal-dielectric interface. Then we will move to more sophisticated analysis of the gold/cobalt samples.

The characteristics of the nanosecond pump-probe setup used for measurements are mentioned in the section 2.6.3. This setup allows to pump and probe from the same side and all samples were measured from the free interface side.

The characteristics of the picosecond pump-probe setup are given in section 2.6.1. This setup allows to pump and probe from opposite sides of the sample and to measure with a femtosecond resolution the transient reflectivity signals. Analysis of the heat dynamics at a shorter timescale allow to estimate more accurately the values of the Kapitza resistance.

3.1.2 Analysis of the heat dynamics in gold/sapphire sample

The first sample that we will analyze is a single layer of 90 nm thick polycrystalline gold deposited on a sapphire substrate as shown in Fig. 3.5.

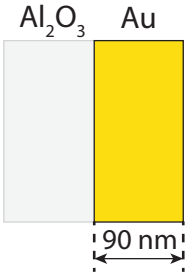

Figure 3.5: Single layer of 90 nm thick polycrystalline gold deposited on a sapphire substrate.

Nanosecond reflectivity

Nanosecond transient reflectivity curve measured for a single gold layer is shown in Fig. 3.6 as blue solid line. The cooling rate is very fast and can be characterized by 4.5 ns FWHM.

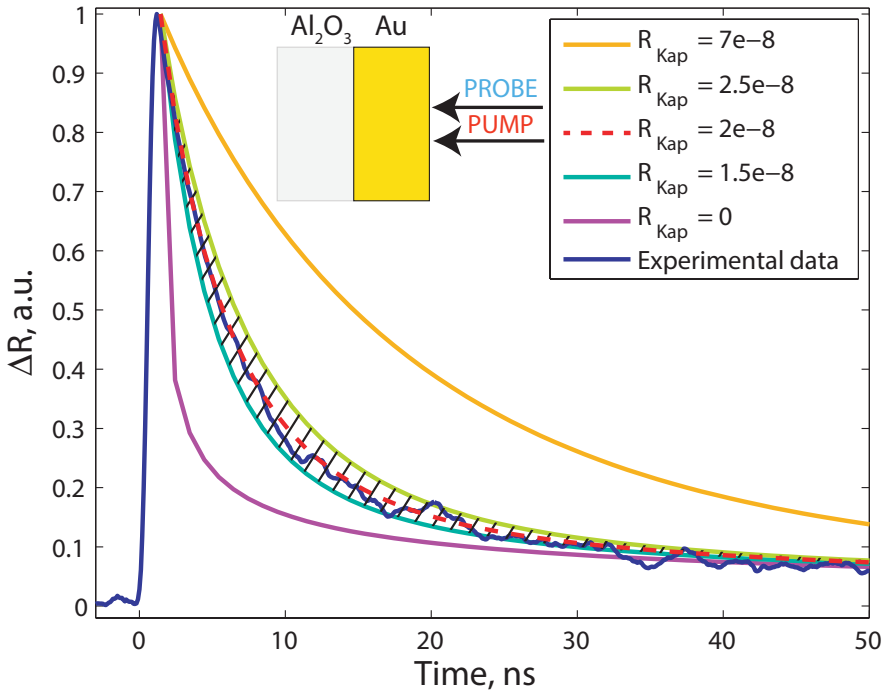

Figure 3.6: Reflectivity curve (blue solid line) measured for the gold/sapphire sample is fitted with solution of the heat diffusion equation for different values of the Kapitza resistance R_{Kap}. Best fit (red dashed line) was achieved for $R_{Kap} = 2 \cdot 10^{-8}$m^{2}KW^{-1} with an error $\pm 0.5 \cdot 10^{-8}$ m^{2}KW^{-1}.

All other curves are produced by COMSOL simulation in attempts to fit the cooling. As it was discussed before, the initial distribution of the temperature can be considered exponential with $\zeta_{diff}^{Au} = 180$ nm but even uniform distribution will produce the same result because the thickness of the sample is small. We can notice a significant difference in the cooling dynamics for a set of simulated Kapitza resistances $0 \div 7 \cdot 10^{-8}$ m^{2}K/W. Among all Kapitza resistances the best correspondence with the experimental data was achieved for $R_{Kap} = 2 \cdot 10^{-8}$ m^{2}KW^{-1} (red dashed line) with an error $\pm 0.5 \cdot 10^{-8}$ m^{2}KW^{-1} shown by a dashed region that comprise all the values of the Kapitza resistances from $R_{Kap} = 1.5 \cdot 10^{-8}$ m^{2}KW^{-1} to $R_{Kap} = 2.5 \cdot 10^{-8}$ m^{2}KW^{-1}. Estimated value of the Kapitza resistance is in good accordance with the value obtained by Stoner and Maris $R_{Kap}^{Au/Sapphire} = 2.2 \cdot 10^{-8}$Km^2/W[38,34]. For comparison, the Kapitza resistance of the gold/SiO_2 interface was found to be $1.8 \pm 0.2 \cdot 10^{-8}$ m^{2}KW^{-1} [72].

Picosecond reflectivity

Picosecond transient reflectivity curve measured for the same gold layer is shown in Fig. 3.7 as blue solid line. In the very beginning we can admit the presence of a very big "electronic peak" (amplitude of this peak reaches -11 a. u.). The electronic peak indicates almost instantaneous arrival of the electrons generated by the pump pulse within the skin depth. From the thermal point of view we can analyze a rise time of the thermal background that follows the arrival of the electronic peak. Therefore, its rise time is equal to ≈ 10 ps, which

indicates that equilibration of the temperature inside the gold film is extremely fast due to the efficient diffusion of the electrons that heat the lattice along their diffusive trajectories.

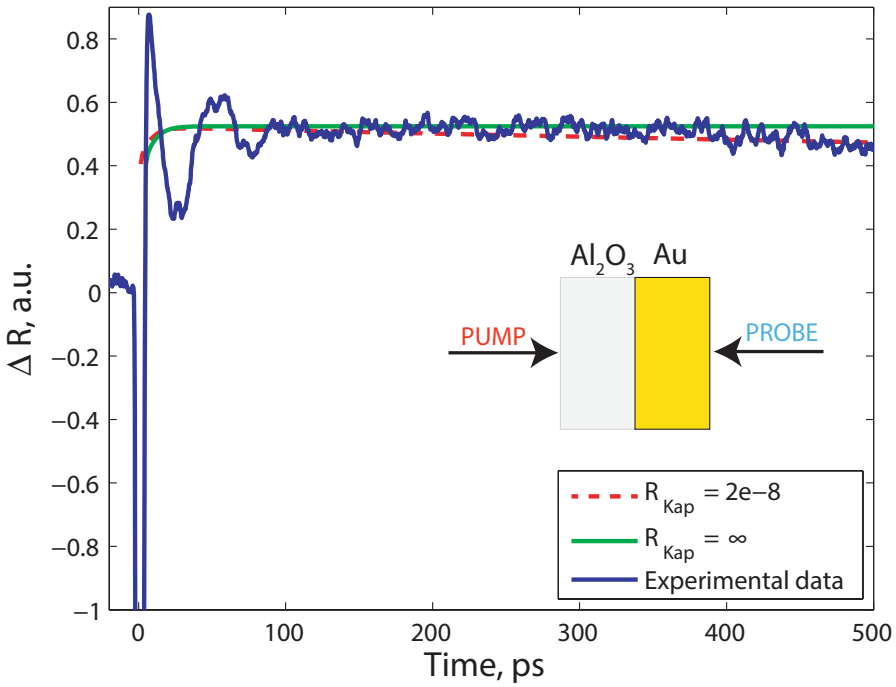

Figure 3.7: Reflectivity curve (blue solid line) of the gold/sapphire sample is fitted with solution of heat diffusion equation (red dashed line) that corresponds to the Kapitza resistance $R_{Kap} = 2 \cdot 10^{-8}$ m^{2}KW^{-1}. Additionally, the solution of the simulation considering infinite Kapitza resistance is shown as the green solid line as a reference.

This signal contains also a coherent acoustic strain propagating inside the structure (two oscillations within 100 ps corresponding to two acoustic echoes detected at the gold/sapphire interface). But keeping in mind the determination of Kapitza resistance, we are interesting only in incoherent thermal component that is a slowly decaying background.

We performed a simulation for the infinite Kapitza resistance of the gold/sapphire interface that blocks the heat inside the film. The heat dynamics corresponding to this case is illustrated in Fig. 3.7 by green solid line. By contrast, the heat dynamics for the Kapitza resistance estimated previously at nanosecond timescale with $R_{Kap} = 2 \cdot 10^{-8}$ m^{2}KW^{-1} (red dashed line) shows very small difference with the dynamics of the infinite Kapitza resistance. Therefore, analysis of samples possessing a large value of the Kapitza resistance are not accurate enough at the picosecond timescale. That is why for such samples we rely on values obtained from nanosecond measurements.

3.1.3 Analysis of the heat dynamics in cobalt/sapphire sample

The second sample that we will analyze is a single layer of 90 nm thick polycrystalline cobalt deposited on a sapphire substrate as shown in Fig. 3.8.

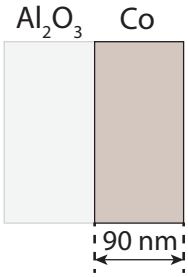

Figure 3.8: Single layer of 90 nm thick polycrystalline cobalt deposited on sapphire substrate.

Picosecond reflectivity

A single cobalt film was investigated under the same experimental conditions as the previous gold film. Picosecond transient reflectivity curve measured at the free cobalt surface is shown in Fig. 3.9 as blue solid line. Two oscillations presented within 100 ps are two acoustic echoes generated close to the cobalt/sapphire interface. We can notice that temporal duration of this echoes is much shorter than in the case of the single gold film. Such short acoustics is directly proportional to the heat penetration depth which was estimated to be $\zeta_{diff}^{Co} = 18$ nm, in agreement with previously reported results[25].

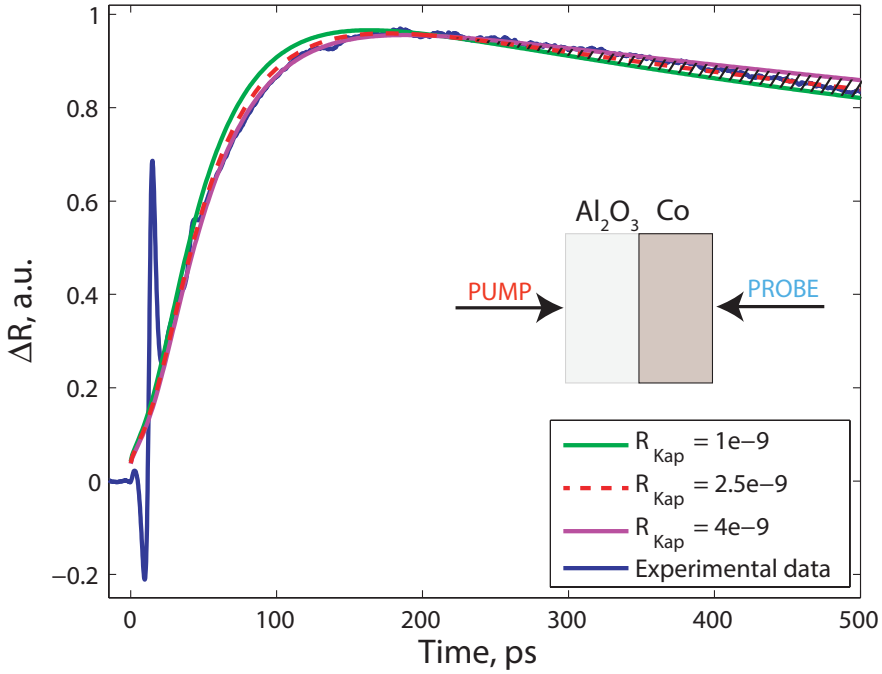

Figure 3.9: Reflectivity curve (blue solid line) of the cobalt/sapphire sample is fitted with the solution of the heat diffusion equation (red dashed line) that corresponds to the Kapitza resistance $R_{Kap} = 2.5{\cdot}10^{-9}$ m^{2}KW^{-1} with an error $\pm 1.5 \cdot 10^{-9}$ m^{2}KW^{-1}.

In contrast to the reflectivity measured for the gold sample, there is no measurable electronic peak corroborating the fact of inefficient electron diffusion in cobalt [12,3]. It means that all the excited electrons are involved in the strong generation of the coherent acoustic strain within the diffusion length. As a result the rise time of the thermal background is very slow and it takes $\approx$ 170 ps to achieve a spatially homogeneous temperature distribution inside the cobalt film.

The best correspondence of simulation with the experimental data was achieved for $R_{Kap} = 2.5 \cdot 10^{-9}$ m^{2}KW^{-1} (red dashed line) with an error $\pm 1.5 \cdot 10^{-9}$ m^{2}KW^{-1} shown by a dashed region that comprises all the values of the Kapitza resistances from $R_{Kap} = 1 \cdot 10^{-9}$ m^{2}KW^{-1} to $R_{Kap} = 4 \cdot 10^{-9}$ m^{2}KW^{-1}.

3.1.4 Analysis of the heat dynamics in gold/cobalt/sapphire sample

The third sample that we will analyze consists of 150 nm gold layer followed by 30 nm cobalt layer grown on sapphire substrate as shown in Fig. 3.10.

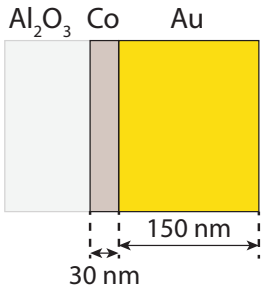

Figure 3.10: Thin 30 nm cobalt layer is sandwiched between 150 nm gold layer and sapphire substrate.

Nanosecond reflectivity

Analysis of the gold/cobalt sample will help to understand the heat transport through the gold/cobalt interface and the influence of a thin 30 nm cobalt layer in the overall cooling dynamics of two metallic films. The transient reflectivity curve measured at the gold free interface is shown in Fig. 3.11 by blue solid line. We can notice a rapid 4 ns FWHM cooling of the gold surface. In this case the cooling rate is 0.5 ns faster than in the case of single 90 nm gold film. This result is very surprising because the overall heat capacity of the gold/cobalt layer is three times greater than the heat capacity of the single gold film (heat capacity $\approx C_p \cdot d_{layer}$).

As previously, the initial temperature distributions in gold and cobalt layers are considered to be uniform ($T_{Co} = T_{Au}$), that is why the analysis of this simulation can be simplified by neglecting the Kapitza resistance of the cobalt/gold interface. So far, the only fit parameter is the Kapitza resistance of the cobalt/sapphire interface and we expect it to be close to the

value measured for single cobalt layer equal to $R_{Kap} = 2.5 \cdot 10^{-9}$ m^{2}KW^{-1}. In the case of faster cooling the accuracy of the fitting is better, thus the estimated Kapitza resistance of the cobalt/sapphire interface reproduces very accurately the heat dynamics in bilayer sample as it is shown in Fig. 3.11 by red dashed line. Green solid line shows the cooling without any Kapitza resistances.

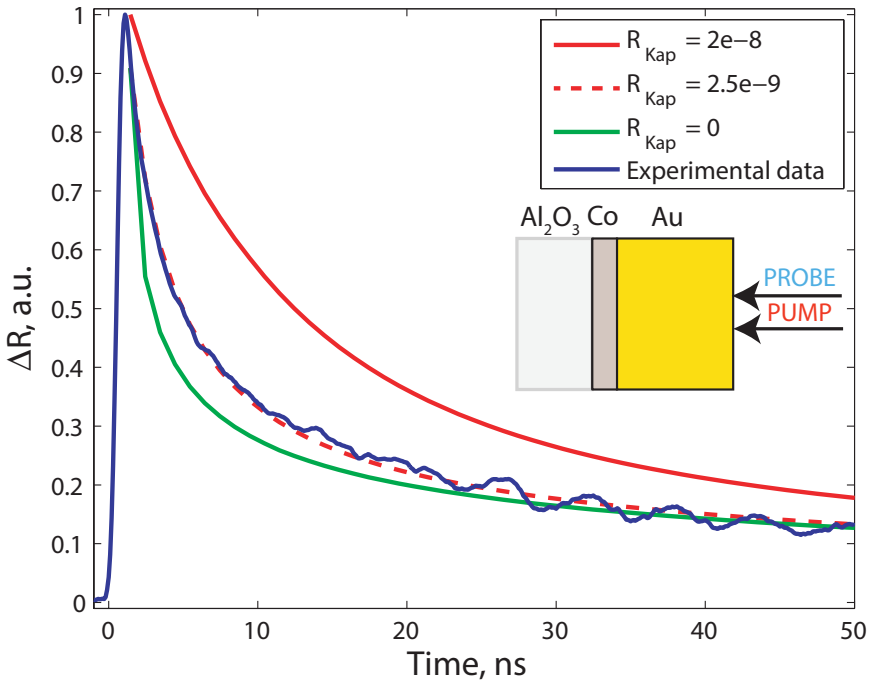

Figure 3.11: Reflectivity curve (blue solid line) of the gold/cobalt/sapphire sample is fitted with solution of the heat diffusion equation. The value of the Kapitza resistance estimated for the gold/sapphire sample (red solid line) is not suitable for simulation of the bilayer structure. Best fit (red dashed line) following well the dynamics of the cooling and corresponds to the Kapitza resistance estimated for 90 nm cobalt film equal to $R_{Kap} = 5 \cdot 10^{-9}$ m^{2}KW^{-1} . The sensitivity of this fit is bigger than in the case of single cobalt film because the zero Kapitza resistance curve (green solid line) shows much more difference with the best fit (red dashed line).

In Fig. 3.11 there is also one interesting curve simulated for the case when the cobalt layer is replaced by the gold (red solid line). In this case it is clear that the Kapitza resistance should be of the same value like in the case of 90 nm gold film equal to $R_{Kap} = 2 \cdot 10^{-8}$m^{2}KW^{-1}. We can notice that the cooling dynamics is three times slower than in the case of the gold/cobalt sample. Therefore we can conclude that the cobalt layer allows to obtain faster cooling and serves as a matching layer gold and sapphire.

This can be explained by the fact that electron transport between two metals is very efficient[16], thus excited electrons from the gold can easily cross the cobalt/gold interface where they scatter very rapidly on phonons[12,3]. Then, at the interface between cobalt and sapphire these phonons can be transmitted much easily into the substrate because this is the only possible mechanism of the heat transfer between a dielectric and a metal. As a result the cobalt layer can be treated as a buffer layer that transforms very efficiently energy from the electrons arriving from the gold layer into the phonons.

To confirm the buffer layer assumption, we can replace the cobalt layer by gold as it is shown in Fig. 3.12 and set a new (effective) Kapitza resistance of the new gold/sapphire interface to be $R_{Kap}^{eff} = 5 \cdot 10^{-9}$ m^{2}KW^{-1}.

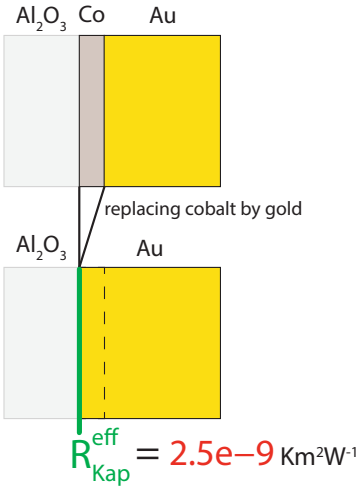

Figure 3.12: Scheme of the cobalt layer replacement by the buffer layer

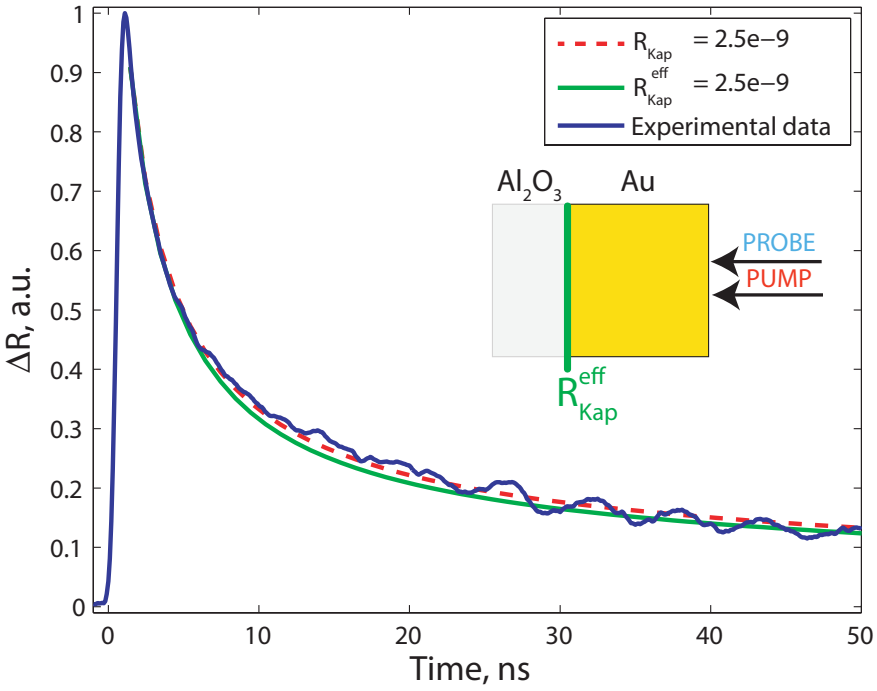

Figure 3.13: Application of the concept of the effective Kapitza resistance that replaces a thin cobalt layer. Simulation of the cooling dynamics with the effective Kapitza resistance (green solid line) allows to correctly reproduce the transient reflectivity curve at nanosecond timescale. A small offset with respect to the best fit simulated previously (red dashed line) can be noticed.

Simulation for the effective Kapitza resistance assumption in Fig. 3.13 (green solid line) is compared with the best fit obtained previously (red dashed line). We can notice that the difference in the dynamics of both curves is small and both of them describe well the

cooling of the structure. Therefore, if a thickness of the buffer layer is sufficiently small we can confirm the applicability of the concept of the buffer layer at the nanosecond timescale with the effective Kapitza resistance R_{Kap}^{eff} with the dielectric substrate. The dependence of the effective Kapitza resistance on cobalt thickness is a subject of future investigations.

Picosecond reflectivity

The last sample that we will analyze consists of 240 nm gold layer followed by 30 nm cobalt layer grown on sapphire substrate as shown in Fig. 3.14.

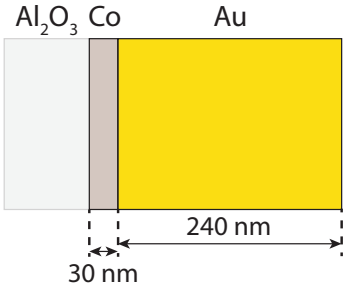

Figure 3.14: Thin 30 nm cobalt layer is sandwiched between 240 nm gold layer and sapphire substrate.

This sample was pumped from the gold side to generate the diffusive electron that will carry the energy to the cobalt layer through the gold/cobalt interface. The transient reflectivity signal was measured at the cobalt/sapphire interface and it is shown in Fig. 3.15 by blue solid line.

The shape of the reflectivity curve can be characterized by 16 ps rise time, i.e. the time of the temperature equilibration within the cobalt film. Relatively fast rise of the temperature is followed by the cooling into the sapphire substrate. The shape of the thermal background signal indicates that there is a strong overheating of the cobalt layer. To illustrate this, two simulations with the different initial temperature distributions are considered. In this particular analysis the values of the Kapitza resistances are less important and will be discussed afterwards, however both curves were obtained for the same Kapitza resistances. The first case is based on the assumption that there is no overheating at all. The profile of this temperature distribution inside gold/cobalt/sapphire structure is shown in inset in Fig. 3.15 by green solid line. As a result of this initial temperature distribution the heat dynamics at the cobalt/sapphire interface is shown by green solid line in Fig. 3.15. We can notice a remarkable difference in the dynamics of simulated and experimental curves. In simulated curve the homogenization of the temperature does not result into the strong amplitude rise, but instead demonstrates slow increase of cobalt temperature at cobalt/sapphire interface.

In contrast, the second temperature profile, shown in inset in Fig. 3.15 by red dashed line assumes overheating of the cobalt layer by a factor of 14.5. The heat flow through the cobalt/sapphire interface in this case displays the temperature very similar to the experimental observation. That happens because the overheated cobalt layer redistributes the

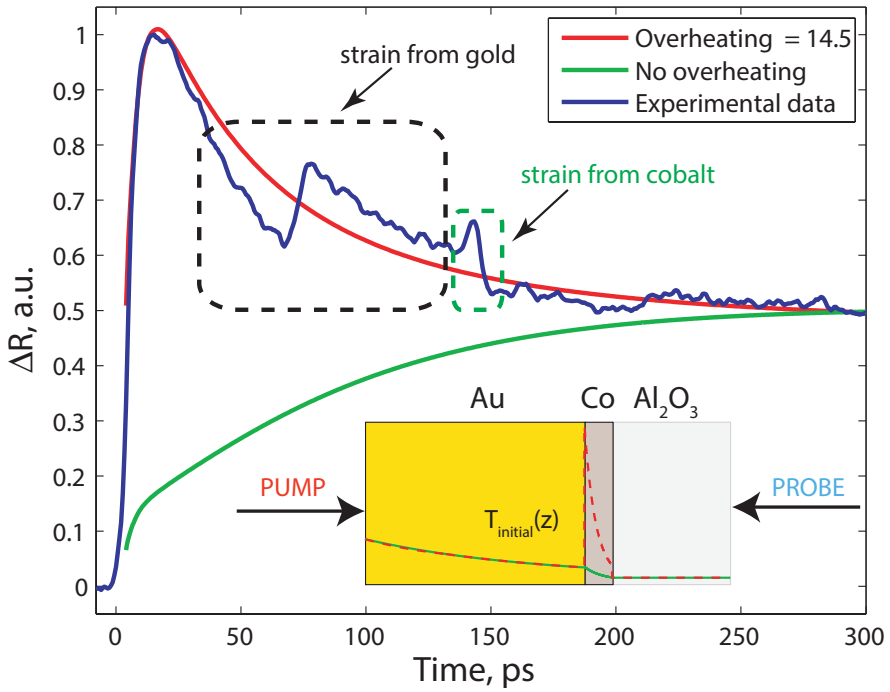

Figure 3.15: Dynamics of the transient reflectivity detected at the cobalt/sapphire interface (blue solid line), that shows a rapid growth of the temperature at the cobalt/sapphire interface until $t = 15$ ps and then followed by slow cooling. Two coherent acoustic signals from gold and cobalt layers are presented at times $t = 73$ ps and $t = 146$ ps respectively. Red dashed line shows the simulation where the cobalt layer is overheated by a factor of 14.5, whereas green solid line considers no overheating. Small inset demonstrates spatial profiles of the temperature for two simulated heat dynamics at the cobalt/sapphire interface.

energy within the entire film and only after that the energy is transferred to the substrate.

The temperature distribution that assumes a remarkable and almost "instantaneous" overheating of the cobalt layer indicates that the mechanism of the energy injection in the cobalt is the fast electron diffusion in gold allowing injection of the electrons into the cobalt film, where they scatter on the phonons and induce a fast growth of the lattice temperature.

An additional fingerprint of the ultrafast energy injection into the cobalt layer by hot electrons is the shape of coherent acoustic pulses. We observe a bipolar acoustic pulse generated in gold layer followed by the short unipolar acoustic pulse generated in the cobalt layer (black and green dashed rectangles in Fig. 3.15 respectively). The acoustic pulse from cobalt layer arrives at time 146 ps. It can be shown that this time corresponds to the round trip inside the gold film and single trip inside the cobalt film : (240 nm $\div$ 3.45 nm/ps)$\cdot$ 2 +30 nm $\div$6 nm/ps = 144 ps)). The estimated value is very close to the actual time of arrival.

The simulation was performed with two exponential temperature profiles: the gold profile has the diffusion length $\zeta_{heat}^{Au} = 180$ nm and the cobalt profile has $\zeta_{heat}^{Co} = 12$ nm. The Kapitza resistance of the cobalt/sapphire interface is $R_{Kap}^{Co/Sapphire} = 2.5 \cdot 10^{-9}$ m^{2}KW^{-1}. So far we have only two fit parameters :

1. the factor of overheating of the cobalt layer,

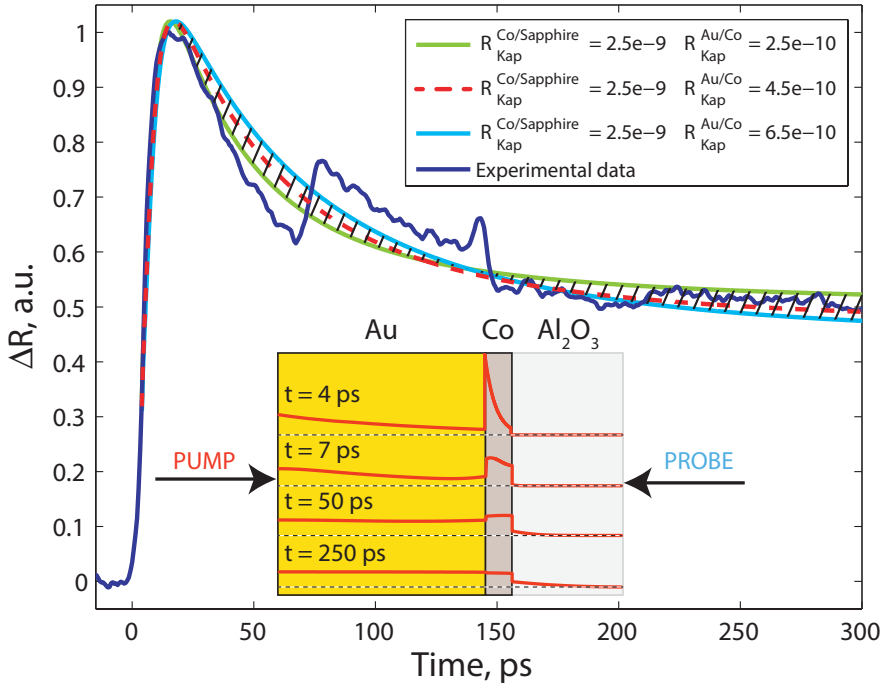

Figure 3.16: Transient reflectivity signal (blue solid line) and the best fit (red dashed line) that was performed with the following fit parameters : $R_{Kap}^{Au/Co} = 4.5 \cdot 10^{-9}$ m^{2}KW^{-1}, $R_{Kap}^{Co/Sapphire} = 2.5 \cdot 10^{-9}$ m^{2}KW^{-1}, and the factor of overheating of the cobalt layer equal to 14.5. Small inset shows the evolution of temperature profiles inside gold/cobalt/sapphire structure for a given instances of a time t.

2. the Kapitza resistance for the cobalt/gold interface $R_{Kap}^{Au/Co}$.

The simulation that allows to achieve the best agreement of the thermal dynamics with the temperature background that was observed experimentally corresponds to the factor of overheating of the cobalt layer equal 14.5 and the Kapitza resistance of the cobalt/gold interface equal to $R_{Kap}^{Au/Co} = 4.5 \cdot 10^{-10}$ m^{2}KW^{-1} (red dashed line in Fig. 3.16). The error of this estimation is $\pm 2 \cdot 10^{-10}$ m^{2}KW^{-1} and shown by a dashed region that comprises all the values of the Kapitza resistances from $R_{Kap} = 2.5 \cdot 10^{-10}$ m^{2}KW^{-1} to $R_{Kap} = 6.5 \cdot 10^{-10}$ m^{2}KW^{-1}. The initial temperature distribution and its dynamics inside the structure is shown in inset in Fig. 3.16, where the first profile corresponds to time $t = 4$ ps. We can notice that at time $t = 7$ ps the equilibrium temperature inside the cobalt film is still not reached and at time $t = 50$ ps both metallic films possess almost uniform temperature distribution.

The estimated value of the Kapitza resistance is typical for a metal-metal interface, for example the Kapitza resistance of an aluminium/copper interface is given by $R_{Kap}^{Al/Cu} = 2.5 \cdot 10^{-10}$Km^2/W[16].

To conclude, the shape of the fit of thermal background can be considered as correct, because the dynamics within the first 15 ps reproduce very well the temperature increase at the cobalt/sapphire interface and fitted curve passes through the middle point of the experimental curve at the time around $t = 60$ ps. This middle point corresponds to the arrival of the symmetrical bipolar strain generated at the free surface of gold.

3.1.5 Conclusion

In this section we have seen the analysis of the carrier transport measured by the transient reflectivity at nanosecond and picosecond timescales. Starting from the analysis of the single-layered gold and cobalt films deposited on the sapphire substrate we have seen that the cooling rate of the metallic films is directly related to the Kapitza resistance of the metal/sapphire interface. We used the initial distribution of the temperature inside the films from the profiles of the acoustics generated at picosecond timescale, thus the heat diffusion profile of gold is $\zeta_{diff}^{Au} = 180$ nm and the heat diffusion profile of cobalt formed by the direct laser absorption is $\zeta_{diff}^{Co} = 18$ nm. This assumption allowed us to have only the Kapitza resistance fit parameter in the COMSOL simulations. From nanosecond timescale cooling rate we determined that the biggest Kapitza resistance is attributed to the gold/sapphire interface that is equal to $R_{Kap}^{Au/Sapphire} = 2 \pm 0.5 \cdot 10^{-8}\mathrm{Km}^2/\mathrm{W}$ which is in high agreement with the value obtained by Stoner and Maris $R_{Kap}^{Au/Sapphire} = 2.2 \cdot 10^{-8}\mathrm{Km}^2/\mathrm{W}$[38,34]. Much smaller value of the Kapitza resistance was estimated using fitting at picosecond timescale for the cobalt/sapphire interface that is equal to $R_{Kap}^{Co/Sapphire} = 0.25 \pm 0.15 \cdot 10^{-8}\mathrm{Km}^2/\mathrm{W}$. We can notice that the fitting at picosecond timescale is more sensitive to the smaller Kapitza resistances like that of cobalt/sapphire interface.

After that we moved to the analysis of the complex heat dynamics observed for the gold/-cobalt/sapphire sample. We noticed, that by introduction of thin 30 nm cobalt layer between gold and cobalt the cooling of the structure was 3 times faster as compared to the gold film of the same thickness. We attribute this to the strong electron-phonon coupling of the cobalt layer that allows to heat the cobalt lattice more efficient. As a result, the phonon transport allowed for the metal/dielectric interface is more efficient in the case of the cobalt/sapphire interface.

Fitting of the gold/cobalt/sapphire sample involved two fit parameters : the Kapitza resistance of the gold/cobalt interface and the overheating factor of the cobalt layer, whereas the Kapitza resistance of the cobalt/sapphire interface was fixed to $R_{Kap}^{Co/Sapphire} = 0.25 \cdot 10^{-8}\mathrm{Km}^2/\mathrm{W}$. In the COMSOL simulation we also changed the heat diffusion profile of cobalt layer to $\zeta_{diff}^{Co} = 12$ nm because of the smaller penetration rate of the diffusive electrons. The best agreement with the experimental thermal background was achieved for the Kapitza resistance of the gold/cobalt interface $R_{Kap}^{Au/Co} = 0.045 \pm 0.02 \cdot 10^{-8}\mathrm{Km}^2/\mathrm{W}$ and with 14.5 cobalt layer overheating factor. The estimated value of the Kapitza resistance of the gold/cobalt interface is in good agreement with other Kapitza resistances of the metal-metal interfaces, for example, the Kapitza resistance of the aluminium/copper interface[16], that was measured to be $R_{Kap}^{Al/Cu} = 2.5 \cdot 10^{-10}\mathrm{Km}^2/\mathrm{W}$.

These studies can be very helpful in the domain of electronics and compact devices that require fast and efficient heat transport at the nano-scale.

3.2 TTM simulations for gold/cobalt structure

In the case of an excitation of the gold/cobalt sample by an ultrashort femtosecond laser pulse from the gold side we have seen two confirmations of the efficient electron diffusion and energy transfer to the cobalt layer. The first confirmation is the coherent acoustic strain generated in the cobalt layer which is shown in Fig. 3.1 and in Fig. 3.15. The second confirmation is the complex shape of the thermal background that demonstrates the presence of two source terms, one from the gold layer and another from the overheated cobalt layer. Fast timescales of these transients signify that hot electrons generated within the skin depth in gold penetrate efficiently in the cobalt layer.

In order to be able to study this diffusion quantitatively we will use the TTM presented in Section 1.1. First of all we will consider the ideal interface between gold and cobalt that neglects any kind of electron scattering and corresponds to zero Kapitza resistance. Then we will use the modifications presented in Section 1.3 to take into account electronic Kapitza resistance at the gold/cobalt interface.

The algorithm and a MATLAB code for the calculation of electron and phonon temperatures inside the bimetallic structure is given in appendix A.1.

3.2.1 TTM simulation with an ideal gold/cobalt interface

We performed the simulation of the TTM for the structure consisting of 150 nm gold layer followed by 30 nm cobalt layer. We consider that 200 fs (FWHM) laser pulse is normally incident at the gold surface as it is shown in Fig. 3.17. This simulation will help to analyze the evolution of the electron and lattice temperatures mainly in the cobalt layer.

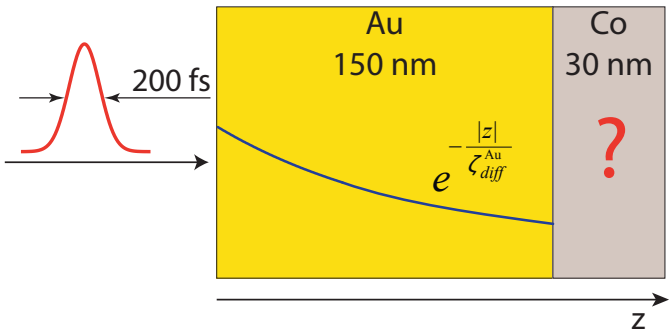

Figure 3.17: Scheme of the TTM simulation consisting of 150 nm thick gold layer and thin 30 nm cobalt layer excited by a 200 fs FWHM laser pulse of an arbitrary intensity.

The physical constants that in our simulations are listed in Table 3.2. The value of cobalt electron phonon coupling g^{Co} was estimated on the basis of the consideration that acoustic strain profile is determined by the heat diffusion ($e^{-z/\zeta_{diff}}$). We have seen in Section 1.1 that the diffusion parameter ζ_{diff} can be expressed by $\zeta_{diff} = \sqrt{k/g}$. From the other hand the duration of the acoustic pulse τ_{ac} multiplied by the sound speed of the medium of propagation

Table 3.2: Physical properties of gold, cobalt and sapphire for TTM simulations

Property/Material	Gold	Cobalt	Unit
Electron-phonon coupling	$2.3 \cdot 10^{16}$ [11]	$43 \cdot 10^{16}$	$[g] = [\frac{W}{m^3 K}]$
Heat conductivity	317 [69]	69 [70,71]	$[k] = [\frac{W}{mK}]$
Electron heat capacity	$71 \cdot T$ [73]	$677 \cdot T$ [74]	$[C_e] = [\frac{J}{m^3 K^2}]$
Lattice heat capacity	$2.5 \cdot 10^6$ [75]	$3.5 \cdot 10^6$ [10]	$[C_i] = [\frac{J}{m^3 K}]$

c_s should give ζ_{diff}. It was measured experimentally that $\tau_{ac}^{Co} = 2$ ps, therefore taking into account the sound speed in cobalt $c_s^{Co} = 6.3$ nm/ps we can estimate the electron-phonon coupling as follows

$$\zeta_{diff}^2 = k/g \equiv \left(c_s^{Co} \cdot \tau_{ac}\right)^2 \rightarrow g^{Co} = \frac{k^{Co}}{\left(c_s^{Co} \cdot \tau_{ac}\right)^2} = 43 \cdot 10^{16} \frac{W}{m^3 K}. \tag{3.2}$$

The estimated value of the electron-phonon coupling $g = 43 \cdot 10^{16}$ $\mathrm{Wm^{-3}K^{-1}}$ does not differ noticeably from that given by Bigot et al. [10] $g = 60 \cdot 10^{16}$ $\mathrm{Wm^{-3}K^{-1}}$.

Typically, heat conductivity, electron heat capacity and electron-phonon coupling are temperature dependent functions. For an electron-gas temperature below the Fermi temperature (which is of the order of $10^4 \div 10^5$ K) the heat conductivity and the electron heat capacity depend linearly on the electron temperature T_e : $k(T_e) = k_0 \cdot (T_e/T_i)$ [28,31] and $C_e = \gamma T_e$ [16] respectively. However, the electron-phonon coupling g does not vary significantly for low T_e [24,32,15].

We do not take into account the temperature dependence of all our parameters and assume small laser fluences (≤ 1 $\mathrm{Jm^{-2}}$ i. e. the pulse energy $\leq$0.3 nJ for the spot size of 20 μm FWHM).

Simulation of the TTM with the listed above parameters results in a two-dimensional (2D) plots of the electron temperature $T_e(z,t)$ and the lattice temperature $T_i(z,t)$. Interpretation of the results will be divided into two parts. First, I will show a 2D plot of the temperature with a spatial profiles inside the gold/cobalt layers and then a temporal profiles of temperature at the gold/air and gold/cobalt interfaces will be examined.

Spatial temperature profiles are important for the analysis of the electron diffusion. Temperature dynamics at two interfaces will show how fast the system reaches the equilibrium ($T_e = T_i$). Given a possible temperature jump at a metal-metal interface we will analyze two profiles at both sides of gold/cobalt interface.

Electron temperature

We will start with analysis of the electron temperature T_e, that is shown in Fig. 3.18 a). We can notice an extremely fast absorption of 200 fs laser pulse that is followed by rapid and deep diffusion of electrons towards the cobalt layer.

Excited electrons will arrive at the gold/cobalt interface by the time ≈107 fs (according to

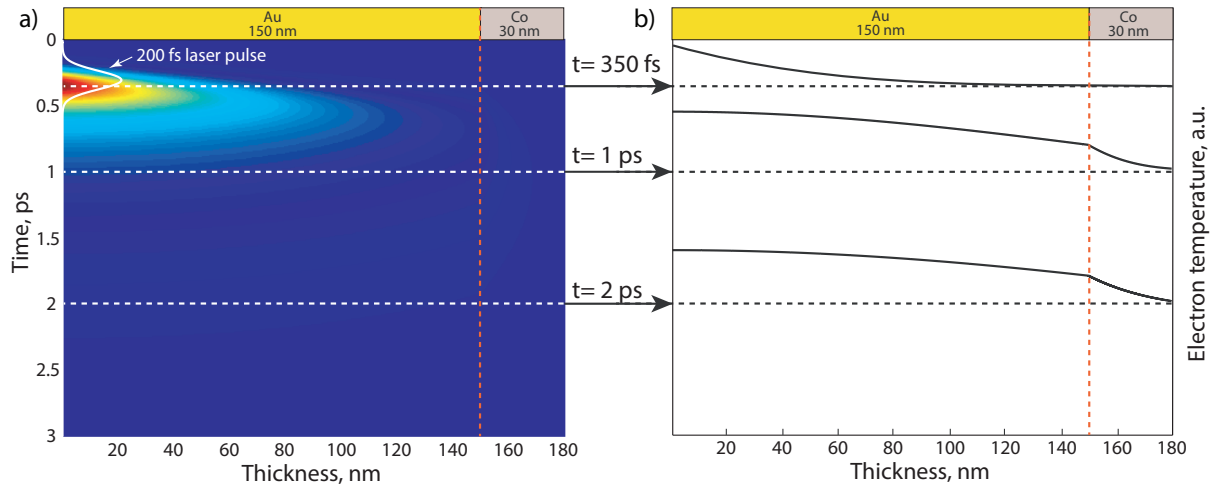

Figure 3.18: a) Distribution of the electron temperature after absorption of a 200 fs laser pulse as a function of a thickness and a time in gold/cobalt structure. The electron temperature grows extremely rapidly close to the surface of excitation and then redistributes all over the structure through the fast diffusion. b) Spatial profiles of T_e multiplied by a scaling coefficients are shown for times at $t = 0.35$ ps, 1 ps and 2 ps. The spatial profile of T_e established after $t = 1$ ps has much wider profile in gold than in cobalt, which is conform with a values of the electron mean free path for these materials.

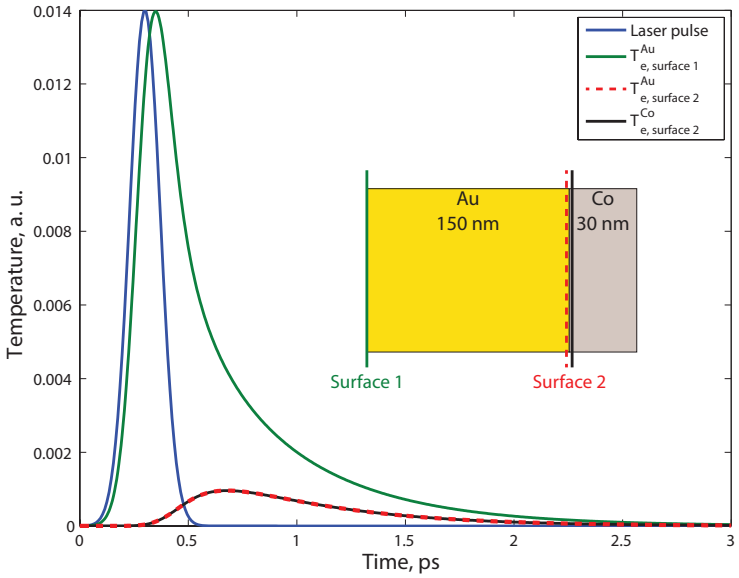

Figure 3.19: Temporal profiles of T_e along two interfaces: *Surface* 1 that is the free surface of the gold and *Surface* 2 that is the gold/cobalt interface. The green line is T_e at the *Surface* 1 that shows a fast growth of the temperature reaching maximum value 50 fs after arrival of the laser pulse. Both, red dashed line and black solid line are temperatures in gold and cobalt in the very proximity to the *Surface* 2 and they show the continuity of the electron temperature through the interface.

the Fermi velocity in gold $v_F^{Au} = 1.4 \cdot 10^6$ m/s and 150 nm thickness of the gold layer). The first spatial profile that corresponds to the electron temperature distribution 150 fs after the laser pulse arrival is shown in Fig. 3.18 b). We can notice that the electron temperature in the cobalt layer is very small as compared to the gold layer because concentration of electrons that reached the cobalt layer is low. However, within next 650 fs (second profile in Fig. 3.18 b)) the electron temperature in the cobalt layer increases forming an exponential profile. In the same time distribution of the electron temperature inside the gold layer is quasi-homogeneous. The last profile shows dramatic decrease of amplitudes of the electron temperature in both layers because electrons transfer their energy to the lattice.

The electron diffusion in both gold and cobalt is in good conformity with the values of the electron mean free path that characterize their penetration rate in the material. In gold the electron mean free path is very long, like also for other noble metals $l_{electron}^{Au}$ =40 nm[7,8,9,5]. From the other hand, in case of cobalt, that is a ferromagnetic material, the electron mean free path is very small and it is estimated to be $l_{electron}^{Co} = 1$ nm[12,3]).

It is useful to compare the temporal profiles of T_e along two surfaces depicted in Fig. 3.19, where *Surface* 1 denotes gold free surface and *Surface* 2 denotes the interface between gold and cobalt. The electron temperature at the free interface (green solid line) rises very rapidly reaching maximum just 150 fs after arrival of the laser pulse (blue solid line). The two other profiles denote the electron temperatures in a close proximity to *Surface* 2 from the gold side (red dashed line) and from the cobalt side (black solid line). These profiles are identical because of zero Kapitza resistance. Dynamics of the T_e show very fast cooling of the electron-gas and reaching equilibrium after $t \approx 2.5$ ps.

Lattice temperature

The calculated distribution of the lattice temperature T_i is shown in Fig. 3.20 a) and b). We can notice that the dynamics of lattice heating do not follow, but is characterized by the smooth monotonous growth of T_i in both layers. Slow lattice temperature growth is governed by the difference between electron and phonon temperatures and is proportional to the electron phonon coupling coefficient (term $g(T_e - T_i)$ given in Eq. (1.3)). Therefore, the lattice temperature growth stops when the system approaches the equilibrium ($T_e = T_i$).

The most interesting result from this simulation is a high temperature jump on the interface between gold and cobalt predicted by Eq. (1.35). We can see that the distribution of the lattice temperature saturates at the time $t = 2$ ps. The overheating at the gold/cobalt interface that is equal to 12.8. Estimated value is very close to the value 13.5 predicted by Eq. (1.35). The value of the overheating changes slightly at the time $t = 3$ ps, but afterwards stays on the same level (12.9), because the temperature of the electrons has reached equilibrium with the lattice.

As it was mentioned in the previous chapter 1.1 the origin of such extraordinary overheating of the cobalt layer is explained by larger electron-phonon coupling coefficient that allows

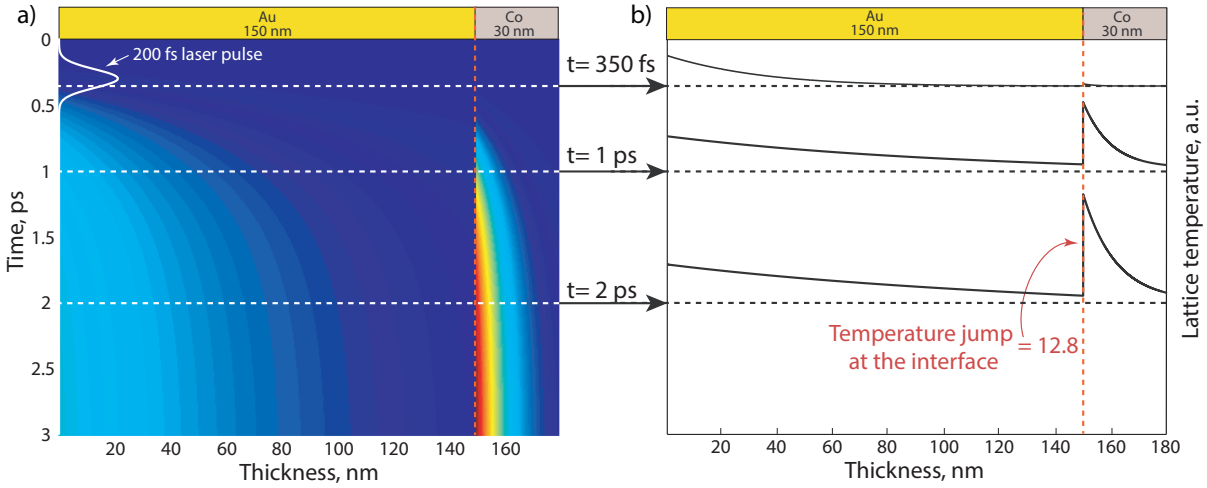

Figure 3.20: a) Distribution of the lattice temperature as a function of thickness and time in gold/cobalt structure. In both layers the temperature rises much slower than T_e and reaches a quasi-constant level at 2 ps. b) Spatial profiles of T_i at $t = 0.35$ ps, 1 ps and 2 ps reveal progressive overheating of the cobalt layer. Final temperature jump at the gold/cobalt interface is equal to 12.8.

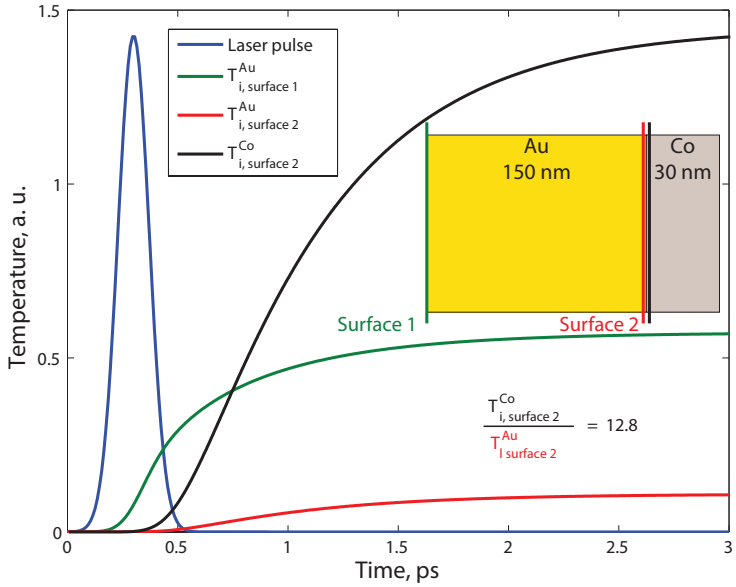

Figure 3.21: Temporal profiles of lattice temperature along two interfaces: *Surface* 1 and *Surface* 2. At the equilibrium the temperature jump at the gold/cobalt interface (*Surface* 2) is equal to 12.8.

to couple more efficiently hot electrons.

Established profile of the lattice temperature allows to extract the diffusion lengths. Therefore, consideration of the low-fluence regime results in $\zeta_{diff}^{Au} = 100$ nm for gold and $\zeta_{diff}^{Co} = 13$ nm for cobalt. The values obtained from simulation differs by 44% for gold and by 8% for cobalt from the values estimated from acoustic strain profiles. Therefore we can conclude, that in experiment the injected laser flux heated up the electron-gas by big enough value to cause the variation of the thermal conductivity and the electron heat capacity constants. This assumption will be checked in the section dealing with the analysis of acoustic pulses, where we will try to fit the coherent acoustic transients using the results of TTM simulations.

The evolution of the temporal profiles along *Surface* 1 and *Surface* 2 introduced previously are shown in Fig. 3.21. From this figure we can clearly see that the system reaches equilibrium after ≈ 2 ps.

3.2.2 TTM simulations with the Kapitza resistance

In this section we will investigate the influence of the Kapitza resistance of the gold/cobalt interface equal to $R_{Kap}^{Au/Co} = 5e^{-10}\text{Km}^2/\text{W}$. Given the case that the Kapitza resistance of the metal-metal interface has a major electron contribution[16] we will consider only the electron transport. We will see how the Kapitza resistance influence the electron and lattice temperature distributions and will estimate the overheating of the cobalt layer. In order to take into account the influence of the Kapitza resistance we need to use the modified expressions of the coefficients c_{11}, c_{12}, c_{21} given by Eq. (1.54).

Electron temperature

Similarly to the previous analysis we start with the evaluation of the dynamics of the electron transport that are shown in Fig. 3.22 a). We can notice that electron diffusion is still very efficient, but the fraction of electrons penetrating into the cobalt layer became significantly smaller. As a result, more electrons stay inside the gold layer and will heat its lattice.

From Fig. 3.22 b) we can quantitatively examine the evolution of the electron temperature. The first profile corresponds to time $t = 350$ fs and shows the same exponential profile as without the Kapitza resistance. In contrast to the previous simulation, at the time $t = 1$ ps the temperature profile inside the gold layer already reaches the homogeneous distribution. We can also notice a remarkable jump of the temperature for $t = 1$ and $t = 2$ ps at the gold/cobalt interface resulting in 4 times smaller electron temperature inside the cobalt layer. The profile of the electron temperature remains exponential.

Temporal evolution of the electron temperatures along *Surface* 1 and *Surface* 2 are shown in Fig. 3.23. We can extract the jump of the temperature between gold (red solid line) and cobalt (black solid line) at the gold/cobalt interface by the factor of 4.

We have seen that the electron flux through the gold/cobalt interface is dramatically

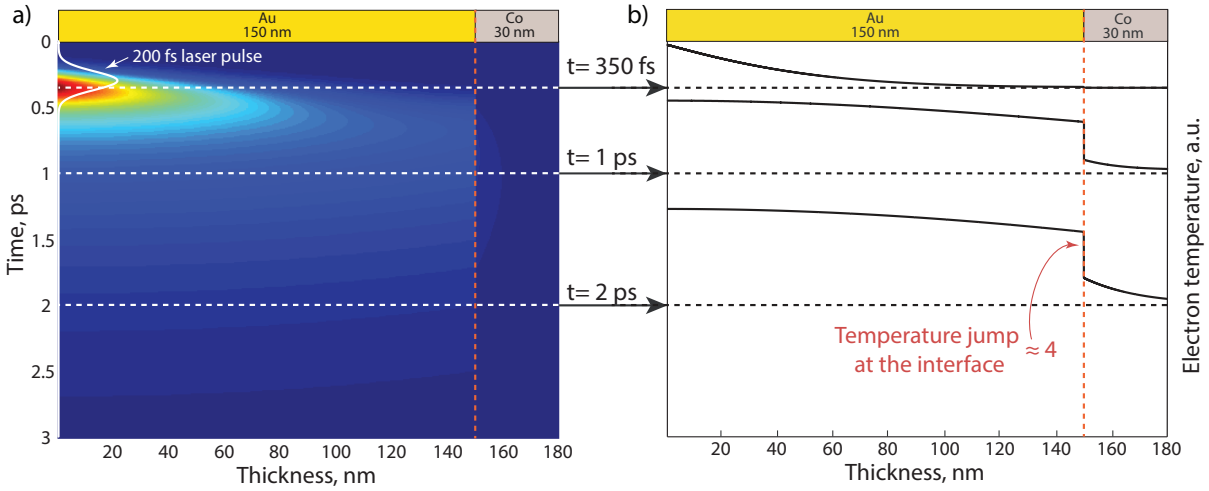

Figure 3.22: a) Distribution of the electron temperature after absorption of 200 fs laser pulse inside of gold/-cobalt layers with the Kapitza resistance. b) Spatial profiles of T_e at $t = 0.35$ ps, 1 ps and 2 ps demonstrate a temperature drop at the gold/cobalt interface by a factor of 4, which is caused by presence of the Kapitza resistance.

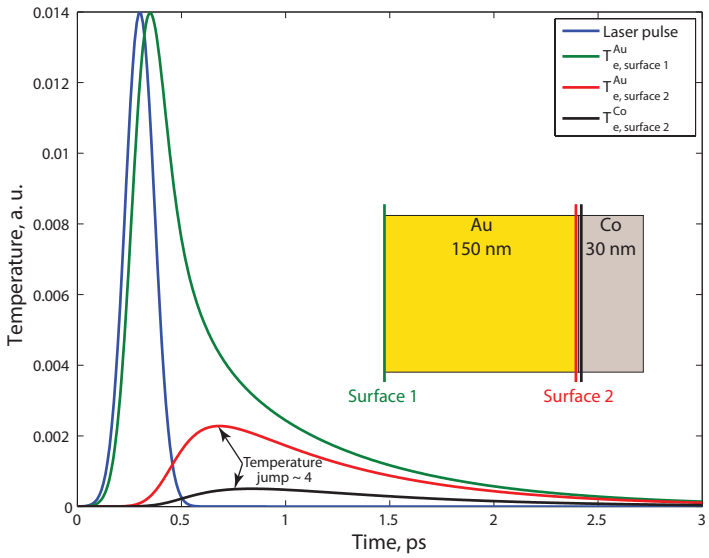

Figure 3.23: Temporal profiles of the electron temperatures along *Surface* 1 and *Surface* 2 calculated with the Kapitza resistance. Dynamics of the temperature at the free interface (green solid line) is almost identical to previously calculated dynamics. The temperature for $t = 1$ and $t = 2$ ps at the gold/cobalt interface resulting in 4 times smaller electron temperature inside the cobalt layer.

reduced after introduction of the Kapitza resistance. As a result, we can expect that the lattice temperature in the cobalt layer will reach much smaller values. However, the profile of the lattice temperature should remain the same for cobalt, but in gold, it will become almost rectangular in shape at $t = 1$ ps.

Lattice temperature

Dynamics of the lattice temperature with the Kapitza resistance are shown in Fig. 3.24 a). By inspecting this figure we can notice that maximum amplitudes of T_i in gold and cobalt do not differ as much as in the case of an ideal interface without the Kapitza resistance. Previously we have seen that the overheating of the cobalt layer reached 12.8 times, but when we introduced the Kapitza resistance the electron temperature dropped by a factor of 4. Therefore we can expect that overheating that relies on the amount of the electrons will be around $12.8/4 = 3.2$ times.

Closer analysis of the lattice temperature profiles is given in Fig. 3.24 b). The first profile corresponding to the time $t = 0.35$ ps shows no difference with the profiles simulated for an ideal interface. However, the two other profiles are significantly different and display much smaller overheating of the cobalt layer. At the time $t = 2$ ps the overheating reaches a factor of 3.5 that is very close to the estimation based on the reduced electron flux.

Additionally, we can observe a small spatial broadening T_i profile in gold that is 30 nm wider and reaches $\zeta_{diff}^{Au} = 130$ nm due to the increased amount of electrons that stayed inside the gold layer close to the gold/cobalt interface. The diffusion length in cobalt remains unchanged $\zeta_{diff}^{Co} = 13$ nm, as it was expected.

Now we will examine the temporal evolution of the lattice temperature along two boundaries at *Surface* 1 and *Surface* 2 given in Fig. 3.25. We can notice that in the case of the Kapitza resistance the equilibration of the lattice temperature occurs at $t = 2.5$ ps. However, the value of the overheating established even for $t = 2$ ps is the same as for $t = 3$ ps and equal to 3.5.

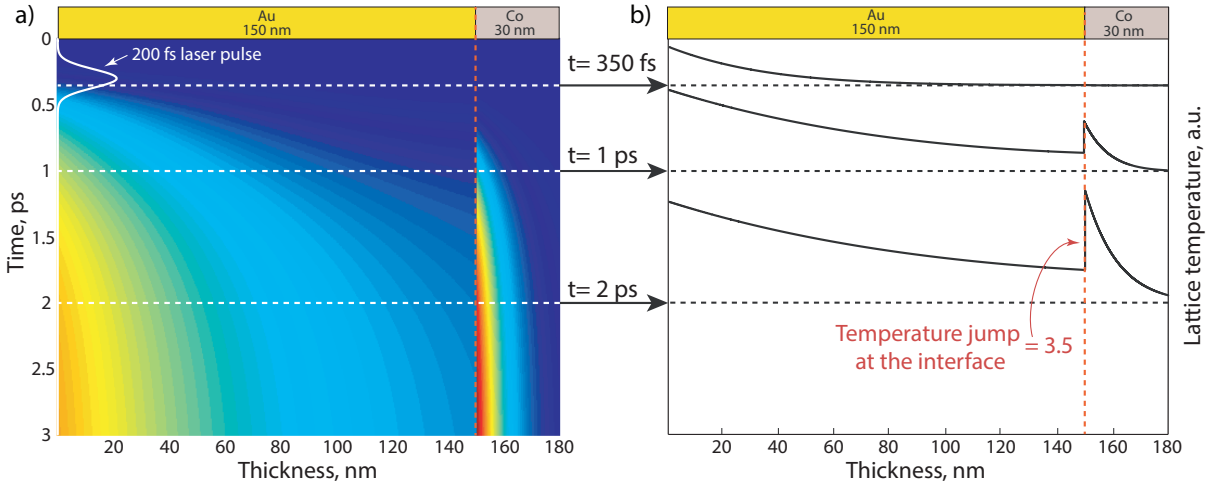

Figure 3.24: a) Distribution of the lattice temperature inside the gold/cobalt strucure with consideration of the Kapitza resistance equal to $R_{Kap} = 5 \cdot 10^{-10}$ m^{2}KW^{-1} resulting in much smaller overheating of the cobalt layer. b) Spatial profiles of T_i at $t = 0.35$ ps, 1 ps and 2 ps show widening by 30 nm of the temperature profile of the gold layer and smaller 3.5 factor of overheating of the cobalt layer.

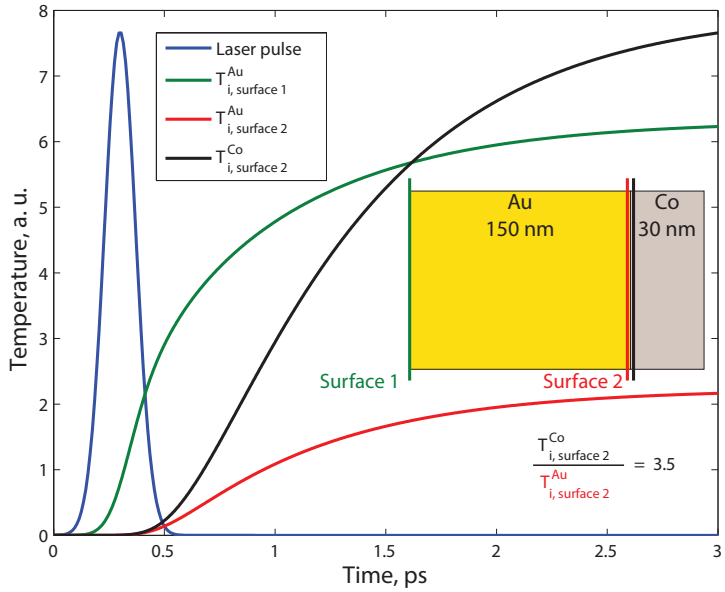

Figure 3.25: Temporal profiles of lattice temperature along two interfaces: *Surface* 1 and *Surface* 2. At the equilibrium the temperature jump at the gold/cobalt interface (*Surface* 2) is equal to 3.5 because of the introduced electron Kapitza resistance for the gold/cobalt interface.

3.2.3 Conclusion

Application of the TTM for a study of the electron diffusion in bimetallic structures has shown the origin of the overheating of the cobalt layer. Simulation showed that a time necessary for electron and phonon sub-systems to reach equilibrium is about $t = 2$ ps, that is in good agreement with the low-fluence regime[28]. The profiles of the established lattice temperatures indicate that the diffusion length in gold is $\zeta_{diff}^{(TTM),Au} = 100$ nm and in cobalt is $\zeta_{diff}^{(TTM),Co} = 13$ nm. When considering the Kapitza resistance of the gold/cobalt interface the diffusion length in gold becomes $\zeta_{diff}^{(TTM),Au} = 130$ nm and the diffusion length in cobalt remains unchanged. For the reference, the profiles of the lattice temperature obtained from the acoustics pulse shape are $\zeta_{diff}^{(Exp),Au} = 180$ nm and $\zeta_{diff}^{(Exp),Co} = 12$ nm.

The overheating of the cobalt layer from simulation is equal to 12.8, but in experiment we observed a factor of 3. We can conclude, that the experiments were performed under conditions of high laser excitation (see section 3.3.2).

By introducing the electron Kapitza resistance for the gold/cobalt interface estimated in the COMSOL fitting section to be $R_{Kap}^{Au/Co} = 5e^{-10}\mathrm{Km}^2/\mathrm{W}$ the electron flux through this boundary and the lattice temperatures in cobalt dramatically dropped. In analysis of the electron transport we have seen temperature drop by a factor of 4. As a result, temperature in the cobalt layer is 3.5 times bigger that in the gold layer. Application of the Kapitza resistance increased the heat diffusion length to $\zeta_{diff}^{TTM,Au} = 130$ nm. But still we have a significant difference between observed and simulated TTM lattice profiles.

3.3 Analysis of coherent acoustic signal in gold-cobalt structure

So far we have conducted the analysis of the incoherent (thermal) component of the reflectivity signal that allows to study thermal transport. The coherent (acoustic) component of the reflectivity signal allows to determine not only elastic properties of the sample but also contains the information about the initial lattice temperature distribution. This distribution was used in the previous sections where we simulated the thermal background using COMSOL.

In this section we will examine pure acoustic echo signals measured in the sample consisting of 240 nm of gold and 30 nm of cobalt. Instead of fitting different acoustic echoes (one generated in gold and another in cobalt) separately we will fit the entire signal simultaneously. On the first stage, the thermal background simulated by COMSOL will be subtracted from the experimental reflectivity signal. Then, we will use the same initial temperature distribution, that was defined to fit the thermal background, as a generated strain inside both layers to fit the remaining part of the reflectivity. After that we will use another approach to fit acoustics that is based on solution of the TTM with the electron temperature and the Kapitza resistance as fit parameters to reproduce the acoustic signal.

3.3.1 Analysis within one temperature model

In order to extract the acoustic component from the reflectivity signal we need to cut the data points in experimental curve for $t < 4$ ps because our COMSOL simulation reasonably describes the heat dynamics only when electron-phonon relaxation is over.

The coherent acoustic component of the measured reflectivity shown in Fig. 3.26 by black solid line. It was obtained after subtraction of the thermal background simulated in COMSOL (red dashed line) from the experimental reflectivity (blue solid line).

The acoustic signal shows the presence of two strains propagating inside the sample, long bipolar strain generated in the gold layer and short strain generated by hot electrons in the cobalt layer. In the original reflectivity curve we can distinguish clearly only first echo from the gold and second echo from the cobalt (see Fig. 3.26). However, after subtraction of the thermal background, the first echo from cobalt (mixed initially with the fast thermal signal) becomes more pronounced. Also we can notice the presence of a small signal that can be characterized as the second gold echo that made an additional acoustic round trip through the metal bilayer.

The first long bipolar strain generated in gold reaches the cobalt/sapphire interface at 73 ps (time point corresponding to central part of the bipolar strain pulse). The total arrival time $\tau^{Au} + \tau^{Co}$ consists of $\tau^{Au} = 69.5$ ps to traverse 240 nm gold layer at the sound speed $c_s^{Au} = 3.45$ nm/ps[51] and of $\tau^{Co} = 4.5$ ps to cross 30 nm cobalt layer at the sound speed

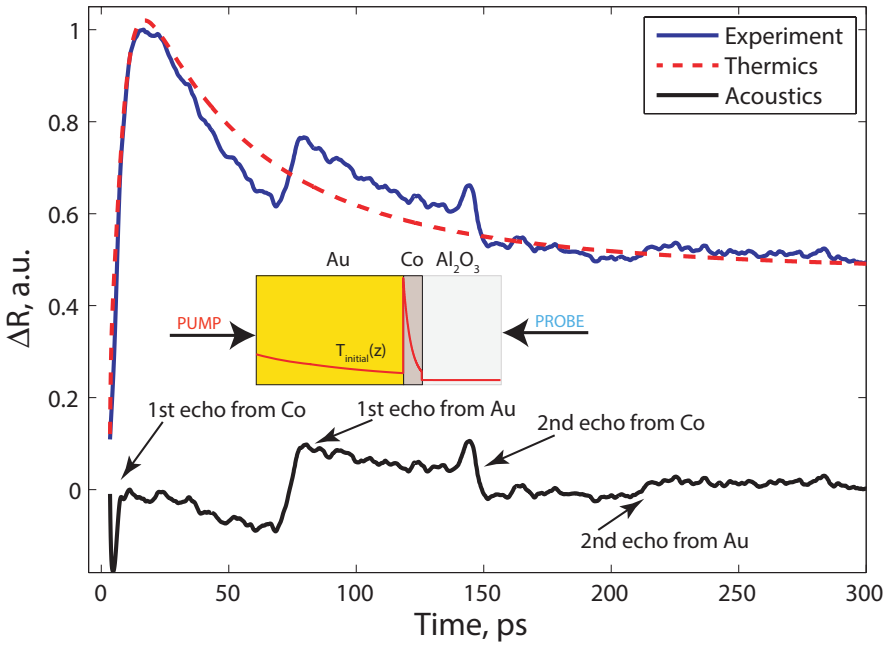

Figure 3.26: Extraction of the acoustic component (black solid line) from the reflectivity signal (blue solid line) by subtraction of the simulated thermal background (red dashed line) that is depicted in the inset.

$c_s^{Co} = 6.3$ nm/ps[52]. As a result, estimated time of strain arrival is 74 ps that is very close to the experimental time 73 ps.

The ultrashort (3 ps FWHM) cobalt strain detected at $t = 146$ ps arrives at the detection interface after one round trip in the gold-cobalt layers. From the other hand the estimation gives arrival time equal to 148 ps, that is still very close to observation.

Two other echoes : 1st echo from cobalt and 2nd echo from gold are barely pronounceable and will be discussed afterwards.

Simulation of the strain pulse shape

To reproduce these echoes we will use the initial temperature distribution depicted in the inset in Fig. 3.26. This distribution is characterized by $\zeta_{diff}^{Au} = 180$ nm heat diffusion of gold and $\zeta_{diff}^{Co} = 12$ nm heat diffusion of cobalt with the overheated cobalt layer by a factor of 14.5. Such distribution of the temperature generates the strain proportional to the linear thermal expansion coefficients α given for gold and cobalt in Table 3.3.

Table 3.3: Linear thermal expansion coefficient of gold and cobalt

Property\Material	Gold	Cobalt	Unit
Thermal expansion	$14{\cdot}10^{-6}$ [76]	$13{\cdot}10^{-6}$ [76]	$[\alpha] = [\mathrm{K}^{-1}]$

As we can notice, the difference of thermal expansion coefficients for both metals differs by less than 10%. The next step involves solving the acoustic wave equation by the algorithm described in chapter 2.3 for initial strain distribution governed by heat diffusion parameters

and the overheating factor of the cobalt layer. It will be informative to show the spatial strain distribution inside the gold/cobalt/sapphire structure for different times shown in Fig. 3.27.

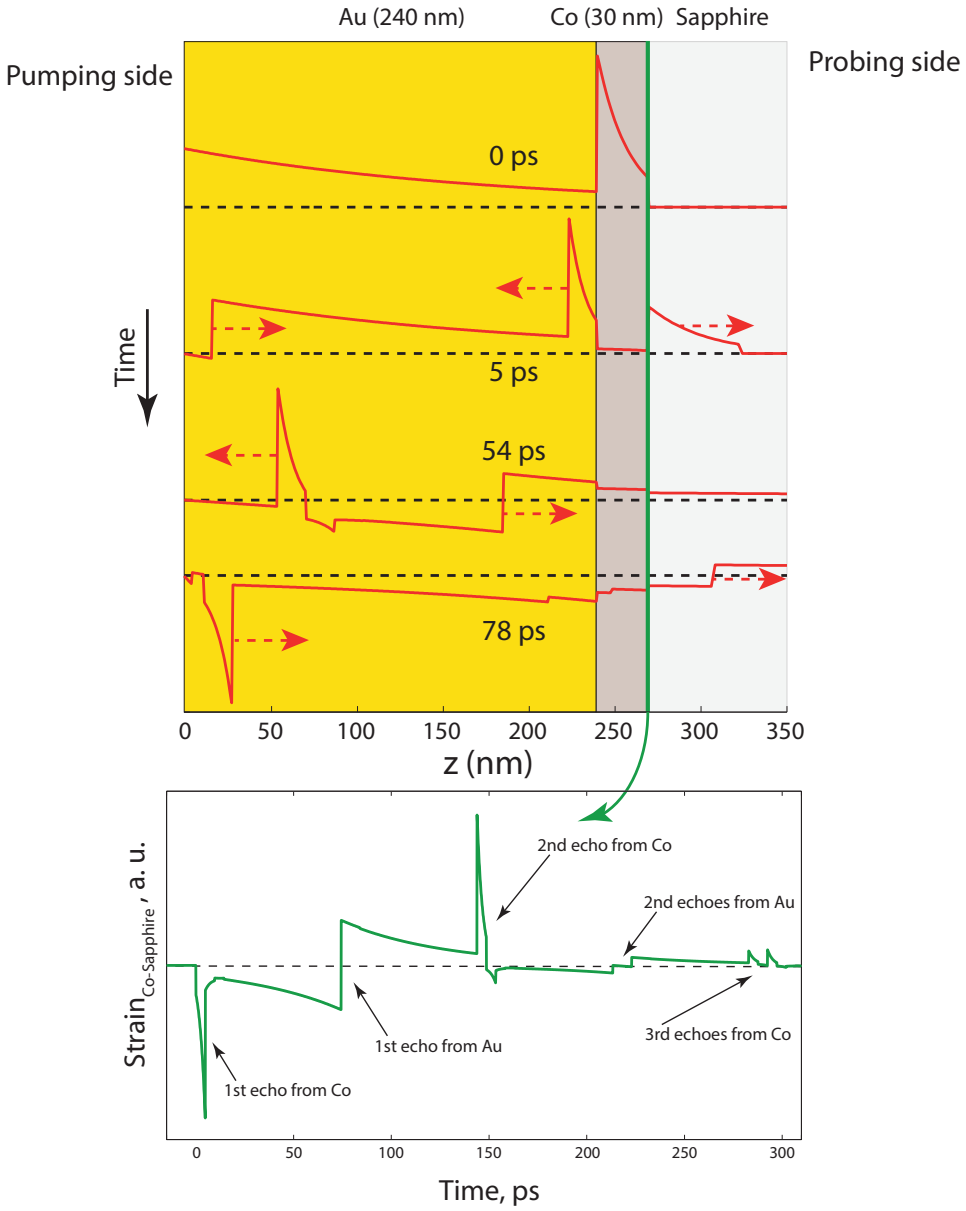

Figure 3.27: (top panel)Progressive spatial profiles of complex strain distribution $\eta(t)$ that propagates with indicated by red arrows directions. (bottom panel) Temporal profile of the strain at the cobalt/sapphire interface that is shown by green solid line with depicted indications of the origin of each strain pulse.

The initial strain distribution given for $t = 0$ ps emits two strains with half amplitude and propagating in opposite directions: one towards sapphire substrate and another towards gold.

At $t = 5$ ps the ultrashort cobalt strain generated by the hot electrons leaves the cobalt layer. One half of this strain was injected into the sapphire substrate and changes the shape due to the 2 times greater sound speed in sapphire (that results in strain widening and

amplitude decrease by a factor of 2). Another strain is injected into the gold layer and undergoes the change in shape as well. But in this case it shrinks and increases in amplitude by a factor of 2 because the sound speed in gold is almost two times smaller than in cobalt. From the other side the profile of the strain generated in the gold layer has bipolar shape because one half of the initial strain is reflected at the free interface.

At the time $t = 54$ ps the bipolar gold strain almost reaches the detection interface and it can be noticed that the cobalt strain contains a small tail that is 10% reflection occurred at the cobalt/sapphire interface for the component propagating towards the sapphire substrate.

Final profile at $t = 78$ ps corresponds to the moment of passage of big bipolar strain pulse through the cobalt/sapphire interface and we can notice two small reflections that will be detected later at the time $t = 220$ ps.

Temporal evolutions of the strain at the interface between cobalt and gold shown in the bottom panel in Fig. 3.27 reproduce all the strain echoes predicted before. At very short times there is the first echo from cobalt that propagates towards the substrate. After that, at t =73 ps the long bipolar strain generated in gold arrives at the cobalt/sapphire interface. By the time of the round trip in gold/cobalt layers ($t = 146$ ps) the second echo from cobalt is observed. And finally, two small 10% reflections of the gold strain from the gold/cobalt and cobalt/sapphire interfaces arrive around $t = 220$ ps.

Fit of the reflectivity

Unfortunately, the photoelastic coefficients of cobalt are not known, thus we use the ratio of the dimensionless parameters A and B responsible for the photoelastic interaction as a fit parameter. The best fit to the experimental data was achieved when B was tending to zero, as a result the sensitivity function $G(t)$ contained only smooth sine-component related to A term (see Section 2.4).

Other constants like Brillouin frequency $\omega_{Br} = 2\pi \cdot 45$ GHz and the acoustic time-of-flight $\tau_{skin} = 1.68$ ps through the skin depth $\delta_{skin} = 10.6$ nm were calculated using the complex index of refraction for cobalt at 400 nm probe wavelength $\tilde{n} = 1.56 + 2.9i$[55].

The strain distribution obtained in the previous step (bottom panel in Fig. 3.27) was used to calculate the reflectivity by taking a convolution $\int \eta(t)G(t-\tau)d\tau$with the sensitivity function $G(t)$ (shown in inset in Fig. 3.28). Superposition of the coherent acoustic signal extracted from the experiment (blue solid line) with the simulated reflectivity response produced by the simulated strain distribution (red solid line) is shown in Fig. 3.28. Additionally, the profile of the strain before the convolution with the sensitivity function is shown as black solid line.

We can notice that the sensitivity function smoothes all the sharp edges and lead to the decrease of the amplitude of the cobalt strain by a factor of three. However, the simulated cobalt echo still has 2.5 times greater amplitude than in the experiment. Therefore the actual amplitude of the overheating of the cobalt layer should be around 5.5, but not 14.5

like it was used in the COMSOL simulations.

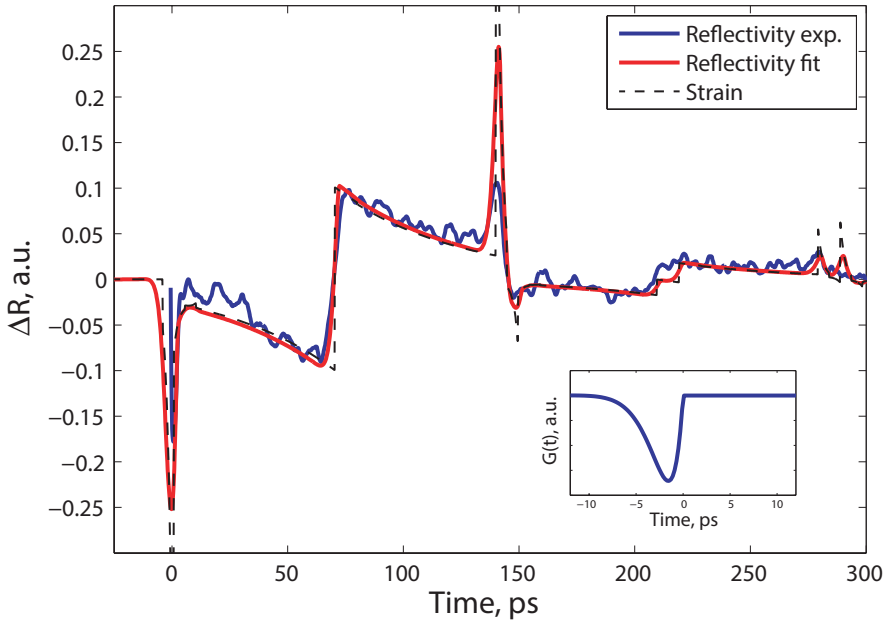

Figure 3.28: Experimental reflectivity data without thermal background (blue solid line) are fitted using a convolution of the simulated strain distribution (black dashed line) with the sensitivity function $G(t)$ (see the inset) that results in reflectivity fit shown by red solid line.

We have shown that the numerical approach, which neglects the interaction of the laser light with the electrons and starts from the distribution of the established lattice temperature represents an efficient simplification. It allows to explain reasonably well the heat diffusion dynamics (thermal background of the reflectivity signal) as well as to fit the entire acoustic signal. The only failure of this approach is an overestimation of the energy injected in the cobalt layer. However, it allows to correctly reproduce the duration of both strain pulses.

Moreover, we are able to explain the small step-like signal at $t = 215$ ps caused by two small 10% reflections of the bipolar gold strain from the gold/cobalt and cobalt/sapphire interfaces.

3.3.2 Analysis within two temperature model

In this section we will try to reproduce the strain profiles generated in the gold/cobalt layers using the TTM. It was shown in section 3.2.2 that the electron diffusion depth was smaller than in experiment. The electron diffusion depth is related to the value of the electron temperature T_e through the thermal conductivity $k(T_e)$ and the electron heat capacity $C_e(T_e)$ which are assumed to depend linearly from T_e [28,31,16]. The value of the overheating of the cobalt layer will be fitted by the Kapitza resistance.

It was possible to fit the diffusion profile in gold ($\zeta_{diff}^{Au} = 180$ nm) by the electron temperature $T_e = 750$ K. In the first TTM simulation we will consider the Kapitza resistance of the gold/cobalt interface that was obtained previously by COMSOL fitting : $R_{Kap} = 4.5 \cdot 10^{-10}$

Km^2/W. Superposition of experimental (blue solid line) and calculated reflectivities (red solid line) are shown in Fig. 3.29. As a result of greater electron temperature the diffusion process is more efficient, thus spatial extent of the lattice profile in gold also increases. The TTM fit is in good agreement with the acoustic echo generated in gold. However, the cobalt echo was underestimated by the considered Kapitza resistance (amplitude of simulated cobalt strain is 1.6 times smaller).

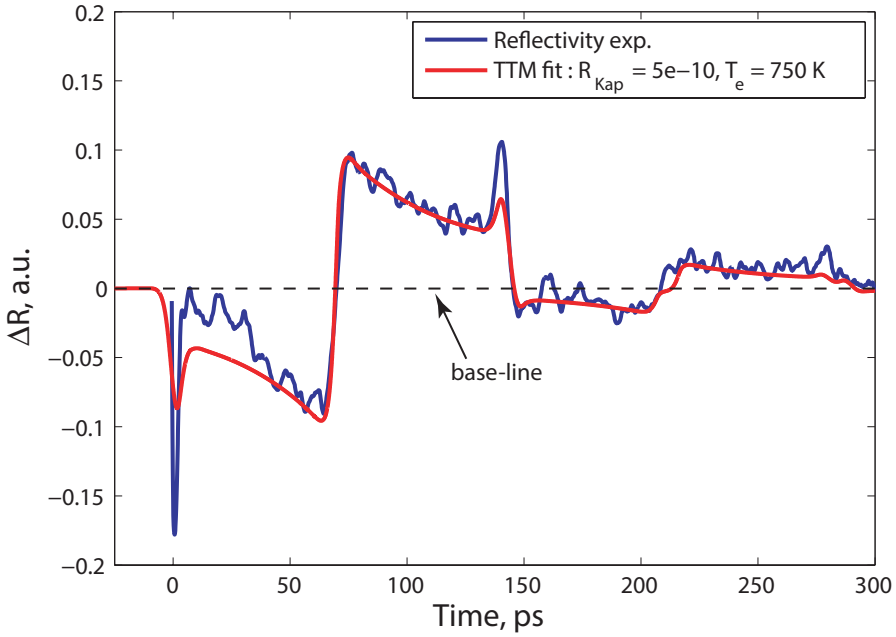

Figure 3.29: Experimental reflectivity without thermal background (blue solid line) is fitted using TTM (red solid line) for $T_e = 750$ K and $R_{Kap} = 4.5 \cdot 10^{-10}$ Km^2/W. Spatial profile of the simulated reflectivity reproduces well the gold echo but underestimates the cobalt echo by 1.6 times.

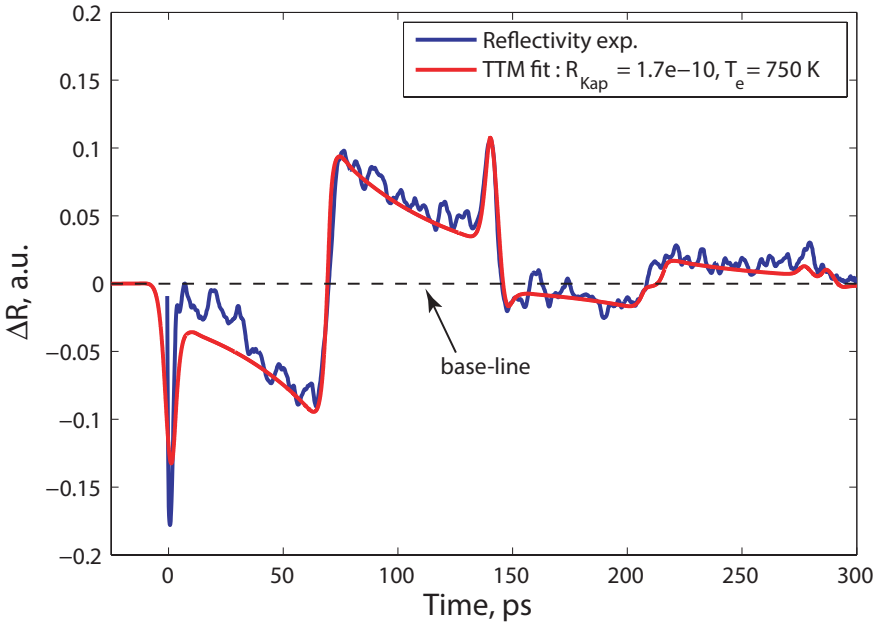

Figure 3.30: Experimental reflectivity data without thermal background (blue solid line) is fitted using TTM (red solid line). Spatial profile of the simulated reflectivity with adjusted Kapitza resistance to the value $R_{Kap} = 1.7 \cdot 10^{-10}$ Km^2/W is in good agreement with the experiment.

The best agreement with the experimental curve was reached for the Kapitza resistance $R_{Kap} = 1.7 \cdot 10^{-10}$ Km^2/W with the same electron temperature $T_e = 750$ K that is shown in Fig. 3.30 by red solid line. The smaller value of the Kapitza resistance allowed to reach the quantitative agreement with the experiment by increasing the overheating of the cobalt layer.

Eventually, it was shown by Cahill et.al.[16] that the Kapitza resistance is also temperature dependent $R_{Kap} = R_{Kap}(T)$ and drops for higher temperatures. It was observed experimentally that by heating the aluminum/copper sample from 200 K to 300 K the Kapitza resistance decreases by a factor of 2.5. Therefore, our simulation performed in COMSOL estimates only the average value of the Kapitza resistance that undergoes changes during the cooling of both gold and cobalt layers.

The smaller value of the Kapitza resistance obtained by TTM simulation assumes that the strain generation occurs only within first few picoseconds after the laser absorption. This small time window is characterized by high temperature within the gold/cobalt interface that can explain 2.6 times smaller Kapitza resistance of this interface as compared to the COMSOL results.

3.3.3 Conclusion

During first attempts of the analysis of the acoustic component of the transient reflectivity (that was obtained by subtraction of the thermal background simulated by COMSOL from the transient reflectivity curve) we achieved to reproduce qualitatively all acoustic echoes detected in the experiment. We used the strain distribution proportional to the initial temperature profiles of gold and cobalt layers (the same as the one used during COMSOL simulations of the thermal background that allowed to extract the acoustic component). This strain distribution was in good agreement with the gold echo but failed to fit the amplitude of the cobalt echo. That is why we performed the TTM simulation that allowed to achieve a good quantitative agreement with the experiment. For that we increased the electron temperature to $T_e = 750$ K in order to increase the diffusion length of electrons to reach $\zeta_{diff}^{Au} = 180$ nm. It turned out, that the value of the Kapitza resistance estimated by COMSOL fitting $R_{Kap}^{Au/Co} = 4.5 \cdot 10^{-10}$Km^2/W underestimates the lattice temperature growth inside the cobalt layer. The best agreement was achieved for the Kapitza resistance that is 2.6 times smaller $R_{Kap}^{Au/Co} = 1.7 \cdot 10^{-10}$Km^2/W. Taking into account that the Kapitza resistance is temperature dependent $R_{Kap} = R_{Kap}(T)$[16] (the Kapitza resistance decreases for high temperatures) we assume that the value estimated by COMSOL fitting is an averaged value that can be smaller within first picoseconds during the acoustics generation when the system is extremely hot.

Moreover, we estimated the sensitivity function $G(t)$ (related to the opto-elastic coefficients) of cobalt for 400 nm wavelength. Similarly to the work of Manke et.al.[6] we determined that the dimensionless parameter $B = 0$ and as a result the sensitivity function $G(t)$

has only a smooth component related to other dimensionless parameter A.

In this section we have seen that the thermo-elastic model of the strain generation allows to quantitatively reproduce the experimental data measured for the gold/cobalt/sapphire sample. The profiles of the acoustics generated in gold and cobalt are in good agreement with the experiment. However, the overheating of the cobalt layer assumed during the COMSOL simulation appears to overestimate the amplitude of the strain by a factor of 2.5.

Also it was shown, that the algorithm of solution of the acoustic wave equation succeed to reproduce the arrival of all the echoes observed experimentally.

3.4 Analysis of the magnetic signal

The remaining part of the analysis is related to the measurements made by the Kerr rotation setup explained in Section 2.6.4. The Kerr rotation signal (black solid line) in Fig. 3.33 shows the oscillation of magnetization in cobalt, which represents the manifestation of the thermal dynamics in ferromagnetic cobalt.

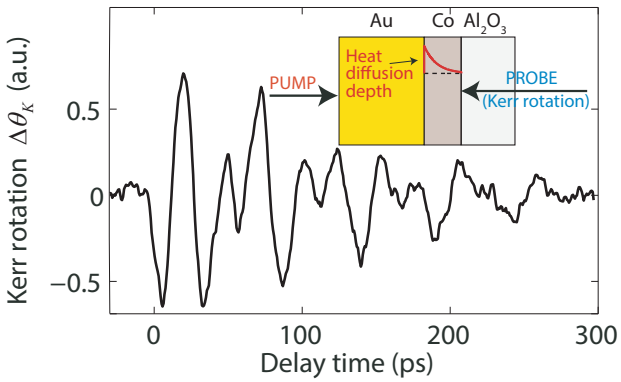

Figure 3.31: Magnetization oscillations measured by Kerr rotation that was triggered by diffusive electrons excited in gold (black solid line).

Similar to the results of the direct optical excitation of ferromagnets with ultrashort optical pulses[77], here we observe magnetization oscillations triggered by diffusive electrons. The magnetization precession contains two damped oscillations: a low-frequency ferromagnetic resonance (FMR) and at least one high-frequency magnon mode. The physical interpretation is identical to that by van Kampen et al.[77], who discovered that both the spatially homogeneous FMR and inhomogeneous magnon modes are excited by a rapid change of magnetocrystalline anisotropy in ferromagnet.

The frequency of the FMR ω_{FMR} depends on the geometry of the structure that is shown in Fig.3.32. In this geometry the relative orientation of the applied external magnetic field $\vec{H}$ and the magnetization vector $\vec{M}$ is given by angles α and θ respectively.

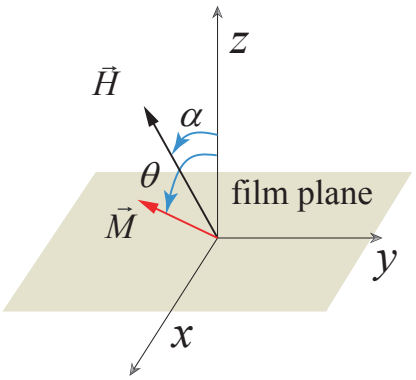

Figure 3.32: Relative orientation of the magnetization vector $\vec{M}$ and the applied field $\vec{H}$ with respect to the film plane.

For such geometry the frequency of the FMR is given by[78]

$$\left(\frac{\omega_{FMR}}{\mu_0\gamma}\right)^2 = (H\cos\alpha - H_{eff}\cos\theta)^2 + H\sin\alpha\,(H\sin\alpha + H_{eff}\sin\theta)\,, \tag{3.3}$$

where H_{eff} is the effective anisotropy field.

Inhomogenious thermal excitation by diffusive electrons at gold-cobalt interface should also trigger the exchange-coupled magnons. The frequency of n-th magnon mode ω_n is given by

$$\omega_n = \omega_{\mathrm{FMR}} + D(n\pi/L)^2, \tag{3.4}$$

where D is the exchange stiffness coefficient ($D_{Co} = 466$ meVÅ^2)[79], n is the number of the mode and L is the thickness of the ferromagnetic layer.

The magnetization precession is quantitatively reproduced by the superposition of two damped oscillations (red solid line): a low-frequency ferromagnetic resonance ω_{FMR} (red dotted curve) and high-frequency first-order magnon mode ω_1 (blue dotted line) that are shown in Fig. 3.33

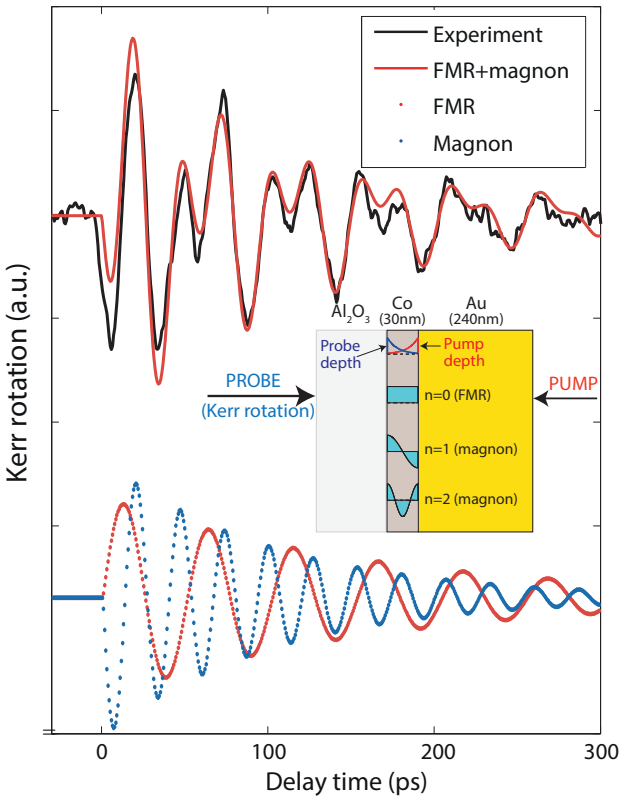

Figure 3.33: Magnetization oscillations measured by Kerr rotation that was triggered by diffusive electrons excited in gold (black solid line). The magnetization oscillations was fitted by in-phase excitation of FMR and magnon precession (red solid line). Two frequencies of FMR and first-order magnon mode are shown by blue dotted line and by red dotted line respectively.

Taking into account the sinusoidal spatial distribution of magnetization in a first-order magnon mode $M(z) = \cos(\pi \frac{z}{L})$ (see the inset in Fig. 3.33, $L = 30$ nm) we conclude that the spatially localized Kerr rotation probing at the cobalt-sapphire interface leads to π-phase shift.

It is important to note that efficient excitation of a spatially inhomogeneous standing magnon modes is an additional indicator of the spatially inhomogeneous temperature distribution within the cobalt layer, which was covered in the previous sections.

4

General conclusions and perspectives

Throughout this work we studied an extremely fruitful gold/cobalt structure. Remarkable electron diffusion of gold and strong electron-phonon coupling of cobalt allowed not only to study the carrier transport through the gold/cobalt interface, but also revealed a novel concept of the acoustic strain generation by superdiffusive electrons in adjacent cobalt layer.

Theory of the electron diffusion, based on the well-known Two-Temperature Model, illustrates an efficient approach of not only qualitative but also quantitative characterization of the femtosecond laser pulse excitation of diffusive electrons. Even though, by taking into account the electron Kapitza resistance of the gold/cobalt interface, the temperature dependence of the thermal conductivity and electron heat capacity, our simulations are in excellent agreement with the experimental observation of the acoustic strain profiles generated in both gold and cobalt.

This new mechanism of ultrashort strain generation may be used for the experimental demonstration of a theoretically predicted phenomenon of ultrafast non-thermal magnetization reversal in highly magnetostrictive material like Terfenol-D[80]. In this concept a key point relies on the precise control of amplitude and duration of picoseconds strain pulses which acoustically switch the direction of magnetization.

Knowledge of the spatial distribution of the acoustic strain profiles gives a direct estimation of the lattice temperature profiles established after the electron-phonon equilibration. We have putted in evidence that the lattice temperature distribution can be successfully used for the simulation of the heat diffusion in a single- and multilayer samples. These simulations allow to estimate the value of the Kapitza resistance at multiple interfaces using the transient reflectivity data and showed a good agreement with the values obtained by other experimental techniques and theoretical predictions.

The heat transport and especially the Kapitza resistance studies are very important in the domain of electronics and compact devices. Proper choice of the materials with a small

Kapitza resistance determines the cooling rate from overheated components. Even though the influence of the heat transfer through the interfaces increases when the element sizes shrinks. We detected a noticeable cooling rate improvement by introducing a thin cobalt film between gold and sapphire layers. It serves as an efficient buffer layer for the heat carriers propagating from the gold layer to the sapphire substrate because of the small Kapitza resistances for both gold/cobalt and cobalt/sapphire interfaces.

A

Appendix

A.1 TTM algorithm and MATLAB script

Analytic formulations discussed previously can be formalized in the following algorithm that will ensure correct calculation:

- Take the Fourier transform of the femtosecond laser pulse $f(t)$.
- Calculate the Maxwell's wave numbers $p^{1,2}$ from Eq. (1.18) paying attention that it should have positive real part.
- Determine coefficients c_{11}, c_{12} from Eq. (1.26) and c_{21} from Eq. (1.26).
- Calculate temperatures of electrons for both gold and cobalt layers in the frequency domain $\hat{T_e}^{1,2}$ using Eq. (1.19).
- Take the inverse Fourier transform of the temperature of electrons and use it to calculate the temperature of the lattice $T_i^{1,2}$ by Eq. (1.39).

The MATLAB script which performs mentioned above steps is given below:

```
clear all
close all
set(0,'Units', 'pixels', 'DefaultAxesFontSize',12,'DefaultAxesFontName'...
    ,'Helvetica','DefaultAxesFontWeight','normal'); % normal bold
%========== Definition of the temperatures ==========%
Tlattice = 300;                 % lattice temperature [K]
Te = 300;                       % electron temperature [K]

%========== gold constants ==========%
g1=2.3*10^(16);             % e-ph coupling [W m^-3 K^-1)]
k1=317 * Te / Tlattice;     % thermal conductivity [W m^-1 K^-1]
```

```
Ce1=71 * Te;                    % electron heat capacity [Jm^-3 K^-3]
Ci1=2.5*10^6;                   % lattice heat capacity [J m^-3 K^-1]
c_s_1 = 3450;                   % sound speed [m/s]
D1=k1/Ce1;                      % electron diffusivity
tau1=Ce1/g1;                    % e-ph relaxation time
%========== cobalt constants ==========%
g2=4.3*10^17;                   % e-ph coupling [W m^-3 K^-1)]
k2=69 * Te / Tlattice;          % thermal conductivity [W m^-1 K^-1]
Ce2=660 * Te;                   % electron heat capacity [Jm^-3 K^-3]
Ci2=3.5*10^6;                   % lattice heat capacity [J m^-3 K^-1]
c_s_2 = 6300;                   % sound speed [m/s]
D2=k2/Ce2;                      % electron diffusivity
tau2=(Ce2/g2);                  % e-ph relaxation time

%========== other definitions ==========%

initial_dt=0.06e-12;            % time step [s]
t_final = 6e-12;                % maximum time
time_temp = 0: initial_dt : t_final;

thicknessAu = 150e-9;           % thickness of gold [nm]
thicknessCo = 30e-9;            % thickness of cobalt [nm]

R_Kap = 5e-10;                  % Kapitza resistance [m^2 K W^-1]

%========== special acoustic mesh ==========%
delta_z1=c_s_1*initial_dt;  % mesh in gold
delta_z2=c_s_2*initial_dt;  % mesh in cobalt

%========== technical definitions ==========%
N1= fix(thicknessAu / delta_z1);      % calc. of number of points
N2= fix (thicknessCo / delta_z2);     % calc. of number of points
N_total=N1+N2;                        % total size of structure
d1=(N1-1)*delta_z1;

%========== time definition for the laser pulse ==========%
N_time=2^10 ;                         % number of points
delta_t=0.02e-12;                     % time step [ps]
tau_laser=100 * 1e-15;                % FWHM of the laser pulse
t0=0.15e-12;                          % time shift
Te_omega=zeros(N_total,N_time);
Te_final=zeros(N_total);
Ti_omega=zeros(N_total,N_time);
```

```
Ti_final=zeros(N_total);
z_show = zeros(1, N_total);

%========== laser pulse creation ==========%
for index_time=1:N_time
    time=delta_t*(index_time-N_time/2-0.5);
    time_show(index_time)=time;
    f_time(index_time)=10^8*exp(-(time - 2 * t0)^2/tau_laser^2);
end

%========== Fourier transform laser pulse ==========%
delta_omega=(2*pi/delta_t)/(N_time-1);

for index_omega=1:N_time
    omega=-pi/delta_t+delta_omega*(index_omega-1);
    omega_show(index_omega)=omega;
    int1=0;
    for index_time=1:N_time
      time=delta_t*(index_time-N_time/2-0.5);
      int1=int1+f_time(index_time)*exp(i*omega*time);
    end
    f_omega(index_omega)=int1;
end

%========== inverse Fourier transform laser pulse ==========%
for index_time=1:N_time
      time=delta_t*(index_time-N_time/2-0.5);
      int1=0;
for index_omega=1:N_time
    omega=-pi/delta_t+delta_omega*(index_omega-1);
      int1=int1+f_omega(index_omega)*exp(-i*omega*time);
    end
    f_reconstr(index_time)=int1/N_time;
end

figure(1)
    subplot(121)
    plot(time_show * 1e12,f_time,'-k',time_show * 1e12,...
    f_reconstr,'.r','LineWidth',2)
    title('Laser pulse & reconstructed laser pulse');
    xlabel('Time (ps)'); grid on; xlim([0 0.7]);

    subplot(122)
```

```
    plot(omega_show/(2*pi) * 1e-12,real(f_omega),...
    omega_show/(2*pi) * 1e-12, imag(f_omega));
    title('Real[Fourier transform of the laser pulse]');
    xlabel('Frequency (THz)');

%========== Calculation of the Te ==========%
for index_omega=1:N_time
   omega=delta_omega*(index_omega-1)-pi/delta_t;
   % calculation of the Maxwell wave numbers p
   p1=sqrt(-1i*(omega/D1)*(1 - (Ci1/Ce1)/(0 + 1i*omega*tau1*Ci1/Ce1)));
   if (real(p1)<0) p1 = -p1; end;

   p2=sqrt(-1i*(omega/D2)*(1 - (Ci2/Ce2)/(0 + 1i*omega*tau2*Ci2/Ce2)));
   if (real(p2)<0) p2 = -p2; end;

   exp_plus=exp(p1*d1); exp_minus=exp(-p1*d1);

   discrim = (-k1*p1+k2*p2-R_Kap*k1*k2*p1*p2)*k1*p1*exp_minus +...
        (k1*p1+k2*p2+R_Kap*k1*k2*p1*p2)*k1*p1*exp_plus;

   C11 = f_omega(index_omega)*(k1*p1+k2*p2+k2*p2*R_Kap*k1*p1)/ discrim;
   C12 = f_omega(index_omega)*(k1*p1-k2*p2+k2*p2*R_Kap*k1*p1)/ discrim;
   C21 = C11 + C12 - R_Kap * k1 * p1 * (C11 - C12);
    % Te in gold layer
    for index_z=1:N1-1
        z=-d1+(index_z-1)*delta_z1;
        z_show(index_z)=z;
        Te_omega(index_z,index_omega)=C11*exp(-p1*z)+C12*exp(p1*z);
    end
    % Te in cobalt layer
    for index_z=N1+1:N_total
        z=(index_z-N1)*delta_z2; z_show(index_z)=z;
        Te_omega(index_z,index_omega)=C21*exp(-p2*z);
    end
    % intermediate point between two materials
    Te_omega(N1,index_omega)=0.5*(Te_omega(N1-1,index_omega)+...
    Te_omega(N1+1,index_omega));
end

%========== Inverse Fourier transform for Te ==========%
N_pnts=length(time_temp);
T_e_total=zeros(N_pnts,N_total);          % matrix of Te(z, t)
T_i_total=zeros(N_pnts,N_total);          % matrix of Ti(z, t)
```

```
index_time = 0;
for idTime=time_temp
    index_time=index_time + 1;
    Te_final=zeros(1,N_total);Ti_final=zeros(1,N_total);
    for index_z=1:N_total
        int1=0;
        for index_omega=1:N_time
            omega=delta_omega*(index_omega-1)-pi/delta_t;
            int1=int1+exp(-1i*omega*idTime)*Te_omega(index_z,index_omega);
        end
        Te_final(index_z)=int1;
    end
    T_e_total(index_time,:)=Te_final ./ sqrt(N_time);
end
% we neglect the imaginary component
T_e_total=real(T_e_total);

%========== Calculation of the Ti ==========%
tau1_p=Ci1/g1*10^12;
tau2_p=Ci2/g2*10^12;

E1=exp(-time_temp/tau1_p);
E2=exp(-time_temp/tau2_p);
% lattice temperature in gold
for ii=1:N1-1
        buf(:,ii)=conv(T_e_total(:, ii)', E1) ./tau1_p;
end
% lattice temperature in cobalt
for ii=N1+1:N_total
        buf(:,ii)=conv(T_e_total(:,ii)', E2) ./tau2_p;
end
% intermediate point between cobalt and gold
buf(:,N1)=0.5*(buf(:,N1-1)+buf(:,N1+1));
T_i_total = buf(1: size(T_e_total, 1), :) .* delta_t;
T_i_total=real(T_i_total);

Te1_surf1=T_e_total(:,1);      % Te at air-metal interface
Te1_surf2=T_e_total(:,N1-1);   % Te at metal1-metal2 interface (in metal1)
Te2_surf2=T_e_total(:,N1+1);   % Te at metal1-metal2 interface (in metal2)

Ti1_surf1=T_i_total(:,1);      % Ti at air-metal1 interface
Ti1_surf2=T_i_total(:,N1-1);   % Ti at metal1-metal2 interface (in metal1)
```

```
Ti2_surf2=T_i_total(:,N1+1);  % Ti at metal1-metal2 interface (in metal2)

hfig = figure(2);
set(hfig, 'position', [0 0 600 450])
plot(time_show * 1e12,f_time.*max(Te1_surf1)/max(f_time),...
    time_temp* 1e12,Te1_surf1,time_temp* 1e12,Te1_surf2,...
    time_temp* 1e12,Te2_surf2)
legend('Laser pulse','T_{e,surface 1}^{Au}',...
'T_{e,surface 2}^{Au}','T_{e,surface 2}^{Co}','Fontsize', 14);
title('T_e at air-metal1 and metal1-metal2 interfaces');
xlabel('Delay time, ps','FontSize',16);
ylabel('Temperature, a. u.' , 'FontSize',16)
xlim([0 t_final * 1e12]);
box on;

hfig = figure(3);
set(hfig, 'position', [0 0 600 450])
plot(time_show* 1e12,f_time.*max(Ti2_surf2)/max(f_time),...
    time_temp* 1e12,Ti1_surf1,time_temp* 1e12,Ti1_surf2,...
    time_temp* 1e12,Ti2_surf2)
legend('Laser pulse','T_{i,surface 1}^{Au}','T_{i,surface 2}^{Au}',...
'T_{i,surface 2}^{Co}', 'Fontsize', 14);
title('T_i at air-metal1 and metal1-metal2 interfaces');
ylabel('Temperature, a. u.' , 'FontSize',16)
xlabel('Delay time, ps','FontSize',16);
xlim([0 t_final* 1e12]);
box on;

hfig = figure(4);
set(hfig, 'position', [0 0 600 450])
mesh((z_show + thicknessAu) * 1e9, time_temp * 1e12, T_e_total)
title('Evolution of the T_e(z, t)');
ylabel('Delay time, ps' , 'FontSize',16)
xlabel('Thickness, nm','FontSize',16);
xlim([0 (thicknessAu + thicknessCo) * 1e9])
view([0 -90])

hfig = figure(5);
set(hfig, 'position', [0 0 600 450])
mesh((z_show + thicknessAu) * 1e9, time_temp * 1e12, T_i_total)
title('Evolution of the T_i(z, t)');
ylabel('Delay time, ps' , 'FontSize',16)
xlabel('Thickness, nm','FontSize',16);
```

```
xlim([0 (thicknessAu + thicknessCo) * 1e9])
view([0 -90])
```

A.2 Strain propagation in multilayer : MATLAB script

```
clear all
close all
set(0,'Units', 'pixels', 'DefaultAxesFontSize',12,'DefaultAxesFontName'...
    ,'Helvetica','DefaultAxesFontWeight','normal'); % normal bold
% You may load your own strain profile here
% load('Strain.mat')
% [N_t,N_z]=size(StrainComsol);

%========== gold constants ==========%
c_sAu = 3.45;               % sound speed [nm/ps]
roAu = 19300;               % density [kg/m^3]

%========== cobalt constants ==========%
c_sCo = 6.3;                % sound speed [nm/ps]
roCo = 8900;                % density [kg/m^3]

%========== sapphire constants ==========%
c_sSapp = 11.3;             % sound speed [nm/ps]
roSapp = 4000;              % density [kg/m^3]

%========== Acoustic impedances ==========%
ZSapp = c_sSapp * roSapp;
ZCo = c_sCo * roCo;
ZAu = c_sAu * roAu;

%========== Transmission coefficients ==========%
TAuCo = 2 * ZAu / (ZCo + ZAu) * c_sAu/c_sCo;
TCoAu =  2 * ZCo / (ZCo + ZAu) * c_sCo/c_sAu;

TCoSapp =  2 * ZCo / (ZCo + ZSapp) * c_sCo/c_sSapp;
TSappCo = 2 * ZSapp / (ZCo + ZSapp) * c_sSapp/c_sCo;

%========== Reflection coefficients ==========%
RAuCo = (ZCo - ZAu) / (ZAu + ZCo);
RCoAu = -RAuCo;
```

```
RCoSapp = (ZSapp - ZCo) / (ZCo + ZSapp);

%========== parameters of the model ==========%
thicknessAu = 150;          % thickness of gold [nm]
thicknessCo = 30;           % thickness of cobalt [nm]
thicknessSapp = 100;        % thickness of sapphire [nm]

zetaAu = 180;               % heat diffusion in gold [nm]
zetaCo = 18;                % heat diffusion in cobalt [nm]
overheating = 13;           % overheating of the cobalt layer

dt = 0.1;                   % time step [ps]
tFinal = 300;               % final time [ps]
time = 0 : dt : tFinal;
N_prop = length(time);

%========== creation of the profiles ==========%
dAu = dt * c_sAu;                   % acoustic mesh in gold
dCo = dt * c_sCo;                   % acoustic mesh in cobalt
dSapp = dt * c_sSapp;

xAu = 0 : dAu : thicknessAu;        % space vector for gold
xCo = 0 : dCo : thicknessCo;        % space vector for cobalt
xSapp = 0 : dSapp : thicknessSapp; % space vector for sapphire
% total space vector
x = [xAu (xCo + xAu(end) + dCo) (xSapp + xCo(end) + xAu(end) + dSapp)];

NAu = length(xAu);                  % last point of gold
NCo = NAu + length(xCo);            % last point of cobalt
N_total = NCo + length(xSapp);      % total number of points

strainAu = exp(-xAu/zetaAu);
strainCo = exp(-xCo/zetaCo) * exp(-thicknessAu/zetaAu) * overheating;
strainSapp = zeros(1, length(xSapp));
% total strain vector
strain = [strainAu strainCo strainSapp];

% Plotting the strain initial distribution
hfig = figure(1);
set(hfig, 'position', [0 0 600 450])
plot(x, strain)
title('Initial strain distribution inside the gold/cobalt');
ylabel('Strain, a. u.' , 'FontSize',16)
```

```
xlabel('Thickness, nm','FontSize',16);
box on;

%========== propagation algorithm ==========%
strain_plus=zeros(N_prop,N_total);          % positive strain
strain_minus=zeros(N_prop,N_total);         % negative strain

% definition of the initial strain condition
strain_plus(1,:)=strain * 0.5;
strain_minus(1,:)=strain * 0.5;

%=== time cycle
 for jj=1:1:N_prop - 1
        %==== cycle for propagation in gold
        for ii=1:1:NAu - 1
            strain_plus(jj+1,ii+1)=strain_plus(jj,ii);
            strain_minus(jj+1,ii)=strain_minus(jj,ii+1);
        end
        %==== cycle for propagation in cobalt
        for ii=NAu+1:1:NCo - 1
            strain_plus(jj+1,ii+1)=strain_plus(jj,ii);
            strain_minus(jj+1,ii)=strain_minus(jj,ii+1);
        end
       %==== cycle for propagation in sapphire
        for ii = NCo + 1 : 1 : N_total-1
             strain_plus(jj+1,ii+1)=strain_plus(jj,ii);
             strain_minus(jj+1,ii)=strain_minus(jj,ii+1);
        end

    % Transmission of strain from gold into cobalt
    strain_plus(jj+1, NAu+1) = TAuCo*strain_plus(jj,NAu)+...
    RCoAu * strain_minus(jj,NAu+1);
    % Transmission of strain from cobalt into gold
    strain_minus(jj+1, NAu) = TCoAu * strain_minus(jj,NAu+1)+...
    RAuCo * strain_plus(jj,NAu);
    % Reflection of strain at cobalt/sapphire interface with
    % propagation into cobalt layer
    strain_minus(jj+1, NCo) = RCoSapp * strain_plus(jj, NCo);
    % Reflection of strain at  free interface towards cobalt
    strain_plus(jj+1,1 ) = -strain_minus(jj,1);
    % Transmision of the strain from cobalt layer into sapphire
    strain_plus(jj + 1, NCo + 1) = TCoSapp *...
    strain_plus(jj, NCo);
```

```
 end
%=== Total strain
strainTotal=(strain_plus+strain_minus);

% Plotting the strain at the cobalt/sapphire interface
hfig = figure(3);
set(hfig, 'position', [0 0 600 450])
plot(time, -strainTotal(:, NCo - 1))
title('Strain at the cobalt/sapphire interface');
ylabel('Strain, a. u.' , 'FontSize',16)
xlabel('Delay time, ps','FontSize',16);
box on;

% Plotting the 2D distribution of the strain
hfig = figure(4);
set(hfig, 'position', [0 0 600 450])
mesh(x, time, strainTotal)
title('Evolution of the strain in gold/cobal/sapphire structure');
ylabel('Delay time, ps' , 'FontSize',16)
xlabel('Thickness, nm','FontSize',16);
xlim([0 x(end)])
view([90 -90])
```

B

Lattice vibrations, Phonons and Electrons

The heat flow problems are very important in the domain of electronics for engineers who design solar panels, computer chips or try to build thermoelectric devices[34,35]. The heat flow in the solids can be explained similarly to the flow of heat carriers (phonons and electrons). To be able to control thermal transport it is necessary to understand the mechanisms of interaction for each carrier. Thus it will be possible to build, for example thermoelectric devices (which are based on material that conduct electricity and block phonons) and design better heat removal allowing manufacturing of faster chips for computers.

Therefore we start from lattice vibration theory then discuss phonons and their thermal behavior, finally we end with properties of electrons that contribute considerably in thermal transport in metals.

B.1 Lattice vibrations

Lattice dynamics approximate motion of atoms in solids and liquids by analogy with classic mechanics. However even such simplified consideration allows to estimate what are the possible frequencies of oscillation of atoms in material called the dispersion relation. Thus dispersion relation dictates how varies the angular frequency of elastic wave ω as a function of momentum k. Moreover, dispersion relation defines not only acoustic properties of material but also thermal behavior as it will be shown later.

B.1.1 Dynamics of linear lattice

Modern theory of solids assumes that the atoms in solids undergoes the continuous thermal agitation. Assuming that the interaction between the atoms is elastic, thermal disturbances cause the displacement that propagates as elastic waves. Let us consider the simplest model, i.e. one dimensional chain of identical atoms as shown in Fig. B.1. In analogy with mechanics

we can assume, that each atom has a mass M and bonded with another atoms by springs with a stiffness coefficient β (also called inter-atomic force constant).

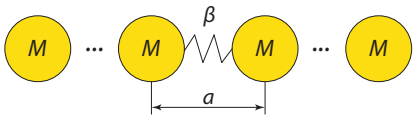

Figure B.1: Infinite mono-atomic chain of gold atoms in 1D used for calculation of the dispersion relation; β is the inter-atomic force constant; M is the mass of the gold atom; a is the lattice spacing parameter.

After solving the equation of motion that accounts the influence of the nearest neighbors we can express the relation between the wave-vector k and angular frequency w of oscillating modes

$$w = \left(\frac{4\beta}{M}\right)^{1/2} \left|\sin\left(\frac{ka}{2}\right)\right|, \tag{B.1}$$

where M is the mass of the atom and wave-vector k is related to its wavelength λ by $k = 2\pi/\lambda$. Such chain of identical atoms can be treated as continuum for wavelengths that are much bigger than the atomic spacing distance a. Therefore the dispersion relation can be approximated by a linear function $w = c_0 k$ (red dashed line in Fig.B.2). In this linear relation c_0 is the speed of a propagating wave. Such simplified dispersion relation is characterized by equal phase ω/k and group velocity $\partial\omega/\partial k$.

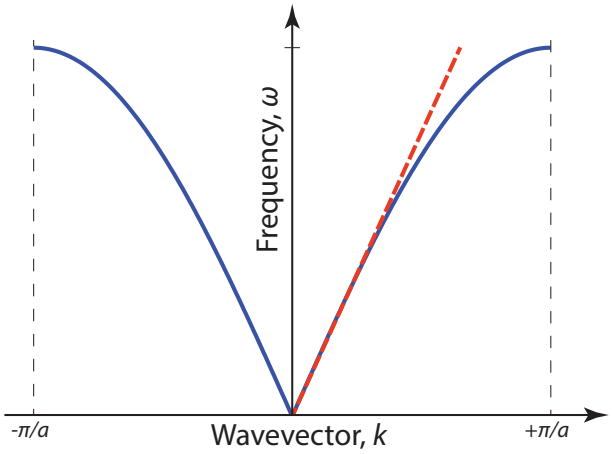

Figure B.2: Dispersion relation for a mono-atomic linear lattice within the first Brillouin zone (blue solid line); linear approximation of dispersion relation (red dashed line).

The dispersive behavior of overall crystalline material can be described by considering only one primitive cell or Wigner-Seitz cell. Therefore, uniquely defined primitive cell that by translation can reproduce the structure of solid is called the first Brillouin zone. An example of the dispersion relation in k-space for first Brillouin zone is shown in Fig. B.2. However the structure of allowed modes can be much more complicated and can consist of acoustic and optic branches.

But we will focus only on acoustic modes that define the type of the displacement of atoms from their equilibrium position. Basically, there are two modes : longitudinal (L) and transverse (T). First, the longitudinal mode is characterized by displacement of particles along the line of the direction of propagating wave (see Fig. B.3). In contrast, the transverse mode is identified when the propagating wave is normal to the displacement of atoms (see Fig. B.4).

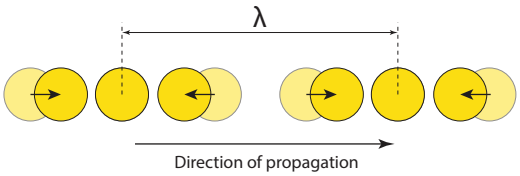

Figure B.3: Trajectory of the motion of the progressive longitudinal wave with wavelength λ.

Typically, T-waves have smaller value of both wavelength and sound velocity for the same frequency and sometimes can be referred to shear waves. In addition there are surface or Rayleigh waves. Such waves represent the oscillating motion of particles that travels along the surface to a depth of one wavelength inside the bulk. They have similar velocities and wavelengths as shear waves. However, in further chapters we will focus only on longitudinal acoustic waves.

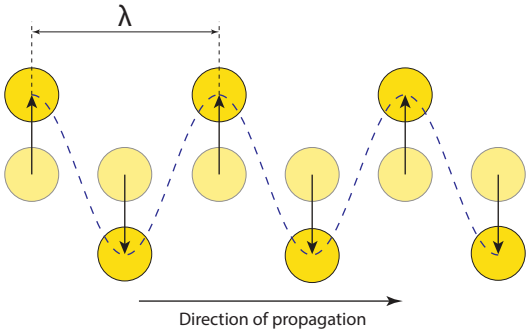

Figure B.4: Trajectory of the motion of the transverse standing wave, showing the out-of-plane motion with wavelength λ.

B.1.2 Dispersion Relation: Extended Model

In reality, in cubic crystals the dispersion relation is much more sophisticated. As an illustration, we can consider a slowness surface of fcc nickel shown in Fig. B.5. Slowness surface shows the value of the wave-vector k in the chosen direction resulting. It is easy to see that there are some privileged directions where acoustic waves can propagate with higher values of speed because length of the wave-vector is in direct relation with the speed of sound. These directions corresponds to zones where the forces slowing the propagation of phonons are minimal.

More sophisticated description of the mono-atomic lattice vibrations for a waves traveling along all the symmetry direction could be examined through Sharma-Joshi[81] and Krebs[82]

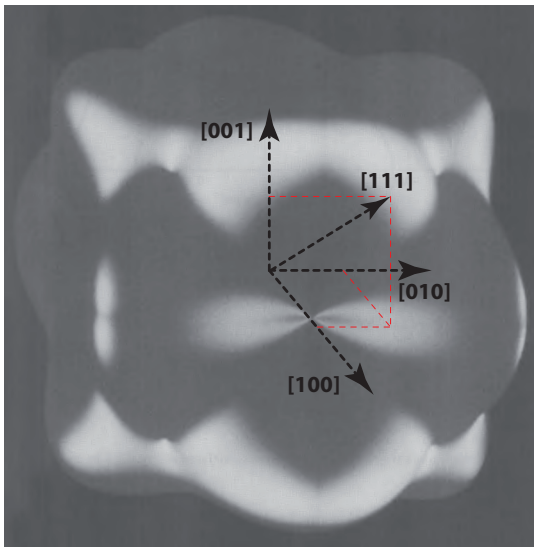

Figure B.5: Phase-surface of the Ni that reveals complex dispersion in fcc lattice with reference crystallographic directions [100], [010] and [001].

phenomenological model. This model describes the lattice dynamics for cubic metals, especially the Noble metals like gold, silver and copper. Characteristic equation that determines the angular frequencies w of the normal modes of vibration can be written through the secular equation

$$|D_{ij}(\boldsymbol{k}) - Mw^2 I| = 0, \tag{B.2}$$

where M is the mass of the ion, I is the unit matrix of third order, and $D_{ij}(k)$ is the dynamic matrix responsible for three different types of interaction resulting in

$$D_{ij}(\boldsymbol{k}) = D^r_{ij}(\boldsymbol{k}) + D^a_{ij}(\boldsymbol{k}) + D^e_{ij}(\boldsymbol{k}), \tag{B.3}$$

where the term $D^r_{ij}(k)$ describes the radial interaction between the ions, $D^a_{ij}(k)$ is the angular interaction between the nearest neighbor ions only, and $D^e_{ij}(k)$ is the interaction between electrons. All these terms could be decomposed into two groups depending on the combination of coefficients i and j so that for $i = j$ we have

$$\begin{aligned} D^r_{ij}(\boldsymbol{k}) &= 2\alpha_1[2 - c_1(c_2 + c_3)] + 4\alpha_2 s_1^2 \\ D^a_{ij}(\boldsymbol{k}) &= 2\alpha'[4 - c_1(c_2 + c_3)] - 2c_2c_3 \\ D^e_{ij}(\boldsymbol{k}) &= a^3\pi^2 K_e k_1^2 G^2(2\pi k\gamma_0), \end{aligned} \tag{B.4}$$

and for $i \neq j$

$$\begin{aligned} D^r_{ij}(\boldsymbol{k}) &= 2\alpha_1 s_1 s_2 \\ D^a_{ij}(\boldsymbol{k}) &= -2\alpha' s_1 s_2 \\ D^e_{ij}(\boldsymbol{k}) &= a^3\pi^2 K_e k_1 k_2^2 G^2(2\pi k\gamma_0), \end{aligned} \tag{B.5}$$

where

$$c_i = \cos(\pi a k_i) \qquad s_i = \sin(\pi a k_i) \tag{B.6}$$

and

$$G(x) = 3\left(\frac{\sin x - x\cos x}{x^3}\right), \quad |\boldsymbol{k}| = \frac{1}{\lambda}, \tag{B.7}$$

where k_i is the ith Cartesian component of the wave vector $\boldsymbol{k}$, λ is the wavelength, a is the semi-lattice parameter, γ_0 is the ionic radius of the Wigner-Seitz sphere. The parameters α_1 and α_2 are the radial force constants for the first- and second-neighbor interactions respectively and α' is the angular force constant for the nearest-neighbor interaction, and the factor K_e arises from the electron-ion interaction. These parameters can be related to the three elastic constants of a cubic metal through

$$\begin{aligned} aC_{11} &= 2\alpha_1 + 4\alpha_2 + 2\alpha' + aK_e \\ aC_{12} &= \alpha_1 - 5\alpha' + aK_e \\ aC_{44} &= \alpha_1 + 3\alpha'. \end{aligned} \tag{B.8}$$

All the connected to this model constants and calculated values are presented in Tables B.1 and B.2

Table B.1: Tabulated elastic constants[83]

Material	C_{11}	C_{12}	C_{44}	a
	$10^{10}\frac{N}{m^2}$	$10^{10}\frac{N}{m^2}$	$10^{10}\frac{N}{m^2}$	10^{-12}m
Gold	19.23	16.31	4.20	407

Table B.2: Calculated elastic parameters[84]

Material	α_1	α_2	α'	K_e	γ_0
	$1\frac{N}{m^2}$	$1\frac{N}{m^2}$	$1\frac{N}{m^2}$	$10^{10}\frac{N}{m^2}$	10^{-9}m
Gold	33.34	4.109	-5.413	1.47	1.37

The result of simulation for three symmetry directions [100], [110] and the orientation that corresponds to the direction of growth of all our gold samples [111] is shown in Fig. B.6.

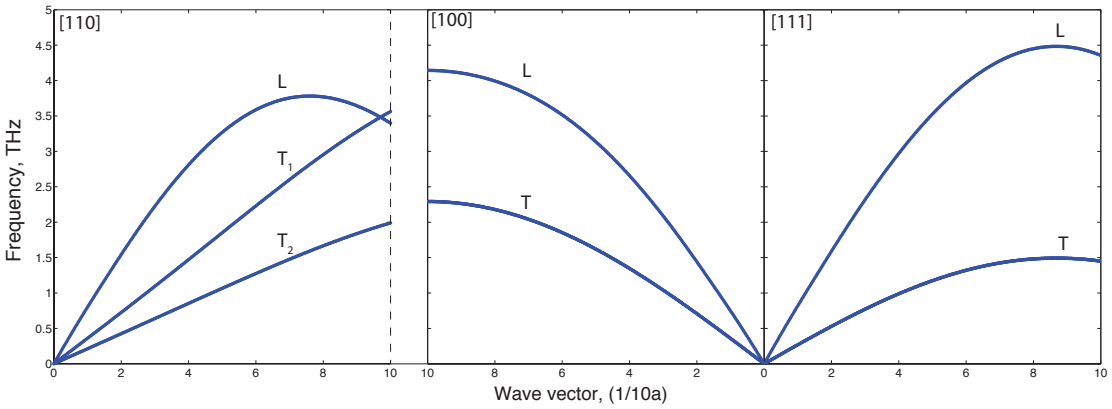

Figure B.6: Calculated dispersion relation for gold at room temperature, k is in units of (1/10a).

Anisotropy of gold will look very similar to nickel because they both have fcc crystal structure. We can evaluate the spatial distribution of the wave-vector variation in sample growth direction [111]. For this reason slowness surface was calculated for gold of 1.5x1.5 μm dimensions and it is shown in Fig. B.7. Observed wave-vector anisotropy distribution should remarkably change the wavefront of propagating plane wave leading to significant distortions. Thus wave propagating in the gold [111] will experience noticeable change of the wavefront due to 10% variation of wavevector k. The shape of observed anisotropy that present three regions of higher values of wavevector is typical for third-order symmetry direction [111].

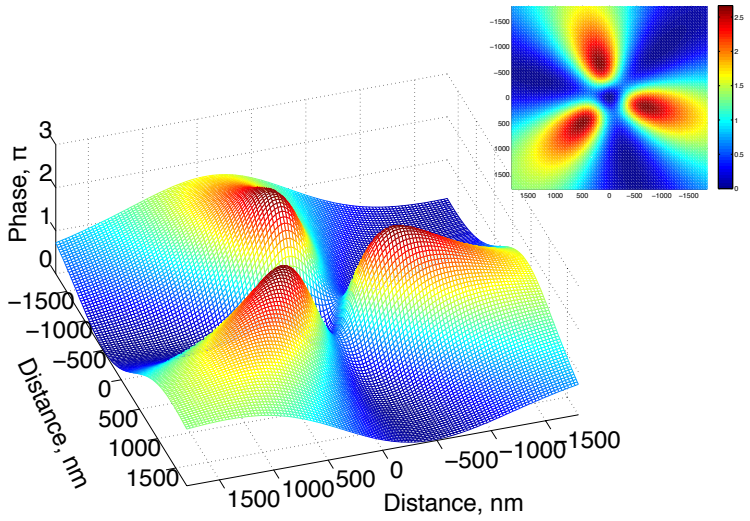

Figure B.7: Calculated slowness surface for gold [111] at room temperature shows three privileged regions in which acoustic speed can reach up to 10% bigger values of k; Such shape of anisotropy is dictated by third order symmetry direction [111].

Such remarkable anisotropy should be taken into account during design of nanodevices like proposed concept of the Fresnel lens for focusing of THz phonons presented in Appendix B.2.2.

B.2 Phonons

In further discussion we will use the quantum notion of the lattice vibration called phonon. Phonon is a boson and follows the Bose-Einstein statistics in thermal equilibrium, thus two or more identical phonons can be on the same quantum state.

Phonon has energy $E = \hbar\omega$ and acts as if it has a momentum $\vec{p} = \hbar\vec{q}$ (but do not carry momentum itself). Phonon with wave-vector $\vec{q}$ can combine with a system of wave-vector $\vec{k}$ leading to creation of a new phonon with the wave-vector $\vec{q'}$. During this process energy and crystal momentum are conserved so that

$$\vec{q} + \vec{k} = \vec{q'} + \vec{G}, \tag{B.9}$$

where $\hbar\vec{G}$ represents the momentum imparted to the crystal as a whole. It is possible also for a phonon $\vec{q}$ to decay into two phonons $\vec{q'}$ and $\vec{q''}$

$$\vec{q} = \vec{q'} + \vec{q''} + \vec{G}. \tag{B.10}$$

There are two types of scattering dominating at different temperature ranges. For a low-temperature regime, in general, the scattering of phonons is taking place without the change of crystal momentum, which means that $\vec{G} = 0$ and the process is called to be normal. At high temperatures the probability of a scattering with a change of the wave-vector is high, thus to preserve the conservation of crystal momentum reciprocal wave-vector $\vec{G} \neq 0$ is introduced, this is the Umklapp process. Interaction of the phonons determine the thermal properties of material which will be covered afterward.

B.2.1 Thermal properties of phonons

To describe thermal properties of phonons it is not enough to have only dispersion relation. In order to take into account the resultant effect of the thermal lattice vibrations on the ultrasonic acoustic wave it is necessary to know also the density of vibrational states as a function of frequency.

The density of states (DOS) is a continuous function that shows what is the probability of the state to be occupied by a phonon. In general, the topological properties of the system has a major impact on the distribution of the DOS. Calculation of the DOS using quantum mechanics is not an easy task, but there is a Debye approximation that can estimate the thermal heat capacity.

In the Debye approximation solid is treated as a continuum in which speed of propagation does not depend on the frequency (linear approximation of dispersion relation) with a limited number of normal modes equal to the number of degrees of freedom. Suppose that the crystal contains $N/3$ atoms per unit volume, and each atom has three degrees of freedom, this leads to N normal modes. In such approximation the cut-off frequency ω_D is introduced

representing the maximum possible frequencies for the medium (bounded on the inter-atomic distance a). So far, the number of modes $D_(\omega)$ in Debye approximation is defined through the relation

$$\int_0^{\omega_D} D(\omega)d\omega = N. \tag{B.11}$$

In the case of solid continuum the expression for a density of states $D(\omega)$ has the following form[85]

$$D(\omega) = \frac{\omega^2}{2\pi^2}\left(\frac{1}{c_L^3} + \frac{2}{c_T^3}\right), \tag{B.12}$$

where two velocities are presented, such as velocity of longitudinal wave c_L and velocity of transverse wave c_T. Distribution of the DOS for the Debye model is shown in Fig. B.8(a) and Fig. B.8(b) is devoted to illustrate DOS calculated by more exact lattice theory[85]. The cut-off frequency could be obtained from Eq. (B.11) using expression (B.12)

$$\omega_D = \left[6\pi^2 N\left(\frac{1}{c_L^3} + \frac{2}{c_T^3}\right)^{-1}\right]^{1/3}. \tag{B.13}$$

In real anisotropic crystals velocities c_L and c_T are direction dependent. That is why average velocity (or effective velocity) c_0 over the direction of propagation is frequently used and it is defined as follows

$$\frac{3}{c_0^3} = \frac{1}{c_L^3} + \frac{2}{c_T^3}. \tag{B.14}$$

From this model one important parameter could be deduced, such as the Debye temperature Θ_D. This is the temperature of a crystal's highest normal mode of vibration, or the highest temperature that can be achieved due to a single normal vibration which is defined by

$$\Theta_D = \frac{\hbar\omega_D}{k_B}, \tag{B.15}$$

where k_B is the Boltzmann's constant.

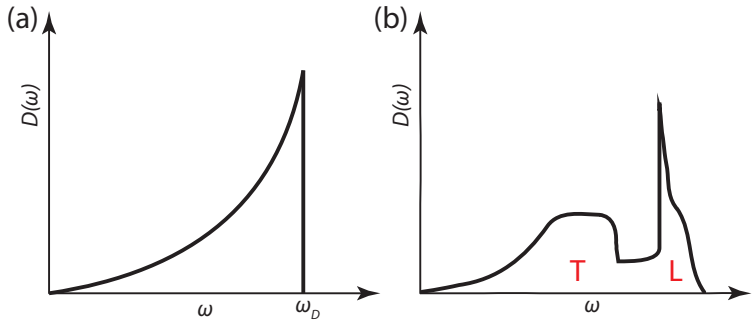

Figure B.8: Density of phonon states in gold calculated by (a) Debye approximation and (b) approximation of the quantum mechanical calculations. In the Debye model all the states before ω_D are available, but in reality the crystal structure remains some states in between L and T regions to be low-populated, that can be seen in (b) where transverse (low-frequency) and longitudinal (high-frequency) modes are splitted.

The Debye temperature for gold is $\Theta_D = 170K$[86]. Having such low value of the Debye temperature means that at 170 K all the phonons in gold are already excited, which results in less stiff properties of gold. For example, the diamond is one of the most hard materials has the Debye temperature equal to 2200 K.

In thermal transport, one of the most important parameters, which is responsible for the amount of temperature change under heating or cooling of a medium is a heat capacity C_V. The empirical expression that gives evolution of heat capacity as a function of temperature

$$C_V = \gamma T + \beta T^3, \tag{B.16}$$

where the first term is associated with contribution of electrons and the second one is related to phonons; γ and β are constants.

Heat capacity could be deduced from the DOS by derivation of the thermal energy U with respect to the temperature T at constant volume V

$$C_V = \left(\frac{\partial U}{\partial T}\right)_V, \tag{B.17}$$

where the total thermal energy is given by

$$U = \int_0^{\omega_D} \hbar\omega D(\omega) n(\omega) d\omega, \tag{B.18}$$

where $n(\omega)$ is the number of thermally excited phonons given by

$$n = \int_0^{\omega_D} D(\omega) n(\omega) d\omega. \tag{B.19}$$

After substitution of all these expressions and derivation of thermal energy (in assumption

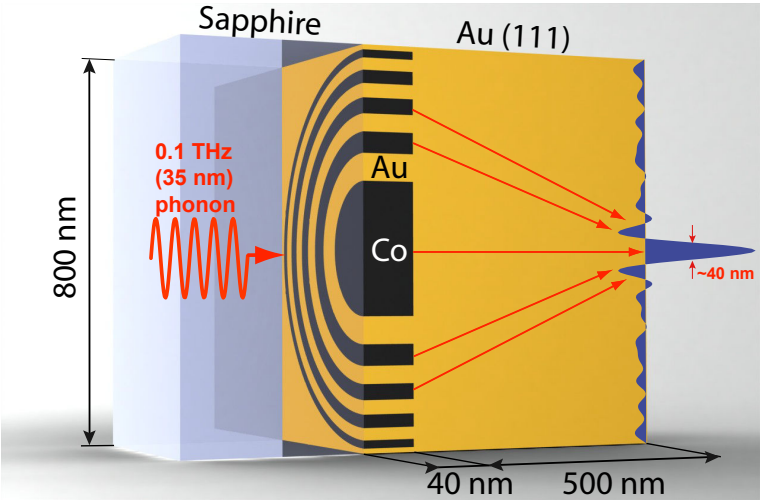

Figure B.9: Concept of the Fresnel lens for focusing of THz phonons into sub 100 nm spot after propagation in gold.

of low temperature regime) we can obtain the T^3 phononic component of heat capacity

$$C_V = 6\pi^4 N k_B \left(\frac{T}{\Theta_D}\right)^3 . \tag{B.20}$$

However this expression fails to describe the high temperature regime of evolution of the heat capacity.

B.2.2 Fresnel lens for focusing of THz phonons

Efficiency of sound focusing is directly proportional to the wavelength of the wave, therefore to be able to focus phonons into sub 100 nm spot, phonons in THz range should be used. Damping of such phonons in gazes and liquids is very high and only in solids they can undergo μm distances[87] that is why solids should be used for focusing THz phonons.

The model of such lens presented in Fig. B.9 consists of a thin cobalt layer (40 nm) sandwiched between a dielectric substrate and a crystalline [111] layer of gold (500 nm, equal to the focal length). A sequence of five rings (with the outer radius of 400 nm) can be etched in cobalt by electron lithography before sputtering the gold layer on top. A good acoustic impedance matching between gold, cobalt and sapphire suggests that acoustic reflections at these interfaces can be neglected and the acoustic Fresnel lens provides spatial phase modulation. The geometrical path difference of acoustic waves coming to the focal spot from the two adjacent cobalt zones equal to π, leading to constructive interference of sound waves at focal plane. Distribution of acoustic strain in the focal plane calculated using classical diffraction theory should produce concentric rings as shown in Fig. B.10 with a central peak of about 40 nm full width half maximum (FWHM). Such result looks very similar to the diffraction pattern of light passing through the Fresnel zone plate because in both cases plane waves are considered to propagate in isotropic medium.

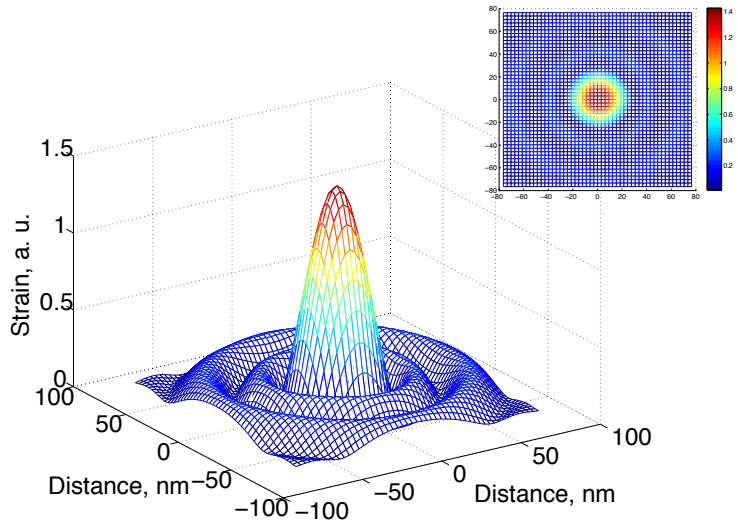

Figure B.10: Calculated distribution of strain formed by the Fresnel lens in the case of isotropic medium of propagation in the focal plane at 500 nm with FWHM 40 nm of central spot.

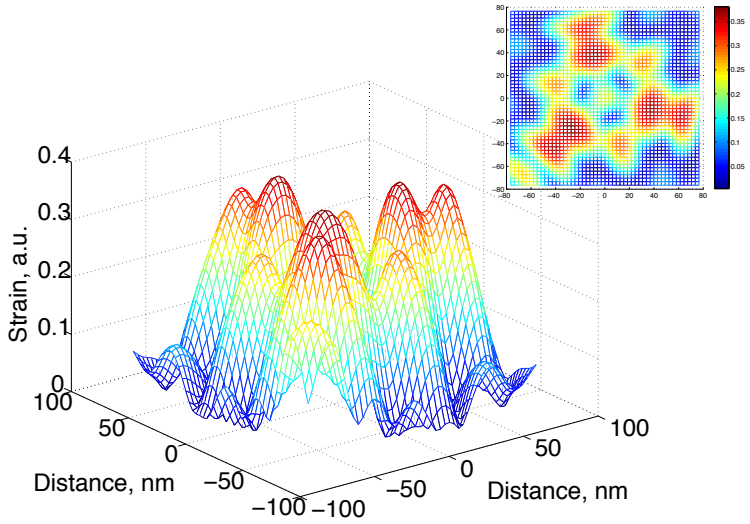

Figure B.11: Calculated distribution of strain formed by the Fresnel lens in the focal plane at 500 nm in the case of propagation of strain in anisotropic gold with orientation [111] showing low efficiency of focusing.

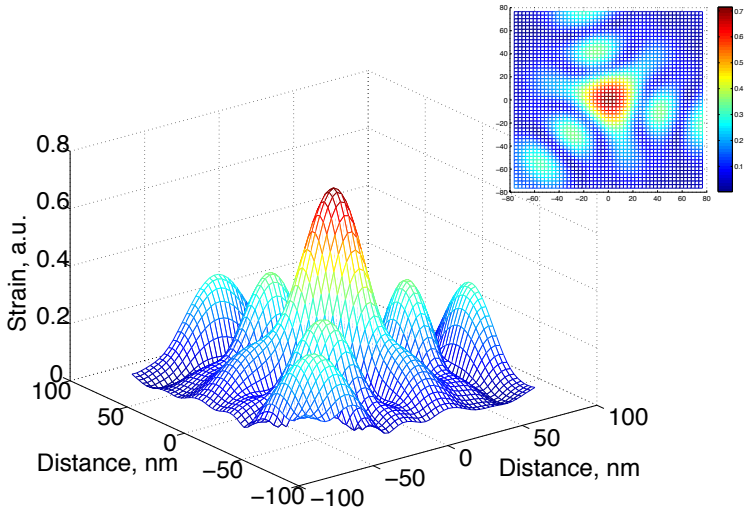

Figure B.12: Calculated distribution of strain formed by the Fresnel lens in the case of anisotropic gold with orientation [111] at 700 nm from the lens forming a new focus.

More interesting will be the case where we will take into account the dispersion for every wave propagating in anisotropic gold. The result of combining diffraction theory with complex lattice dynamics model discussed earlier is shown in Fig. B.11. Distribution of strain is significantly distorted by the presence of 10% anisotropy in gold. A single central peak evolves into complex shape where strain is redistributed all over the zone of dimension 100 by 100 nm. It is evident that efficiency of focusing for that case is very low.

Surprisingly, it was found that the distribution of strain at the plane situated 200 nm away from the focal plane at 700 nm converges to higher efficiency of focusing as it is shown in Fig B.12 where we can distinguish anew single peak similar to isotropic. FWHM of central focal spot is of the same value 40 nm that for the isotropic case but with three satellites produced by gold third-order symmetry direction [111].

Simulations shows, that for devices designed to work at the nanoscale the effect of 10% anisotropy can distort very pronounceable desirable strain distribution leading to less efficient operation of the device.

Operating dimensions of the focal spot are directly proportional to the sizes of the Fresnel lenses[88]. As well as higher frequency phonons can not propagate in water and gas substances that is why to be able to focus in sub-100 nm spot concept of Fresnel lens composed of cobalt nanodisks followed by gold was proposed. Such pair of materials are proposed because of their phase-match properties leading to only 10% reflections on the interfaces.

However, to fabricate such lens with more than 5 rings is a difficult technological task because thickness of the rings after fifth is about 10 nm. But to create such structure with 3-5 rings is a feasible task for modern production capability.

An open question for this work is an experimental installation allowing to prove the concept of the working Fresnel lens for focusing THz phonons. In case if it can be proven the new horizons of the acoustic microscopy could be achieved with plenty applications in the domain of biophysics and medicine by operation with small biological samples, cancer tissues etc.

B.3 Electrons

Electron is a subatomic particle that have a negative elementary charge e^- and angular momentum m_s referred as spin. Since electron is the fermion it has half-integer spin and follows Fermi-Dirac statistics. According to Pauli principle electrons have intrinsic property that restricts for two identical electrons to occupy the same quantum state simultaneously. In further discussion we will review the behavior of electrons on the basis of free electron model and afterwards we will examine the mechanism of interaction of light with electrons in metals.

B.3.1 Free Electrons in Metals

There are different approaches to describe the electronic properties but we use simple "free electron gas" or Fermi gas. Such model has several assumptions. First assumption concerns valence electrons that supposed to be completely detached from their ions forming the electron gas. Second assumption suppose absence of the electron-electron and electron-ion interactions (ideal gas approximation). And the last assumption implies that electrons could not leave the boundaries of the metal. To find the allowed states for electrons boundary conditions are applied to the single-particle wave function. As a result, after solving the Schrödinger equation we can find that allowed states form a cubic array in k-space with a cube side $2\pi L$, where L is the dimension of the sample. Energy that corresponds to each state is equal to

$$E = \frac{\hbar^2}{2m}(k_x^2 + k_y^2 + k_z^2), \tag{B.21}$$

where $k_x = 2\pi n_x/L$, $k_y = 2\pi n_y/L$, $k_z = 2\pi n_z/L$, n_x, n_y, n_z are integral quantum numbers, m is the mass of electron and $\hbar$ is the reduced Planck constant or Dirac constant. With respect to the Pauli principle, each electron have a unique set of n_x, n_y, n_z and m_s. In honor of Italian physicist Enrico Fermi in solid state physics and theory of free electrons there are three important characteristics of metals : Fermi surface, Fermi energy and Fermi velocity. First, the Fermi surface corresponds to a sphere of radius k_f that contains all electrons occupying the lowest states in reciprocal space at absolute zero temperature. The states above the Fermi surface are supposed to be empty. Furthermore, the Fermi energy E_f is the energy of electron that occupy states at the Fermi surface and is given by

$$E_f = \frac{h^2 k_f^2}{2m}, \tag{B.22}$$

where h is the Planck constant. Fermi energy of gold is $E_f^{Au} = 5.53\text{eV}$[89]. The excited electrons from the Fermi surface are propagating at the Fermi velocity which is given by

$$v_F = \sqrt{\frac{2E_f}{m}} = \frac{hk_f}{m}. \tag{B.23}$$

Typical value of the Fermi velocity is a value of order of 10^6[m/sec], for gold it is $v_F^{Au} = 1.4 \cdot 10^6\text{m/s}$.

As it was mentioned before, electrons are characterized by Fermi-Dirac statistics so that at temperature T, the probability that a state with energy E is occupied by an electron is given by the Fermi-Dirac distribution function,

$$f(E) = \frac{1}{e^{(E-E_f)/k_BT} + 1}, \tag{B.24}$$

where k_B is the Boltzman's constant. Different distributions of electrons along the levels of energy for various temperatures are illustrated in Fig. B.13. At $T = 0$ K all the states above Fermi energy are filled and with a rise of the temperature more and more electrons are redistributed among the states corresponding to higher energies.

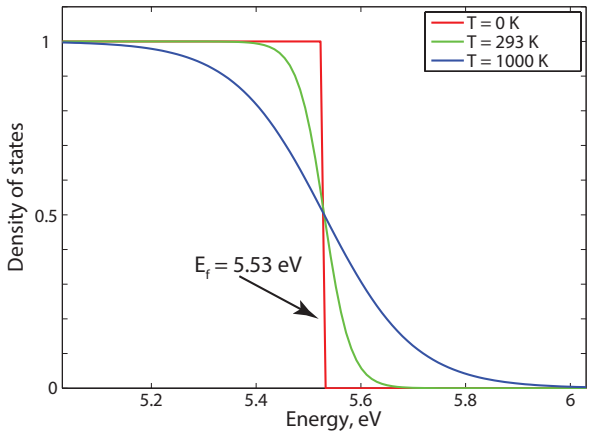

Figure B.13: Example of the Fermi-Dirac distribution for gold for three temperatures $T = 0$ K, 293 K and 1000 K showing the migration of the electrons towards higher energy states when the temperature of metal is increased.

At low temperatures the heat capacity is determined by the density of electronic states n and depends linearly from temperature in contrast to phononic cubic T^3 dependence

$$C_V = \frac{\pi}{3} k_B^2 \left(\frac{dn}{dE}\right) T. \tag{B.25}$$

The applicability of the model of free electrons is in good conformity only for alkali metals. To be able to obtain more useful and realistic predictions of the behavior of electrons in metals, the interactions of electrons with the ions of the lattice should be taken into account. In that case the electrons are assumed to exist in the periodic potential created by the positive

ions in the lattice, thus they are no longer absolutely free. That is why this model is called nearly-free electron gas. In this way it is possible to predict discontinuity of the energy, thus leading to band structure of energy levels with forbidden gaps.

An example of extended zone scheme for several Brillouin zones for free electron gas (black dashed line) and for nearly-free electron gas (blue solid line) is shown in Fig. B.14. The forbidden gaps presented for nearly-free gas are regions of energy states restricted for occupation. These band gaps occur on the boundaries of the Brillouin zones.

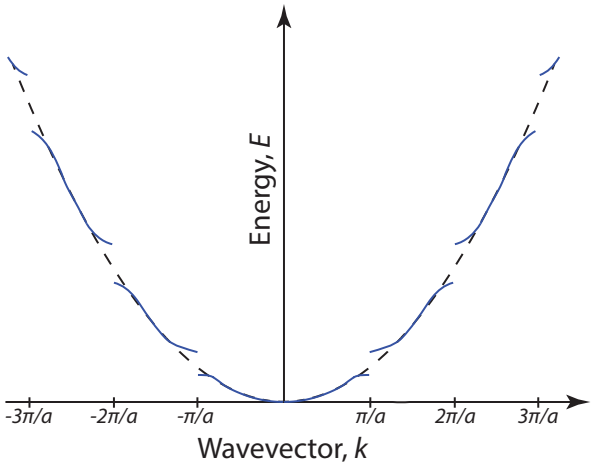

Figure B.14: Free-electron band structure (dashed line) and band structure of electron in the periodic potential (solid line)

However, there is another way to represent the band structure, such as more convenient reduced-zone scheme that is presented in Fig.B.15. The reduced-zone scheme represents the band structure from all the Brillouin zones folded over in the first zone. Such approach to represent electronic structure is usually the one most often used.

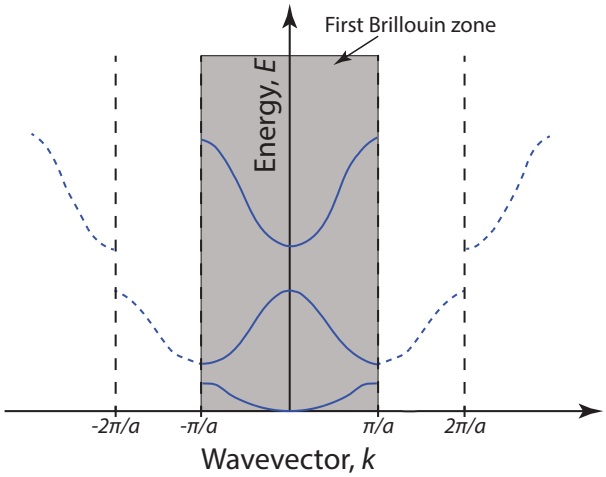

Figure B.15: Reduced-zone scheme showing the effect of translation of all the wave-vectors into first Brillouin zone represent much clear the band gaps in material.

C

Femtosecond imaging of nonlinear acoustics in gold : publication

Femtosecond imaging of nonlinear acoustics in gold

Thomas Pezeril,[1,*] Christoph Klieber,[1] Viktor Shalagatskyi,[1] Gwenaelle Vaudel,[1] Vasily Temnov,[1] Oliver G. Schmidt,[2,3] and Denys Makarov[2]

[1] *Institut Molécules et Matériaux du Mans, UMR CNRS 6283, Université du Maine, 72085 Le Mans, France*

[2] *Institute for Integrative Nanosciences, IFW Dresden, 01069 Dresden, Germany*

[3] *Material Systems for Nanoelectronics, Chemnitz University of Technology, 09107 Chemnitz, Germany*

[*] *thomas.pezeril@univ-lemans.fr*

http://perso.univ-lemans.fr/~tpezeril

Abstract: We have developed a high-sensitivity, low-noise femtosecond imaging technique based on pump-probe time-resolved measurements with a standard CCD camera. The approach used in the experiment is based on lock-in acquisitions of images generated by a femtosecond laser probe synchronized to modulation of a femtosecond laser pump at the same rate. This technique allows time-resolved imaging of laser-excited phenomena with femtosecond time resolution. We illustrate the technique by time-resolved imaging of the nonlinear reshaping of a laser-excited picosecond acoustic pulse after propagation through a thin gold layer. Image analysis reveals the direct 2D visualization of the nonlinear acoustic propagation of the picosecond acoustic pulse. Many ultrafast pump-probe investigations can profit from this technique because of the wealth of information it provides over a typical single diode and lock-in amplifier setup, for example it can be used to image ultrasonic echoes in biological samples.

OCIS codes: (320.0320) Ultrafast optics; (100.0118) Imaging ultrafast phenomena; (110.7170) Ultrasound.

References and links

1. T. Pezeril, G. Saini, D. Veysset, S. Kooi, P. Fidkowski, R. Radovitzky, and K. A. Nelson, "Direct visualization of laser-driven focusing shock waves," Phys. Rev. Lett. **106**(4), 214503 (2011).
2. C. A. Werley, S. M. Teo, B. K. Ofori-Okai, P. Sivarajah, and K. A. Nelson, "High-resolution, low-noise imaging in THz polaritonics," IEEE Trans. Terahertz Sci. Technol. **3**, 239–247 (2013).
3. C. Thomsen, H. T. Grahn, H. J. Maris, and J. Tauc, "Surface generation and detection of phonons by picosecond light pulses," Phys. Rev. B **34**, 4129–4138 (1986).
4. O. B. Wright and K. Kawashima, "Coherent phonon detection from ultrafast surface vibrations," Phys. Rev. Lett. **69**, 1668–1671 (1992).
5. T. Saito, O. Matsuda, and O. B. Wright, "Picosecond acoustic phonon pulse generation in nickel and chromium," Phys. Rev. B **67**(7), 205421 (2003).
6. Y. Sugawara, O. B. Wright, O. Matsuda, M. Takigahira, Y. Tanaka, S. Tamura, and V. E. Gusev, "Watching ripples on crystals," Phys. Rev. Lett. **88**(4), 185504 (2002).
7. K.-H. Lin, C.-T. Yu, S.-Z. Sun, H.-P. Chen, C.-C. Pan, J.-I. Chyi, S.-W. Huang, P.-C. Li, and C.-K. Sun, "Two-dimensional nanoultrasonic imaging by using acoustic nanowaves," Appl. Phys. Lett. **89**(3), 043106 (2006).

#201826 - $15.00 USD Received 29 Nov 2013; revised 10 Jan 2014; accepted 11 Jan 2014; published 20 Feb 2014

8. K.-H. Lin, C.-M. Lai, C.-C. Pan, J.-I. Chyi, J.-W. Shi, S.-Z. Sun, C.-F. Chang, and C.-K. Sun, "Spatial manipulation of nanoacoustic waves with nanoscale spot sizes," Nat. Nanotechnol. **2**, 704–708 (2007).
9. M. Tomoda, O. Matsuda, O. B. Wright, and R. L. Voti, "Tomographic reconstruction of picosecond acoustic strain propagation," Appl. Phys. Lett. **90**(3), 041114 (2007).
10. T. Dehoux, O. B. Wright, and R. Li Voti, "Picosecond time scale imaging of mechanical contacts," Ultrasonics **50**, 197–201 (2010).
11. M. Hettich, K. Jacob, O. Ristow, C. He, J. Mayer, M. Schubert, V. Gusev, A. Bruchhausen, and T. Dekorsy, "Imaging of a patterned and buried molecular layer by coherent acoustic phonon spectroscopy," Appl. Phys. Lett. **101**(4), 191606 (2012).
12. B. C. Daly, N. C. R. Holme, T. Buma, C. Branciard, T. B. Norris, D. M. Tennant, J. A. Taylor, J. E. Bower, and S. Pau, "Imaging nanostructures with coherent phonon pulses," Appl. Phys. Lett. **84**(25), 5180–5182 (2004).
13. S. Zhang, E. Peronne, L. Belliard, S. Vincent, and B. Perrin, "Three-dimensional acoustic wavefront imaging in anisotropic systems by picosecond acoustics," J. Appl. Phys. **109**(7), 033507 (2011).
14. A. Amziane, L. Belliard, F. Decremps, and B. Perrin, "Ultrafast acoustic resonance spectroscopy of gold nanostructures: Towards a generation of tunable transverse waves," Phys. Rev. B **83**(7), 014102 (2011).
15. S. Bourquin, R. P. Prasankumar, F. X. Kartner, J. G. Fujimoto, T. Lasser, and R. P. Salathe, "High-speed femtosecond pump-probe spectroscopy with a smart pixel detector array," Opt. Lett. **28**(3), 1588–1590 (2003).
16. R. J. Smith, M. G. Somekh, S. D. Sharples, M. C. Pitter, I. Harrison, and C. Rossignol, "Parallel detection of low modulation depth signals: application to picosecond ultrasonics," Meas. Sci. Technol. **19**(8), 055301 (2008).
17. R. J. Smith, R. A. Light, S. D. Sharples, N. S. Johnston, M. C. Pitter, and M. G. Somekh, "Multichannel, time-resolved picosecond laser ultrasound imaging and spectroscopy with custom complementary metal-oxide-semiconductor detector," Rev. Sci. Instrum. **81**, 024901 (2010).
18. E. Pontecorvo, M. Ortolani, D. Polli, M. Ferretti, G. Ruocco, G. Cerullo, and T. Scopigno, "Visualizing coherent phonon propagation in the 100 GHz range: A broadband picosecond acoustics approach," Appl. Phys. Lett. **98**(3), 011901 (2011).
19. A. Bartels, R. Cerna, C. Kistner, A. Thoma, F. Hudert, C. Janke, and T. Dekorsy, "Ultrafast time-domain spectroscopy based on high-speed asynchronous optical sampling," Rev. Sci. Instrum. **78**, 035107 (2007).
20. S. Dilhaire, G. Pernot, G. Calbris, J. M. Rampnoux, and S. Grauby, "Heterodyne picosecond thermoreflectance applied to nanoscale thermal metrology," J. Appl. Phys. **110**(13), 114314 (2011).
21. E. Peronne, E. Charron, S. Vincent, S. Sauvage, A. Lemaitre, B. Perrin, and B. Jusserand, "Two-color femtosecond strobe lighting of coherent acoustic phonons emitted by quantum dots," Appl. Phys. Lett. **102**(4), 043107 (2013).
22. V. Temnov, C. Klieber, K. A. Nelson, T. Thomay, V. Knittel, A. Leitenstorfer, D. Makarov, M. Albrecht, and R. Bratschitsch, "Femtosecond nonlinear ultrasonics in gold probed with ultrashort surface plasmons," Nat. Commun. **4**(6), 1468 (2013).
23. T. Pezeril, F. Leon, D. Chateigner, S. Kooi, and K. A. Nelson, "Picosecond photoexcitation of acoustic waves in locally canted gold films," Appl. Phys. Lett. **92**(3), 061908 (2008).
24. P.-A. Mante, A. Devos, and A. Le Louarn, "Generation of terahertz acoustic waves in semiconductor quantum dots using femtosecond laser pulses, " Phys. Rev. B **81**(11), 113305 (2010).
25. B. Perrin, B. Bonello, J. C. Jeannet, and E. Romatet, "Interferometric detection of hypersound waves in modulated structures, " Prog. Nat. Sci. Suppl. **6**, S444 (1996).
26. D. H. Hurley and O. B. Wright, "Detection of ultrafast phenomena by use of a modified Sagnac interferometer," Opt. Lett. **24**, 1305–1307 (1999).
27. O. Matsuda, M. Tomoda, and T. Tachizaki, "Ultrafast ellipsometric interferometry for direct detection of coherent phonon strain pulse profiles," J. Opt. Soc. Am. B **30**, 1911–1921 (2013).
28. K. J. Manke, A. A. Maznev, C. Klieber, V. Shalagatskyi, V. V. Temnov, D. Makarov, S.-H. Baek, C.-B. Eom, and K. A. Nelson, "Measurement of shorter-than-skin-depth acoustic pulses in a metal film via transient reflectivity," Appl. Phys. Lett. **103**(4), 173104 (2013).
29. P. J. S. van Capel and J. I. Dijkhuis, "Optical generation and detection of shock waves in sapphire at room temperature," Appl. Phys. Lett. **88**(3), 151910 (2006).
30. A. Bojahr, M. Herzog, D. Schick, I. Vrejoiu, and M. Bargheer, "Calibrated real-time detection of nonlinearly propagating strain waves," Phys. Rev. B **86**(5), 144306 (2012).
31. H. Y. Hao and H. J. Maris, "Experiments with acoustic solitons in crystalline solids," Phys. Rev. B **64**(7), 064302 (2001).
32. E. Peronne and B. Perrin, "Generation and detection of acoustic solitons in crystalline slabs by laser ultrasonics," Ultrasonics **44**, 1203–1207 (2006).
33. P. J. S. van Capel and J. I. Dijkhuis, "Time-resolved interferometric detection of ultrashort strain solitons in sapphire," Phys. Rev. B **81**(9), 144106 (2010).
34. Y. Hiki and A. V. Granato, "Anharmonicity in noble metals; higher order elastic constants," Phys. Rev. **144**, 411–419 (1966).
35. Y. Li, Q. Miao, A. V. Nurmikko, and H. J. Marisa, "Picosecond ultrasonic measurements using an optical cavity," J. Appl. Phys. **105**(8), 083516 (2009).

#201826 - $15.00 USD Received 29 Nov 2013; revised 10 Jan 2014; accepted 11 Jan 2014; published 20 Feb 2014

36. C.-K. Min, D. G. Cahill, and S. Granick, "Time-resolved ellipsometry for studies of heat transfer at liquid/solid and gas/solid interfaces," Rev. Sci. Instrum. **81**(7), 074902 (2010).
37. D. H. Feng, X. Q. Pan, X. Li, T. Q. Jia, and Z. R. Sun, "Coherent acoustic phonon generation and detection by femtosecond laser pulses in ZnTe single crystals," J. Appl. Phys. **114**(9), 093513 (2013).
38. T. Pezeril, V. Gusev, D. Mounier, and P. Ruello, "Surface motion induced by laser action on opaque anisotropic crystals," J. Phys. D Appl. Phys. **38**, 1421–1428 (2005).
39. T. Pezeril, P. Ruello, N. Chigarev, S. Gougeon, D. Mounier, J.-M. Breteau, P. Picart, and V. Gusev, "Generation and detection of plane coherent shear picosecond acoustic pulses by lasers: Experiment and theory," Phys. Rev. B **75**(19), 174307 (2007).
40. T. Pezeril, C. Klieber, S. Andrieu, and K. A. Nelson, "Optical generation of gigahertz-frequency shear acoustic waves in liquid glycerol," Phys. Rev. Lett. **102**(4), 107402 (2009).
41. C. Klieber, T. Pezeril, S. Andrieu, and K. A. Nelson, "Optical generation and detection of gigahertz-frequency longitudinal and shear acoustic waves in liquids: theory and experiment," J. Appl. Phys. **112**(11), 013502 (2012).
42. M. Ducousso, O. E.-F. Zouani, C. Chanseau, C. Chollet, C. Rossignol, B. Audoin, and M.-C. Durrieu, "Evaluation of mechanical properties of fixed bone cells with sub-micrometer thickness by picosecond ultrasonics," Eur. Phys. J. Appl. Phys. **61**(10), 11201 (2013).
43. O. Kovalenko, T. Pezeril, and V. Temnov, "New concept for magnetization switching by ultrafast acoustic pulses," Phys. Rev. Lett. **110**(5), 266602 (2013).
44. http://perso.univ-lemans.fr/~tpezeril/crbst_5.html

1. Introduction

Time-resolved optical experiments based on femtosecond lasers have become extremely popular and of routine use for investigating ultrafast phenomena in condensed matter, chemical, and biological systems. Independent of the phenomena investigated, the pump-probe femtosecond technique behind the time-resolved optical experiment is typically used in conjunction to lock-in amplifiers fed by photodiodes which restrict the possibility of ultrafast imaging. It is only in the disciplines involving high power lasers (shock waves [1], polaritons [2]...) that cameras are extensively used. The reason behind this is the necessity of high power lasers to achieve sufficient detectable pump-probe signal magnitudes. Although the pulse repetition rate from low-power femtosecond laser oscillators is extremely high, the pulse energies are low compared to high-power lasers, and therefore the signal levels are difficult to detect by cameras. Since standard CCD cameras are not suitable to detect modulated signals, the advantage of high-repetition-rate femtosecond laser oscillators to detect high signal-to-noise ratio modulated pump-probe signals becomes less of a benefit. To address this, we present in this paper an imaging technique with low-noise and high-sensitivity performances (in the range of 10^{-4}) based on pump-probe lock-in acquisition of images with a standard CCD.

In the discipline of picosecond ultrasonics, femtosecond lasers enable the generation and detection of ultrashort acoustic pulses on picosecond time scales [3]. In order to go beyond the conventional picosecond ultrasonics experiments, we illustrate the potential of our technique by imaging picosecond time scale ultrasonic pulses propagating in a thin gold film. Usually, ultrasonic pulses are exploited for thin film mechanical diagnostics and for the measurement of linear acoustic properties of materials [4,5]. In the present case, we demonstrate through direct visualization of ultrasonic pulse nonlinear acoustic reshaping during propagation which can be used in order to estimate the acoustic nonlinear properties of the material. Our results are a step forward in picosecond ultrasonic imaging over pump-probe scanning of the sample surface [6–11], far-field acoustic imaging [12–14], multi-channel detection [15–18] or asynchronous lasers [19–21].

2. Experimental set-up and methodology

A Ti-sapphire oscillator with an intra-cavity dumper running at a repetition rate of 500 kHz was used to generate laser pulses with a central wavelength of 800 nm and duration of 150 fs. The laser output was split into separate pump and probe beams. The probe beam was frequency-

#201826 - $15.00 USD Received 29 Nov 2013; revised 10 Jan 2014; accepted 11 Jan 2014; published 20 Feb 2014

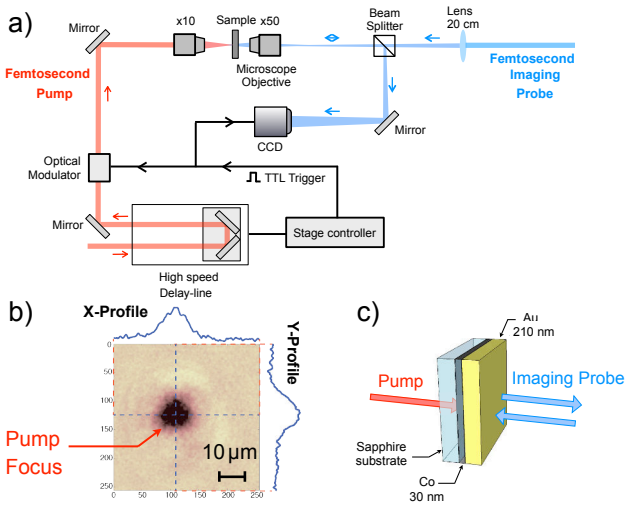

Fig. 1. a) Sketch of the femtosecond pump-probe imaging experimental setup. The $\times 50$ microscope objective is adjusted to image the front of the sample surface by a 400 nm probe onto the CCD camera with high magnification. A 20 cm lens before the beam splitter is used to illuminate the whole CCD sensor. The 800 nm pump beam that excites the transient phenomenon is focused on the back of the sample by a $\times 10$ microscope objective. The stage controller synchronously triggers the pump beam modulation and the image acquisition during the continuous motion of the high speed delay-line. After image processing, we obtain sequences of images showing picosecond time resolved evolution of the photoexcited phenomena. b) The pump beam is in focus at the sample surface where the light intensity forms a 2D gaussian profile with a FWHM of about 10 μm. c) The sample investigated here is a metallic multilayer structure composed of a 210 nm gold (Au) layer and a 30 nm cobalt (Co) layer coated on a sapphire substrate. The pump beam is focused on the back side of the sample at the cobalt layer while the probe beam is used to image the front gold free surface.

doubled by a second harmonic generation BBO crystal in order to obtain a probe wavelength of 400 nm. For imaging the sample surface onto the CCD, we used a $\times 50$ Mitutoyo microscope objective, and a 20 cm lens placed before the probe beam-splitter in order to illuminate the whole CCD sensor, see Fig. 1(a). The pump beam of 15 nJ single pulse energy was focused onto the back of the sample with a $\times 10$ Mitutoyo microscope objective producing a 2D gaussian laser profile at the focal spot with a FWHM (Full-Width at Half-Maximum) of about 10 μm, see Fig. 1(b). In order to avoid unwanted drift of the probe pointing during image acquisition, the pump beam is time delayed rather than the probe beam. The delay-line used in the experiment is composed of a Newport ILS-LM high speed linear motor stage of maximum speed of 500 mm/s controlled by a Newport XPS controller as shown in Fig. 1(a). This stage controller is a key aspect of the setup ensuring the electronic synchronization of pump modulation and image acquisition. The optical modulator is an acousto-optic (AO) deflector cell which deflects the pump beam with a deflection efficiency of about 90%. The disadvantage of using an AO deflector is the fact that it alters the beam quality of the deflected beam; thus, the 0^{th} order transmitted pump beam is directed to the sample rather than the deflected 1^{st} order pump beam. The TTL trigger sent by the XPS controller at a predefined rate (lower than the maximum frame rate of the camera) during the continuous motion of the delay-line alternatively switches the AO modulation on and off while the image acquisition occurs at each

#201826 - $15.00 USD Received 29 Nov 2013; revised 10 Jan 2014; accepted 11 Jan 2014; published 20 Feb 2014

trigger. When the TTL trigger rate is set at f_0, the image frame rate is locked at f_0, while the AO modulation rate is locked at $f_0/2$. This means that two successively recorded images do not carry the same information since one of them is recorded when the pump beam is present (the signal image) while the second is recorded without pump beam (the reference image). The reference image is recorded in order to sample the laser noise. Typically, laser fluctuations with the laser noise amplitude inversely proportional to the frequency dominate over electrical noise of the light detector. As a result, balancing the reference image with the signal image is used to drastically reduce laser noise. As in the conventional point pump-probe measurements with a lock-in amplifier, the signal and reference images should be acquired as close together in time as possible i.e. at the highest possible frequency. Thus, the ideal camera would have extremely low electrical noise and a high dynamic range in order to detect weak optical signals on top of a significant background (set close to pixel saturation for maximum detection capability), and fast frame rate for noise reduction. The camera we use is a Hamamatsu EM-CCD 9100-02, with high dynamic range (full well capacity of 70 000 electrons, 10 electrons of readout noise, 14 bit A/D converter) and maximum frame rate of 30 Hz at full image resolution of 1000×1000 pixels. Compared to CMOS cameras, CCD cameras have the advantage of low-noise electrical detectors, however, their frame rate at full image resolution is always lower than for CMOS [2]. Given the fact that the full image resolution of 1000×1000 pixels is not necessary in our experiment, a good compromise between frame rate and image resolution is given by an image acquisition at setting the image acquisition at 256×256 pixels for the image resolution while running the CCD at 101 Hz. The exposure time is set below 1/101 s and the probe light intensity is adjusted close to the pixel saturation for optimum sensitivity.

All the recorded images were processed by the following basic image treatment,

$$\frac{\Delta I}{I}(i) = \frac{2(I_{2i+1} - I_{2i})}{I_{2i+1} + I_{2i}} = \frac{\Delta R}{R}(i), \tag{1}$$

where I_{2i+1} is the $2i+1$-th image (a signal image), and I_{2i} is the $2i$-th image (reference image), both stored in the computer RAM. During continuous acquisition and motion of the delay-line, the computer calculates the result of formula (1) in real time which, for each signal and reference image pair gives the i-th image of the absolute change in light intensity $\frac{\Delta I}{I}(i)$, equals to the change of the sample optical reflectivity $\frac{\Delta R}{R}(i)$. Because of the continuous motion of the delay-line during acquisition, the i-th index of the image is assigned to a certain time delay τ ($\frac{\Delta R}{R}(i) \equiv \frac{\Delta R}{R}(\tau)$). The $\frac{\Delta R}{R}(\tau)$ images are directly scaled in absolute units, which is an advantage compared to standard lock-in detection techniques where the signal is usually scaled in arbitrary units. After each "acquisition run", we obtain a sequence of images displaying the time variation of $\frac{\Delta R}{R}(\tau)$ over the desired time delay interval. The total number of images n_i in the acquired sequence depends on the time delay interval, the frame rate of the camera and the delay-line speed. The sequence of "acquisition runs" is performed as many times as necessary in order to average the noise level of the n_i images of the sequence. After N sequences of "acquisition runs" we obtained a smoothed time variation of the sequence $< \frac{\Delta R}{R}(\tau) >_N$, averaged over N runs.

3. Results and discussion

For the experiment, a hybrid multilayer sample structure composed of a 210 nm gold / 30 nm cobalt / sapphire substrate, depicted in Fig. 1(c), has been manufactured by RF magnetron sputtering (details can be found elsewhere [22]). The femtosecond pump beam is focused through the transparent sapphire substrate on the back of the sample at the cobalt layer. As a results of the strong electron-phonon coupling in cobalt, the laser excited electrons rapidly transfer their excess energy to the lattice such that the cobalt layer thermally expands and generates an ultra-

#201826 - $15.00 USD Received 29 Nov 2013; revised 10 Jan 2014; accepted 11 Jan 2014; published 20 Feb 2014

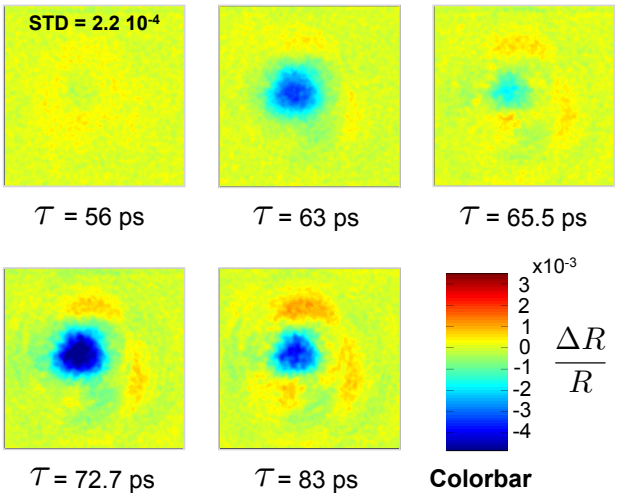

Fig. 2. After image processing, we obtain a sequence of images showing time resolved evolution of the transient reflectivity $\Delta R/R$ on a picosecond time scale. Here, we show selected images from τ = 56 ps to 83 ps after the pump excitation of the acoustic pulse - see the supplementary material online for the full sequence (Media 1). In the present case, the arrival of the laser excited acoustic pulse from the cobalt layer at the gold front surface slightly modifies the gold optical reflectivity. Each image of the transient reflectivity $\Delta R/R$ at different time delays is a display of the 2D acousto-optic response. The transient reflectivity change reaches about -4$\times 10^{-3}$ at the blue center part of the images. The fact that the center blue part on the images reaches two pseudo-maxima at τ = 63 ps and 72.7 ps is inherent to the acousto-optic detection of an unipolar acoustic pulse at a free surface. The orange edge part which changes the transient reflectivity by about 2×10^{-3} and appears at different time delays compared to the blue center part is the signature of the nonlinear acoustic propagation of the acoustic pulse trough gold.

short acoustic strain pulse propagating both into the gold layer and into the sapphire substrate. The excellent acoustic impedance matching between the cobalt opto-acoustic transducer and gold or sapphire minimizes the acoustic reflections at the surrounding interfaces (only about 10% of acoustic strain gets reflected). As a consequence, the initial shape of the acoustic pulse transmitted into gold follows the spatial profile of the laser deposited heat in the cobalt layer. Since the optical skin depth in cobalt at 800 nm wavelength is about 13 nm, the acoustic pulse profile follows the same spatial extension. After propagation through the 210 nm gold layer at the gold acoustic speed of $\sim$ 3.3 nm/ps [23], the laser excited acoustic pulse reaches the free surface of gold where it slightly modifies the optical reflectivity R through the acousto-optic effect and produces an image sampled by the imaging femtosecond probe pulse. Figure 2 shows the transient reflectivity $< \frac{\Delta R}{R}(\tau) >$ at five different time delays τ. The complete sequence with a total number of images n_i = 150 has been averaged for N = 1000 times which corresponds to a total acquisition time of about 30 minutes. As a comparison, for an equivalent image resolution of 250$\times$250, conventional pump-probe scanning of the surface sample would take about 250$\times$250$\times$5 s $\sim$ 5000 minutes (if we assume that one single acquisition takes about 5 s each), which is roughly 100 times longer than offered by our experimental technique. To further improve image quality and to diminish the uncorrelated pixel noise, a standard numerical filtering procedure using a 3$\times$3 circular averaging filter has been applied to each individual image of the sequence. This numerical filter does not alter the image resolution (which is close to the

#201826 - $15.00 USD Received 29 Nov 2013; revised 10 Jan 2014; accepted 11 Jan 2014; published 20 Feb 2014

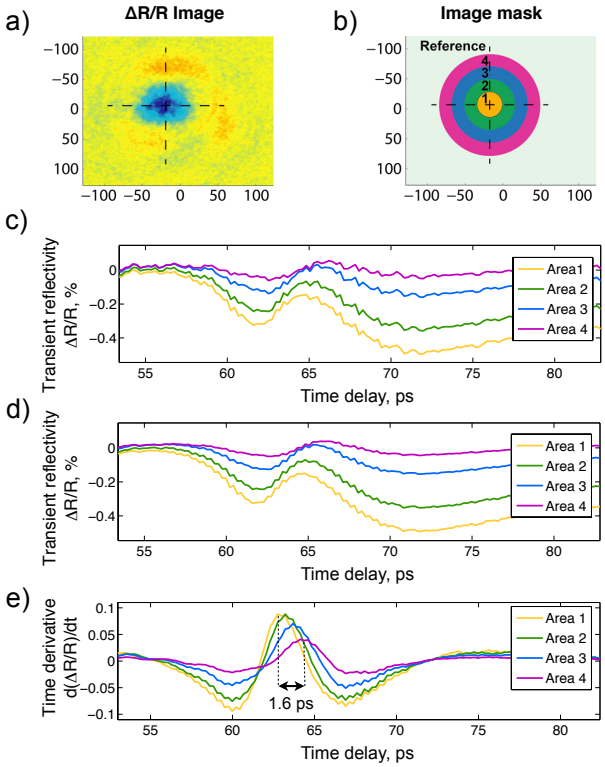

Fig. 3. a) and b) After image processing, every transient reflectivity image at each time delay has been numerically split in 4 different areas and a reference area defined by an image mask. These five areas of the image mask include Area 1 which comprises the center of the transient reflectivity maximum, Areas 2 through 4 as concentric areas around the center and the Reference Area with negligible pump induced transient reflectivity signal which is used as a noise reference image. c) Mean transient reflectivity signal of each of the four concentric areas. d) The signal-to-noise level is increased by a factor of 3 when the noise reference Area is used in the image processing. e) The smoothed time derivatives of the signals shown in d) reveal different arrival times of the acoustic pulse at the front gold surface for different areas corresponding to different laser pump power inputs. We observe a 1.6 ps time difference between the areas of maximum (Area 1) and minimum (Area 4) pump fluence which is in close agreement with the calculated estimates of the nonlinear acoustic propagation in gold.

diffraction limit) but only removes high frequency spatial noise and improves the pixel standard deviation (STD) from 5.1×10^{-4} to 2.1×10^{-4}, see Fig. 2 at $\tau = 56$ ps. The value of the STD (in the range $\sim10^{-4}$) gives a reliable estimate of the detection sensitivity of the experiment, which is significantly better than required for this measurement. Increasing the number of averages N would improve the detection sensitivity by $\sqrt{N}$, however it would critically augment the total acquisition time.

The acousto-optic detection process at the free sample surface works as long as the propagating acoustic pulse remains in the probe optical penetration depth area of about $\xi = 32$ nm typical size at 400 nm probe wavelength. Because of the reflection of the propagative acoustic pulse at the free surface with a change in sign (the pressure strain is converted into a tensile

#201826 - $15.00 USD Received 29 Nov 2013; revised 10 Jan 2014; accepted 11 Jan 2014; published 20 Feb 2014

strain), the detected reflectivity signal goes through a minimum when the pressure and tensile strain upon reflection balance each other (i.e. when the first half of the reflected strain overlaps with the other half of the incoming strain) and the sign of the detected reflectivity variation changes due to the inversion of the sign of the strain. As a consequence of the acoustic reflection at the free surface the acoustic pulse appears to have a bipolar reflectivity signal even if the acoustic pulse has unipolar shape. This artifact of acousto-optic detection can be seen in Fig. 2 which displays a selection of reflectivity images at different time delays τ. The resulting minimum in the reflected signal at τ = 65.5 ps can be directly seen in the corresponding image and previous and subsequent images, at τ = 63 ps and 72.7 ps respectively, illustrating the non-symmetrical shape (i.e. bipolar shape) of the acousto-optic signal. The relevant acousto-optic detection process is described by,

$$\frac{\Delta R}{R}(\tau) \equiv \int_0^{+\infty} s(z)\eta(z,\tau)dz, \tag{2}$$

where the sensitivity function $s(z)$ (which depends on the optical and acousto-optical properties of the film [3]) weights the influence of the propagative acoustic strain $\eta(z,\tau)$ on the change in reflectivity at different depths z below the free surface of the film. From Eq. (2) it is obvious that the measured change in reflectivity does not directly describe the acoustic strain, but is a convolution of the optical sensitivity function $s(z)$ with the propagative acoustic strain $\eta(z,\tau)$. The inability to optically detect the exact acoustic pulse shape [24] is problematic. Different detection techniques have been developed to circumvent this limitation [25–27], however, in a situation as the one described here it has recently been demonstrated [28] that an appropriate algorithm can retrieve the actual profile of the acoustic pulse from transient reflectivity measurements. We will see in the following that in case of transient reflectivity detection of shorter-than-skin-depth acoustic pulses in a gold film, the situation can be simplified. At the moment, we will emphasize the direct observation of the nonlinear reshaping of the propagating acoustic pulse.

The foremost observation in nonlinear laser acoustics (high-power laser excitation of weak to strong shock waves [1, 22, 29, 30] or solitons [31–33]) is the increase in sound velocity (over the speed of sound of the material) of large pressure acoustic pulses. As a matter of fact, any experimental evidence of the acoustic velocity being dependent on the acoustic pressure implies the involvement of nonlinear acoustics. The sequence of reflectivity images of Fig. 2, in particular the orange edge portion whose maximum has a time offset as compared to the blue center part (compare the images at τ = 72.7 ps and 83 ps in Fig. 2) is a direct demonstration of the nonlinear propagation of the inhomogeneous acoustic pulse. Since the laser pump is focused as an inhomogeneous 2D gaussian profile, see Fig. 1(a), the non-uniform amplitude of the laser pump will give rise to an inhomogeneous acoustic pulse that does not travel at a constant speed. As a consequence, the acoustic speed will be non-uniform along the in-plane position of the acoustic pulse. This is the reason for the center blue portion of the acoustic pulse with higher acoustic pressure arriving before the orange edge portion with lower acoustic pressure. A second step of image analysis provides deeper insight into the observation of the governing nonlinear acoustic phenomena. In this step, each image of the sequence has been processed with a predefined image mask - adapted to the 2D Gaussian excitation profile, with four plus one different areas in order to isolate five different subimages. A selected raw image and the adapted mask are shown in Figs. 3(a) and 3(b). The mask has a central part, the first area with a disk-like shape centered at the in-plane position of the maximum transient reflectivity signal, and corresponds to the maximum in pump light intensity. Finally, the last region, Area 5, serves as a reference area with negligible pump induced transient reflectivity signal to quantify the measurement noise. After applying the mask, the mean values of each of the five resulting subimages are calculated. From all the images constituting the sequence, we obtain

#201826 - $15.00 USD Received 29 Nov 2013; revised 10 Jan 2014; accepted 11 Jan 2014; published 20 Feb 2014

the picosecond time evolution of the mean values for each of the 4 areas - as displayed in Figs. 3(c) and 3(d). While Fig. 3(c) shows the extracted mean values of Areas 1 through 4, Fig. 3(d) shows the same results after subtractions of the mean value of the reference area, Area 5, which diminishes the noise level further. Comparison of the results of Area 4 shown in Figs. 3(c) with 3(d) demonstrates that the subtraction of the reference area removes noise by about a factor of 3 – a substantial improvement of data quality. More quantitatively, the STD value of Area 4 decreases from 8.9×10^{-5} to 3.4×10^{-5} when the reference Area is subtracted. In case of gold and a probe wavelength of 400 nm [28], the time derivative of the transient reflectivity signal approximates very well the acoustic strain profile η in Eq. (2). As a final step, we perform the time derivation of the reflectivity signals displayed in Fig. 3(d), which yields the approximate acoustic pulse profiles for each of the four different areas. The results of this procedure in Fig. 3(e) highlight that the acoustic pulse arrival is different for the 4 different areas with different acoustic pressures. From the acoustic pulse with higher pressure (Area 1) arriving before the acoustic pulse with lower pressure (Area 4), we conclude the nonlinear acoustic propagation through gold. Between Area 1 and Area 4, we measure a time jitter of about 1.6 ps in arrival time of the acoustic pulse, consistent with what has been measured with femtosecond surface plasmon interferometry [22]. This time jitter only depends on the third order elastic parameter of gold and on the peak amplitude of the generated acoustic pulse. In case of gold, since this nonlinear elastic coefficient is already known [34], our results displayed in Fig. 3, directly scaled in absolute units, can be used to estimate the absolute value of the photoelastic coefficients in the sensitivity function $s(z)$ of Eq. (2). From the comparison of the measured intensity-dependence of the time jitter with the solutions of the nonlinear Korteveg-de Vries (KdV) theory [22, 31], we obtain an estimate of the photoelastic coefficients in gold at 400 nm probe wavelength, $dn/d\eta = 2.0 \pm 0.7$ and $dk/d\eta = 1.0 \pm 0.3$. Vice versa when a material is studied with unknown nonlinear elastic coefficient, the analysis of the time jitter and the nonlinear reshaping of ultrashort acoustic pulses can be exploited to extract the values of elastic nonlinearities.

4. Conclusion

Through this paper we introduced an ultrafast pump-probe experiment based on lock-in acquisition of images. The technique enables direct 2D visualization of femtosecond laser induced phenomena. To illustrate the high-sensitivity, low-noise performance of the developed setup, we present the direct visualization of the nonlinear propagation and reshaping of an ultrashort acoustic pulse in gold. Potentially, this experimental technique could lead to a simple and routine measurement of nonlinear elastic parameters of many materials. To facilitate the detection of even smaller features in time resolved images it could be possible to further increase the image resolution close to the diffraction limit. The detection sensitivity could be improved further with a new type of low noise CMOS sensors with a frame rate of $\sim$ 800 Hz at 256×512 pixels resolution (Hamamatsu OrcaFlash), and by using different detection techniques [35–37]. Beyond that, we envision to use this new technique for imaging longitudinal or transverse ultrasonic echoes in biological or liquid samples [38–42] or to adapt the experiment for Magneto-optical Kerr measurements in order to image magnetic domains subjected to ultrashort acoustic pulses [43]. The latest results can be found online [44].

Acknowledgments

This work has been financially supported by Région des Pays de la Loire under contract ECHOPICO, and sponsored by Réseau-Femto CNRS. We acknowledge Brice Villier from Hamamatsu Photonics for technical support and C. Krien (IFW Dresden) for deposition of metal films.

#201826 - $15.00 USD Received 29 Nov 2013; revised 10 Jan 2014; accepted 11 Jan 2014; published 20 Feb 2014

References

[1] C. Thomsen, H. T. Grahn, H. J. Maris and J. Tauc. Surface generation and detection of phonons by picosecond light pulses. *Phys. Rev. B*, 34:4129–4138, 1986.

[2] O. B. Wright and V. Gusev. Ultrafast generation of acoustic waves in copper. *IEEE Transactions on Ultrasonics, Ferroelectrics and Frequency Control*, 42:331–338, May 1995.

[3] T. Saito, O. Matsuda and O. B. Wright. Picosecond acoustic phonon pulse generation in nickel and chromium. *Phys. Rev. B*, 67(205421), 2003.

[4] H. Park, X. Wang, S. Nie, R. Clinite and R. Cao. Mechanism of coherent acoustic phonon generation under nonequilibrium conditions. *Phys. Rev. B*, 72(100301), 2005.

[5] M. Lejman, V. Shalagatskyi, O. Kovalenko, T. Pezeril, V. V. Temnov and P. Ruello. Ultrafast optical detection of coherent acoustic phonons emission driven by superdiffusive hot electrons. *J. Opt. Soc. Am. B*, 31(2), 2013.

[6] K. J. Manke, A. A. Maznev, C. Klieber, V. Shalagatskyi, V. V. Temnov, D. Makarov, S.-H. Baek, C.-B. Eom and K. A. Nelson. Detection of shorter-than-skin-depth acoustic pulses in a metal film via transient reflectivity. *Appl. Phys. Lett.*, 103(173104), 2013.

[7] M. Bonn, D. N. Denzlerv, S. Funk, M. Wolf, S.-S. Wellershoff and J. Hohlfeld. Ultrafast electron dynamics at metal surfaces: Competition between electron-phonon coupling and hot-electron transport. *Phys. Rev. B*, 61(1101), 2000.

[8] G. Tas and H. J. Maris. Electron diffusion in metals studied by picosecond ultrasonics. *Phys. Rev. B*, 49(15046), 1994.

[9] V. V. Temnov, K. Nelson, G. Armelles, A. Cebollada, T. Thomay, A. Leitenstorfer and R. Bratschitsch. Femtosecond surface plasmon interferometry. *Opt. Exp.*, 17(10):8423, 2009.

[10] J. Y. Bigot, M. Vomir, L. H. F. Andrade and E. Beaurepaire. Ultrafast magnetization dynamics in ferromagnetic cobalt: The role of the anisotropy. *Chem. Phys.*, 318:137–146, 2005.

[11] M. Kimble. *Femtochemistry VII: Fundamental Ultrafast Processes in Chemistry, Physics, and Biology*. Elsevier, Oct. 3 2006.

[12] M. Getzlaff, J. Bansmann and G. Schonhense. Spin-polarization effects for electron-spassing through iron and cobalt films. *Solid. State. Comm.*, 87:467–469, 1993.

[13] S. I. Anisimov, B. L. Kapeliovich and T. L. Perelman. Electron emission from metal surfaces exposed to ultrashort laser pulses. *Sov. Phys. JETP*, 39:375–377, 1974.

[14] M. I. Kaganov, I. M. Lifshitz and L. V. Tanatarov. Relaxation between electrons and crystalline lattices. *Sov. Phys. JETP*, 4:173–178, 1957.

[15] J. Hohlfeld, S.-S. Wellershoff, J. Güdde, U. Conrad, V. Jähnke and E. Matthias. Electron and lattice dynamics following optical excitation of metals. *Chem. Phys.*, 251:237–258, 2000.

[16] B. C. Gundrum, D. G. Cahill and R. S. Averback. Thermal conductance of metal-metal interfaces. *Phys. Rev. B*, 72(245426), 2005.

[17] C. K. Sun, F. Vallee, L. H. Acioli, E. P. Ippen and J. G. Fujimoto. Femtosecond-tunable

measurement of electron thermalization in gold. *Phys. Rev. B*, 50(20):337–348, 1994.

[18] T. Rangel, D. Kecik, P. E. Trevisanutto, G.-M. Rignanese, H. Van Swygenhoven and V. Olevano. The bandstructure of gold from many-body perturbation theory. *Phys. Rev. B*, 86(125125), 2012.

[19] S. Linic, U. Aslam, C. Boerigter and M. Morabito. Photochemical transformations on plasmonic metal nanoparticles. *Nature Mat.*, 14:567–576, 2015.

[20] P. Phillips. *Advanced Solid State Physics*. Cambridge Univ. Press, 2012.

[21] W. S. Farm, R. Storz and H. W. K. Tom. Electron thermalization in gold. *Phys. Rev. B*, 46(20), 1992.

[22] M. G. Haines, M. S. Wei, F. N. Beg and R. B. Stephens. Hot-electron temperature and laser-light absorption in fast ignition. *Phys. Rev. Lett.*, 102(045008), 2009.

[23] D. Y. Tzou. *Macro- to Microscale Heat Transfer: The Lagging Behavior*. John Wiley & Sons, Ltd., 2012.

[24] S. D. Brorson, J. G. Fujimoto and E. P. Ippen. Femtosecond electronic heat-transport dynamics in thin gold films. *Phys. Rev. Lett.*, 59, 1987.

[25] V. V. Temnov, C. Klieber, K. A. Nelson, T. Thomay, V. Knittel, A. Leitenstorfer, D. Makarov, M. Albrecht and R. Bratschitsch. Femtosecond nonlinear ultrasonics in gold probed with ultrashort surface plasmons. *Nature Comm.*, 4(1468), 2013.

[26] D. Bejan and G. Raseev. Nonequilibrium electron distribution in metals. *Phys. Rev. B*, 55(7), 1997.

[27] G. H. M. Rogier, R. Sprik and A. Lagendijk. Effect of a nonthermal electron distribution on the electron-phonon energy relaxation process in noble metals. *Phys. Rev. B*, 45(9), 1992.

[28] T. Q. Qiu and C. L. Tien. Size effects on nonequilibrium laser heating of metal films. *J. Heat Transfer*, 115(4):842–847, 1993.

[29] J. K. Chen and J. E. Beraun. Numerical study of ultrashort laser pulse interactions with metal films. *Numer. Heat Transfer A*, 40(1):1–20, 2002.

[30] E. M. Lifshitz and L. P. Pitaevskii. *Physical Kinetics, Course on Theoretical Physics*. Pergamon Press, Oxford, 1981.

[31] D. Y. Tzou, J. K. Chen and J. E. Beraun. Ultrafast deformation in femtosecond laser heating. *ASME J. Heat Transf.*, 124:284–292, 2002.

[32] H. E. Elsayed-Ali, T. B. Norris, M. A. Pessot and G. A. Mourou. Time-resolved observation of electron-phonon relaxation in copper. *Phys. Rev. Lett.*, 58:1212–1215, 1987.

[33] V. V. Temnov. Ultrafast acousto-magneto-plasmonics. *Nature Phot.*, 6:728–736, 2012.

[34] D. G. Cahill, W. K. Ford, K. E. Goodson, G. D. Mahan, A. Majumdar, H. J. Maris, R. Merlin and S. R. Phillpot. Nanoscale thermal transport. *J. Appl. Phys.*, 93(793), 2003.

[35] D.G. Cahill, P.V. Braun, G. Chen, D.R. Clarke, S. Fan, K.E. Goodson, P. Keblinski, W.P. King, G.D. Mahan, A. Majumdar, H.J. Maris, S.R. Phillpot, E. Pop and L. Shi. Nanoscale thermal transport ii. *Appl. Phys. Rev.*, 1, 2014.

[36] I. M. Khalatnikov. *Sov. Phys. JETP*, 22(687), 1952.

[37] E. T. Swartz and R. O. Pohl. Thermal boundary resistance. *Rev. Mod. Phys.*, 61(3):605–668, 1989.

[38] R. J. Stoner and H. J. Maris. Kapitza conductance and heat flow between solids at temperatures from 50 to 300 k. *Phys. Rev. B*, 48(16373), 1993.

[39] P. L. Kapitza. The study of heat transfer in helium ii. *J. Phys. USSR*, 4:181, 1941.

[40] M. Schreier, A. Kamra, M. Weiler, J. Xiao Gerrit, E. W. Bauer, R. Gross and S. T. B. Goennenwein. Magnon, phonon, and electron temperature profiles and the spin seebeck effect in magnetic insulator/normal metal hybrid structures. *Phys. Rev. B*, 88(094410), 2013.

[41] J. Ordonez-Miranda, J. J. Alvarado-Gil and Ronggui Yang. The effect of the electron-phonon coupling on the effective thermal conductivity of metal-nonmetal multilayers. *J. Appl. Phys*, 109(094310), 2011.

[42] G. Chen. Thermal conductivity and ballistic-phonon transport in the cross-plane direction of superlattices. *Phys. Rev. B*, 57, 1998.

[43] V. Drchal, J. Kudrnovsky, P. Bruno, P. H. Dederichs, I. Turek and P. Weinberger. Electron transport in magnetic multilayers: Effect of disorder. *Phys. Rev. B*, 65(214414), 2002.

[44] J. Velev and W. H. Butler. Effects of interface disorder on transmission probability in magnetic multilayer. *Phys. Rev. B*, 69(024404), 2004.

[45] H. T. Grahn, H. J. Maris and J. Tauc. *IEEE J. Quant. Electron.*, 25(2562), 1989.

[46] A. A. Maznev, K. J. Manke, K. H. Lin, K. A. Nelson, C. K. Sun and J. I. Chyi. Broadband terahertz ultrasonic transducer based on a laser-driven piezoelectric semiconductor superlattice. *Ultrasonics*, 52:1–4, 2012.

[47] A. Yamamoto, T. Mishina, Y. Masumoto and M. Nakayama. Coherent oscillation of zone-folded phonon modes in gaas-alas superlattices. *Phys. Rev. Lett.*, 73(740), 1994.

[48] R. M. White. Generation of elastic waves by transient surface heating. *J. Appl. Phys.*, 34(3559-3567), 1963.

[49] L. D. Landau and E. M. Lifshitz. *Mechanics*. Elsevier, New York, 1982.

[50] W. Nowacki. *Thermoelasticity*. Pergamon Press, Oxford, London, New York, Paris, 1962.

[51] T. Pezeril, F. Leon, D. Chateigner, S. Kooi and K. A. Nelson. Picosecond photoexcitation of acoustic waves in locally canted gold films. *Appl. Phys. Lett.*, 92(3)(061908), 2008.

[52] G. Steinle-Neumann, L. Stixrude and R. E. Cohen. First-principles elastic constants for the hcp transition metals fe, co, and re at high pressure. *Phys. Rev. B*, 60:791–799, 1999.

[53] O. B. Wright and K. Kawashima. Coherent phonon detection from ultrafast surface vibrations. *Phys. Rev. Letters*, 69:1668–16671, 1992.

[54] J. E. Rothenberg. Observation of the transient expansion of heated surfaces by picosecond photothermal deflection spectroscopy. *Phys. Rev. Letters*, 13:713–715, 1988.

[55] P. B. Johnson and R. W. Christy. Optical constants of transition metals: Ti, v, cr, mn, fe, co, ni, and pd. *Phys. Rev. B*, 9(5056), 1974.

[56] P. B. Johnson and R. W. Christy. Optical constants of the noble metals. *Phys. Rev. B*, 6(4370), 1972.

[57] D. W. Lynch and W. R. Hunter. *Handbook of optical constants of solids*. Elsevier, 1998.

[58] W. Maryam, A. V. Akimov, R. P. Campion and A. J. Kent. Dynamics of a vertical cavity quantum cascade phonon laser structure. *Nature Comm.*, 4(2184), 2013.

[59] E. S. K. Young, A. V. Akimov, M. Henini, L. Eaves and A. J. Kent. Subterahertz

acoustical pumping of electronic charge in a resonant tunnelling device. *Phys. Rev. Lett.*, 108(226601), 2012.

[60] T. Pezeril, C. Klieber, V. Shalagatskyi, G. Vaudel, V. Temnov, O. G. Schmidt and D. Makarov. Femtosecond imaging of nonlinear acoustics in gold. *Opt. Exp.*, 22:4590–4598, 2014.

[61] D. Mounier, C. Poilane, H. Khelfa and P. Picart. Sub-gigahertz laser resonant ultrasound spectroscopy for the evaluation of elastic properties of micrometric fibers. *Ultrasonics*, 54:259–267, 2014.

[62] J. Hohlfeld, E. Matthias, R. Knorren and K. H. Bennemann. Nonequilibrium magnetization dynamics of nickel. *Phys. Rev. Lett.*, 78(25), 1997.

[63] E. Beaurepaire, J.-C. Merle, A. Daunois and J.-Y. Bigot. Ultrafast spin dynamics in ferromagnetic nickel. *Phys. Rev. Lett.*, 76(22), 1996.

[64] J. Y. Bigot, M. Vomir and E. Beaurepaire. Coherent ultrafast magnetism induced by femtosecond laser pulses. *Nature Phys.*, 5:515–520, 2000.

[65] B. Koopmans, M. van Kampen, J. T. Kohlhepp and W. J. M. de Jonge. Ultrafast magneto-optics in nickel: Magnetism or optics? *Phys. Rev. Lett.*, 85(4), 2000.

[66] Mathematica ElementData. Density of the elements, 2015. [Online; accessed 21-September-2015].

[67] MolTech GmbH. Density of the elements, 2015. [Online; accessed 21-September-2015].

[68] Mathematica ElementData. Specific heat of the elements, 2015. [Online; accessed 21-September-2015].

[69] H. D. Young. *University Physics*. Addison Wesley, 7th edition, 1992.

[70] F. C. Campbell. *Elements of Metallurgy and Engineering Alloys*. Number 557. ASM International, 2008.

[71] C. Y. Ho, R. W. Powell and P. E. Liley. Thermal conductivity of the elements. *J. Phys. Chem. Ref. Data*, 1(2):331, 1972.

[72] A. N. Smith, J. L. Hostetler and P. M. Norris. Thermal boundary resistance measurements using a transient thermoreflectance technique. *Micro. Thermophys. Eng.*, 4:51–60, 2000.

[73] Z. Lin and L. V. Zhigilei. Electron-phonon coupling and electron heat capacity of metals under conditions of strong electron-phonon nonequilibrium. *Phys. Rev. B*, 77(075133), 2008.

[74] P. C. Lanchester, N. F. Whitehead, P. Wells and R. G. Scurlock. The low temperature specific heat of hexagonal cobalt in a magnetic field. *J. Phys. F: Met. Phys*, 5:247–254, 1975.

[75] G. Gordoba and C. R. Brooks. The heat capacity of gold. *Phys. Stat. Sol. (a)*, 6:581, 1971.

[76] S. A. Bradlye, B. Hindin, U. R. Kattner, J. G. Kaufman, C. A. Parker and H. W. Sizek. *ASM Ready Reference: Thermal Properties of Metals*. ASM International, 2002.

[77] J. T. Kohlhepp, P. LeClair, L. Lagae, W. J. M. de Jonge M. van Kampen, C. Jozsa and B. Koopmans. All-optical probe of coherent spin waves. *Phys. Rev. Lett*, 88(227201), 2002.

[78] J. N. Zhou A. Butera and J. A. Barnard. Ferromagnetic resonance in as-deposited and annealed fe-sio$_2$ heterogeneous thin films. *Phys. Rev. B*, 60(17), 1999.

[79] X. Liu, M. M. Steiner, R. Sooryakumar, G. A. Prinz, R. F. C. Farrow and G. Harp.

Exchange stiffness, magnetization, and spin waves in cubic and hexagonal phases of cobalt. *Phys. Rev. B*, 53:12166–12172, 1996.

[80] O. Kovalenko, T. Pezeril and V. V. Temnov. New concept for magnetization switching by ultrafast acoustic pulses. *Phys. Rev. Lett.*, 266602(100301), 2013.

[81] P. K. Sharma and S. K. Joshi. *J. Chem. Phys.*, 39, 1963.

[82] K. Krebs. Dynamical model for lattice vibrations in metals. *Phys. Rev. Lett.*, 10(1), 1964.

[83] C. Kittel. *Introduction to solide state physics*. Wiley, 1967.

[84] J. Behari and B. B. Tripathi. Phonon dispersion relations in noble metals. *J. Phys. C*, 3(659), 1970.

[85] A. Levy. *Basic set theory*. Springer-Verlag, Berlin-New York, 1979.

[86] C. Kittel. *Introduction to Solid State Physics*. John Wiley & Sons, 8 edition, 2004.

[87] R. Lujian M. Lim J. C. Zesch B.T. Khuri-Yakub B. Hadimioglu, E. G. Rawson and C. F. Quate. High-efficiency fresnel acoustic lenses. *Ultrafast Symp*, pages 579 – 582, 1993.

[88] B. T. Khuri-Yakub B. Hadimioglu, E.G. Rawson, R. Lujan. M. Lim, J. C. Zesch and C. F. Ouate. High-efficiency fresnel acoustic lenses. *IEEE Ultrason. Symp.*, pages 579–582, 1993.

[89] N. W. Ashcroft and N. D. Mermin. *Solid state physics*. Thomson learning: high holborn, London UK, 2003.

l'université nantes angers le mans
COMMUNAUTÉ D'UNIVERSITÉS ET ÉTABLISSEMENTS

Université du Maine
Le Mans - Laval

Thèse de Doctorat

Viktor SHALAGATSKYI

Acoustique ultra-rapide dans les couches magnétiques hybrides
Ultrafast acoustics in hybrid and magnetic structures

Résumé

L'objectif de cette thèse est de comprendre la dynamique des excitations électroniques, thermiques et acoustiques dans une structure hybride composée d'un film métallique noble et d'un film ferromagnétique. L'analyse des processus est possible grâce à l'excitation d'un film métallique par une impulsion laser ultra brève qui génère des impulsions acoustiques. L'étude s'appuie sur la technique femtoseconde pompe-sonde et les simulations numériques. Beaucoup de processus intéressants comme l'excitation des électrons chauds et génération des impulsions acoustiques peuvent être étudiés. Le fait de mieux comprendre le mécanisme de ces processus amène à la possibilité de contrôler les propriétés électroniques, mécaniques et magnétiques des matériaux. Cela permettra d'introduire des concepts innovants pour des nouveaux dispositifs ou d'optimiser la performance des dispositifs qui existent déjà.
Le point de départ de ce travail est l'observation expérimentale d'impulsions acoustiques de durée très courte (2 ps) générées dans un film de cobalt de 30 nm via excitation d'un film d'or (de 50 nm jusqu'à 500 nm). Le processus majeur en jeu est le transport ultrarapide de l'énergie par les électrons super diffusifs à travers la couche d'or. Pour étudier le transport diffusive des électrons on utilise le modèle à Deux Températures. Ce nouveau concept a été confirmé par des mesures magnétiques : excitation de la précession de la magnétisation par les électrons super diffusifs.
De plus, notre analyse des courbes de réflectivité a montré la possibilité de retrouver la résistance aux l'interfaces (résistance de Kapitza) pour les interfaces métal- diélectrique et métal-métal.

Mots clés
ultrarapide, acoustique, électron, phonon, interface, résistance

Abstract

This thesis aims to understand the ultrafast dynamics of electronic, thermal and acoustic excitations in noble metal - ferromagnet multilayer structures. We start from the initial stage of ultrafast laser excitation up to the detection of the generated picosecond acoustic pulses by using the femtosecond pump-probe technique and numerical simulations. Various interesting transient physical processes are taking place on intermediate timescales. Understanding and explaining their mechanisms leads to the possibility of controlling electronic, mechanical and magnetic properties of materials. Thus, it becomes possible to introduce innovative concepts of new devices and optimize the performances for already existing technologies.
The starting point of this work is the experimental observation by reflectivity measurements of 2-ps acoustic pulses generated in a 30 nm thin cobalt layer when the ultrashort laser pulse excites a much thicker gold over-layer of varying thicknesses from 50 to 500 nm. If we take into account the fact that the optical energy deposition by a visible light in gold is limited by a tiny (~10nm) skin depth, the only reasonable explanation of the acoustic strain generation in adjacent cobalt layer can be provided by considering ultrafast energy transport by super-diffusive hot electrons through the gold layer. The hot electron diffusion is studied within the Two Temperature Model. This novel concept was corroborated by complementary measurements of magnetization precession in cobalt induced by hot electrons initially generated in gold.
In our analysis we were able to fit both thermal and acoustic components of transient reflectivity measurements and retrieve the values of the Kapitza resistances at the metal-metal and metal-dielectric interfaces.

Key Words
ultrafast, acoustics, electron, phonon, interface, resistance.